Modelling of Saturation Currents and Dynamic Resistance in High-Temperature-Superconductors

Justin McRobbie Brooks

Victoria University of Wellington

A Thesis
submitted to the Victoria University of Wellington
in fulfilment of the requirements for the degree of
Doctor of Philosophy

May 19, 2022

Acknowledgements

First and foremost I would like to thank my supervisors, Chris Bumby and Rod Badcock, who have provided a great deal of academic and personal support during this project. Both have gone to great lengths to facilitate my development as an independent researcher and person. For this I will be eternally grateful.

I would also like to acknowledge my friend and contemporary, Ratu Mataira-Cole, who embarked on his own journey at a similar time to myself and with whom I have shared many a discussion concerning our respective subjects.

To Dr. Mark Ainslie, thank you for being a wonderful host and teacher. It is excellent to have gained you as a friend and collaborator.

To the group at Robinson, everyone has contributed to making our work environment so lovely and I am proud to have been a part of the team.

Te Hungaruarua o Atihau, kei to mihi. Nga Kaihoe o te waka Aotea, kei te mihi. Ko au te awa. Ko te awa ko au. Tihei Mauri Ora!

Finally, to my father Kit. You have helped me on every leg of this journey, providing unconditional love and support. You instilled in me an appreciation for the physical sciences and this has led me on a wonderful journey that has no doubt shaped the rest of my life. Thank you very much.

Abstract

High temperature coated conductors are useful for their large T_c, J_c and B_{c2} values. They are manufactured in long lengths and are available from numerous commercial distributors around the world. As a result, they have found use in many applications that can utilise the large magnetic fields that these materials can produce.

In any complex circuit that incorporates superconducting components, it can be desirable to include superconducting analogues of semiconducting power electronics, such as switches, and transistors. The ideal switch in a superconducting circuit has zero resistance when the switch is closed and infinite resistance when open. Only superconductors can provide the zero resistance closed state. Thus it is the onset of resistive phenomenon, the conditions under which a non zero resistance is induced in a superconducting tape, stack, or loop, that are the subject of this thesis. The two phenomena that are examined are: geometric current saturation, and dynamic resistance. Both are investigated using existing finite element models employing the $\boldsymbol{H}$-formulation and a power-law resistivity in the software COMSOL, accompanied by experimental verification.

Flux flow resistance arises when the transport current in a high temperature superconductor is larger than the critical current I_c. This current produces a sufficiently large Lorentz force such that there is continuous vortex motion through the superconductor. This results in an effective DC resistance. Today, the critical current is universally identified using an arbitrary voltage measurement criterion. In this thesis, it is demonstrated that current filling and eventual saturation across the width of a HTS tape can be observed using magnetic field imaging near to the tape surface and correlated with changes in the measured I-V characteristics. A simple model is presented to explain this behaviour which requires only that the material have a non-linear resistivity. The current filling behaviour is modelled using numerical methods and validated against experimental data obtained from commercial wires. Finally, it is shown that the saturation determined using either magnetic field imaging or voltage measurements is sensitive to the rate of change of current.

Dynamic resistance is a resistive phenomenon that occurs when an AC magnetic field interacts with a high temperature superconductor that is simultaneously carrying a DC transport current lower than the critical current. Dynamic resistance occurs when the AC field amplitude is larger than some sample dependent threshold. Comparison between numerical models and measured data demonstrate that field dependent J_c values are required to reproduce the experimentally observed transient voltage waveforms. The finite element models were then used to analyse the transient current distributions inside of vertical stacks of parallel connected tapes and predict values for the threshold magnetic field. The threshold fields exhibit a transition from 'tape-like' to 'slab-like' behaviour as the stack aspect ratio varies. Finally, the effective resistance of a current carrying hollow superconducting strip exposed to an alternating perpendicular magnetic field is presented and analysed via finite element modelling.

List of Publications Produced During Period of PhD Study

- J. Geng, **J.M Brooks**, C.W. Bumby, and R.A. Badcock, "Time-varying magnetic field induced electric field across a current-transporting type-II superconducting loop: beyond dynamic resistance effect," Submitted for review in *Supercond. Sci. Technol.*, (2021)
- **J.M. Brooks**, M.D. Ainslie, R. Mataira, R.A. Badcock, and C.W. Bumby, "Below 1μV/cm: Determining the geometrically-saturated critical transport current of a superconducting tape," *Supercond. Sci. Technol*, (2021)
- **J.M. Brooks**, M.D. Ainslie, R.A. Badcock, and C.W. Bumby, "Effect of stack geometry on the dynamic resistance threshold fields for vertical stacks of coated conductor tapes," *IEEE Trans. Appl. Supercond*, (2021)
- **J.M. Brooks**, M.D. Ainslie, Z. Jiang, S.C. Wimbush. R.A. Badcock, and C.W. Bumby, "Numerical modelling of dynamic resistance in a parallel-connected stack of HTS coated-conductor tapes," *IEEE Trans. Appl. Supercond.*, (2020)
- **J.M. Brooks**, M.D. Ainslie, Z. Jiang, A.E Pantoja, R.A. Badcock, and C.W. Bumby, "The transient voltage response of ReBCO coateed conductors exhibiting dynamic resistance," *Supercond. Sci. Technol.*, (2020)
- Z. Jiang, N. Endo, S.C. Wimbush, **J.M. Brooks**, W. Song, R.A. Badcock, D. Miyagi, and M. Tsuda, "Exploiting asymmetric wire critical current for the reduction of AC loss in HTS coil windings," *J. Phys. Commun.*, (2019)

Contents

1
Introduction

High temperature superconductors (HTS) have attracted attention since their discovery in 1986 by Bednorz and Muller [1]. They have superconducting transition temperatures above 77 K and can remain superconducting in significantly higher magnetic fields compared to low temperature superconductors. They can also support current densities orders of magnitude larger than in typical metals, with zero electrical resistance. These properties coupled with the availability of km+ lengths of commercially manufactured wire is facilitating the development of new technology. Notable examples include fusion magnets [2–6], NMR / MRI magnets [7], electric aircraft motors [8–12], dynamos [13–18], and transformer rectifiers [19, 20]. Many of these applications are useful in the pursuit of sustainable energy. This provides motivation to investigate the electromagnetic performance of HTS materials, particularly at a time when humanity must reduce its reliance on burning fossil fuels.

Two types of commercially manufactured wire are investigated in this thesis; coated-conductors and powder-in-tube conductors. The superconducting wires are manufactured by one of following companies, SuNAM, SuperPower, and InnoST. Each of these wires has a thin film geometry with each manufacturer having a separate method to include the superconducting layer within the wire. Throughout the text, the terms "wire" and "tape" will be used interchangeably to reference them.

The wire from SuperPower and SuNAM are examples of coated-conductors. SuperPower (see figure 1.1 (a)) uses ion beam assisted deposition to add buffer layers onto a substrate. This is followed by a ReBCO layer, added using metal organic chemical vapour deposition [21]. A silver capping layer is sputtered on top before the wire is encased in a copper stabiliser layer. The SuNAM wire has a

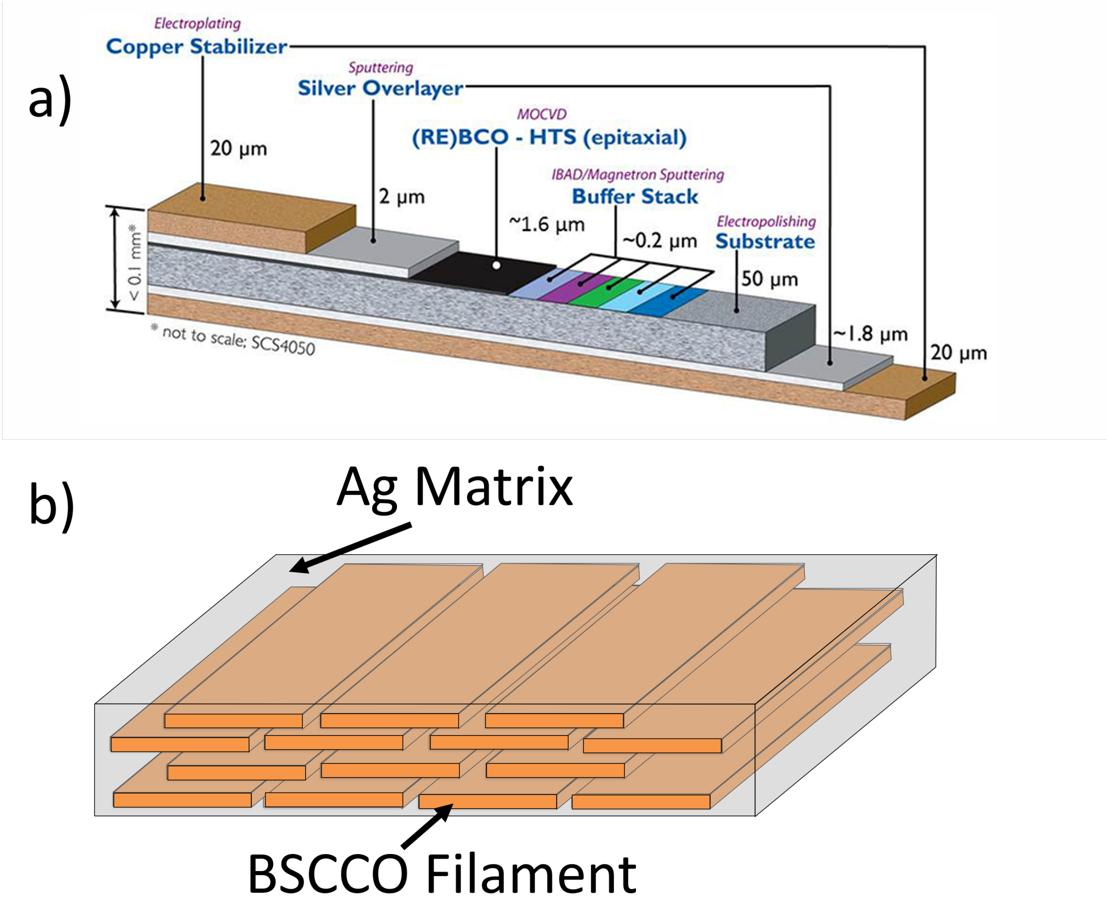

Figure 1.1: a) SuperPower coated conductor architecture [24], b) BSCCO powder-in-tube wire architecture.

similar structure, but the ReBCO layer is added using the reactive co-evaporation by deposition and reaction process [22].

BSCCO wire (see figure 1.1 (b)) is manufactured using the powder in tube method [23]. Silver tubes containing a precursor powder are drawn and placed inside of an additional silver-alloy tube. This is then repeatedly extruded, rolled, and sintered to produce a homogeneous wire. Transport measurements are performed on all three types of wire in chapter four and dynamic resistance measurements are made on SuNAM and SuperPower wires in chapter five.

All HTS tapes are type-II superconductors. Dissipation in type-II superconductors is linked to the motion of Abrikosov vortices. These are filaments of quantised magnetic flux within the material that move in response to a combination of electromagnetic and pinning forces. This thesis focuses on finite element modelling of two particular dissipative mechanisms involving the motion of vortices; geometric current saturation and the onset of flux flow resistance, and dynamic resistance. In both cases, emphasis is given to highlighting changes in the model results when the superconducting response to changes in the local magnetic flux density are considered.

Unlike conventional metals, the current distributions in superconducting wires are highly non-linear. Flux flow resistance and dissipation in HTS tapes occurs when the transport current is increased above a threshold value, known as the critical current, I_c. As the transport current is increased from zero, both the transport current and self-magnetic field penetrate the tape from the tape edges and migrate towards the centre. At I_c in self-field conditions, the Lorentz force is strong enough to cause constant vortex motion with vortex-anti vortex annihilation occurring in the tape centre (in a DC background field, a single polarity vortex traverses the entire width of the conductor). In either case, vortex motion drives current through the normal vortex cores, resulting in dissipation. I_c is typically identified using voltage measurements with an arbitrary electric field criterion (commonly 1 μV cm^{-1}). This approach inherently overestimates the critical current as the conductor must already be in the dissipative regime. This thesis will investigate how the current distribution in HTS tapes varies as the voltage definition of I_c is approached. An alternative definition for I_c is presented, based on current saturation over the tape width and observed using near surface magnetic field measurements.

Dynamic resistance occurs in HTS tapes that carry a DC transport current while exposed to an AC magnetic field with an amplitude greater than some sample dependent threshold. Under these conditions, an effective resistance is observed attributed to a net passage of flux across the conductor width. This phenomenon can be understood using the Bean critical state model which assume a field independent critical current density. In this thesis, an investigation of the DC and transient behaviour of coated conductors exhibiting dynamic resistance is presented when the electrical properties of the conductor change with the local magnetic flux density. The models are first validated against simple geometries and then extended to more complex configurations which are not easily realised experimentally.

1.1 Thesis outline

In chapter two, a brief description of the relevant physics of superconductivity is presented. The concepts surrounding flux quanta are discussed followed by the Bean critical state model. The power law is introduced which describes the gradual transition between superconducting and non-superconducting states. Analytical equations for the DC electric field in the resistive phenomenon known as dynamic resistance are presented for superconducting slabs, strips, and hollow slab geometries. This is followed by a brief description of the finite element method, which is used to produce supporting numerical analysis throughout this thesis.

In chapter three, the finite element models and experimental methods used throughout this thesis are described. This includes the constituent partial differential equations and boundary conditions used for the various problems considered here. The method by which experimental data is incorporated within the model to capture the superconducting properties as a function of magnetic field is also presented. This is followed by a brief description of the experimental procedures used in this work, including: I-V measurement procedures, power supplies, hall sensor arrays, and the magnet used to apply an AC magnetic field to samples during dynamic resistance measurements.

Chapter four presents experimental measurements and finite element modelling of the magnetic field profile near the surface of a HTS coated conductor as a function of total transport current, I_{T}. Data is presented in the range of $0 < I_{\mathrm{c}} \ll I_{\mathrm{t}}$. A method to identify the current saturated state in HTS tapes is presented which relies solely on changes to the measured magnetic field signal. The technique is then demonstrated on a number of different tapes.

In chapter five, dynamic resistance in a single tape under a perpendicular field is presented. Numerical analysis indicates that in order to fully reproduce the observed transient voltage response the FE model must employ a field-dependent resistivity. The complex current and electromagnetic field distributions that lead to this result are presented graphically using contour plots.

In chapter six, the FE model is modified to investigate the dynamic resistance in vertical stacks of parallel connected HTS tapes. The redistribution of transport current throughout the cycle of the applied field is presented. The FE model is used to investigate how the cable threshold fields transition between strip and slab like behaviour.

In chapter seven, the effective dynamic resistance exhibited by a hollow superconducting strip is presented. It is demonstrated that the physics is essentially identical to that of a hollow slab geometry, albeit with a different expression for the threshold field. Three different output regimes are identified, which are not entirely captured by the analytical model. Again, the current and electromagnetic field distributions that give rise to these regimes are presented visually using contour plots.

Finally, in chapter eight, conclusions regarding the body of work presented here are given and possible directions for future research are suggested.

2 Theoretical Background

This chapter gives a brief introduction to superconductivity with an emphasis on type-II superconductivity (all high-temperature-superconductors are this type) as well as established models which describe the observed behaviour.

2.1 Type-II Superconductivity

Superconductivity is a state of matter exhibited by certain elements and alloys, typically when cooled below a material dependent transition temperature. The transition is often identified through resistivity measurements which become vanishingly small upon entering the superconducting state. This was first observed by Kamerlingh Onnes [25] in Hg in 1911. In 1933, Meissner and Ochsenfeld discovered that these materials not only exhibit zero resistivity, but also expel magnetic fields from their interior [26]. These two criteria define superconductivity of the first type.

Today, superconductors are referred to as type-I or type-II. Type-I superconductors are described by the above two criteria, whilst type-II differs in that it permits partial magnetic field penetration of the superconducting material in the form of Abrikosov vortices [27].

Figure 2.1 shows the phase diagrams for type-I and type-II superconductors. In type-I materials, the material will transition between states if the temperature is increased above the transition temperature, T_{c}, or if a sufficiently large magnetic field, B_{c}, is applied. In type-II materials, there is is an intermediate phase between the Meissner and normal states, termed the mixed state which permits partial flux penetration. In this thesis, only type-II superconductors are considered.

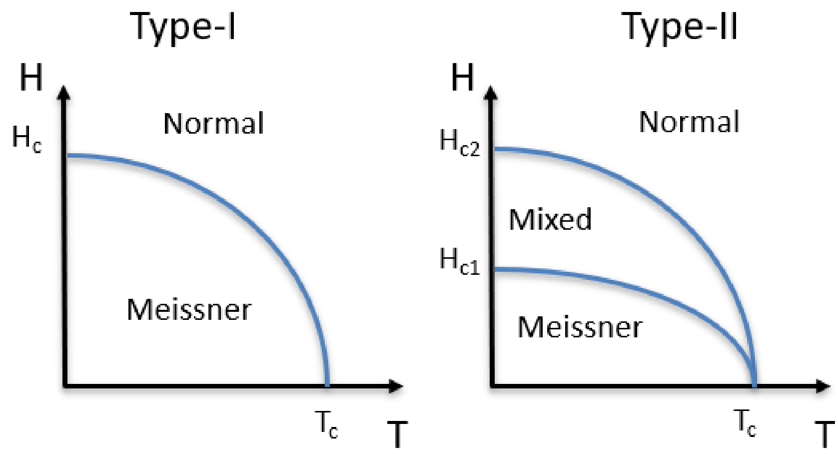

Figure 2.1: The phase diagrams of type-I (left) and type-II (right) superconductivity.

2.2 Flux Vortices, Pinning, Creep, and Flow

When a superconductor is in the mixed state, the material is partially penetrated in the form of Abrikosov vortices. These are regions of normal conducting material in which the local magnetic field exceeds the upper critical field H_{c2}. Each vortex is generated by a circulating supercurrent and is penetrated by the flux quantum, $\Phi_0 = h/2e$ where e is the fundamental charge and h Planck's constant. Vortices have an attractive (repulsive) interaction with other vortices if the supercurrents circulate in the opposite (same) direction. Vortices can also interact with variations in the crystalline structure. The Langevin equation which describes vortex motion can be written as [28]

$$\eta_v \mathbf{v} = \mathbf{F}_\mathrm{L} + \mathbf{F}_\mathrm{P} + \mathbf{F}_\mathrm{T} \tag{2.1}$$

where $\boldsymbol{v}$ is the velocity of a vortex, η_v is the vortex flow viscosity, $\mathbf{F}_\mathrm{L}$ is the Lorentz force $\mathbf{J} \times \mathbf{B}$, $\mathbf{F}_\mathrm{P}$ is the pinning force, and $\mathbf{F}_\mathrm{T}$ is the thermal fluctuation force.

The Lorentz force, $\mathbf{F}_\mathrm{L}$, is a result of the overall distribution of current and vortices within the conductor. The pinning force $\mathbf{F}_\mathrm{P}$ is a result of interactions between vortices and the crystal lattice, typically in the form of impurities which are not superconducting and as a result have a tendency to capture and hold vortices.

The final force in equation 2.1 is the thermal actuation force which is a result of random temperature fluctuations within the material.

Flux vortices are regions of normal matter and their motion through superconducting regions results in dissipation. As discussed by Bardeen [29], the dissipation can be accounted for assuming supercurrents pass through the normal vortex cores as a result of the vortex motion. This has led to extensive research into enhancement of the pinning forces as a means to improve the critical current density (current at which vortices start to move) [30–33]. There are typically two regimes of loss in a superconductor. When the Lorentz Force and pinning force are approximately equal and opposite, the thermal fluctuation force can de-pin vortices. When thermal forces are the dominant depinning forces, the resultant loss is known as flux creep. When either the applied magnetic field or transport current is increased such that the Lorentz force overcomes both the pinning and thermal forces, there is a continuous flow of vortices which is appropriately known as flux flow. It is important to note that vortex motion causes dissipation and as such, non-zero electric fields may always be present which is quite different from what one might expect of a type-I superconductor.

2.3 Bean Critical State Model

It is often desirable to enhance the pinning forces. Type-II superconductors with particularly strong pinning centres are referred to as 'hard superconductors'. The presence of pinning centres allows for flux to be trapped after cycling of an external magnetic field or transport current. The trapping of flux within the conductor leads to hysteresis in measured magnetisation loops. While the collection of forces which act upon vortices can be quite complex, there is a simple model which is particularly useful for predicting the behaviour in materials with strong pinning - the Bean critical state model [34, 35]. The Bean model makes two key assumptions; 1) there is a maximum current density that the superconductor can support, termed the 'critical current density', J_c. 2) Any electromotive force present within the

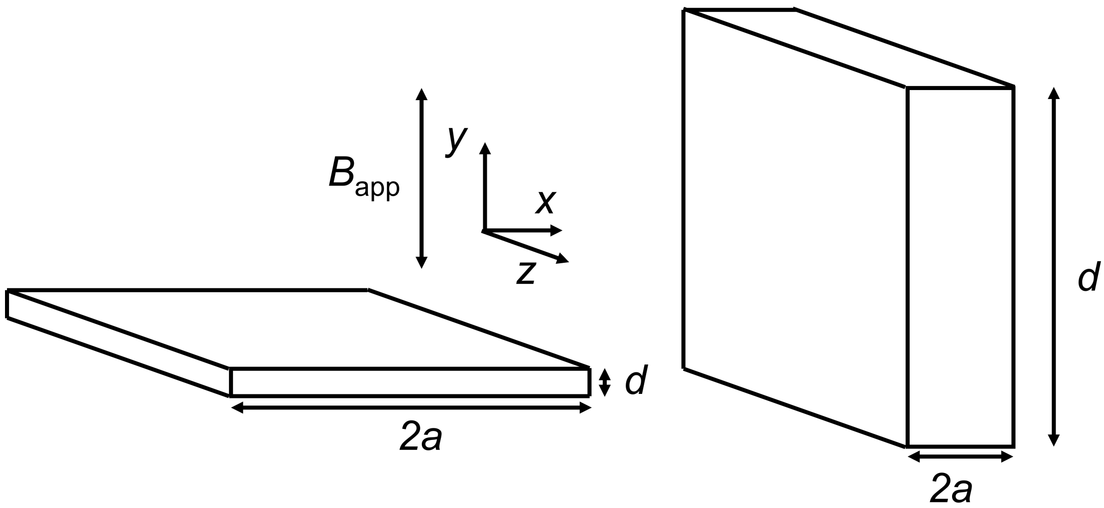

Figure 2.2: Two important geometries to which the Bean critical state model has been applied. A superconducting strip (left) in an external field applied perpendicular to the broad face of the conductor. A slab (right) in an external field applied parallel to the broad face of the conductor.

superconductor induces the full J_c. The critical current of a conductor with cross-section A is therefore given by $I_c = J_c A$. There are two particularly important geometries to which the Bean critical state model has been applied. A slab in parallel field and a thin film (strip) carrying a transport current. The geometries for these two cases are shown in figure 2.2.

2.3.1 Infinitely Thick Slab in a Parallel Field

Take first the case of a superconducting slab of width $2a$, infinite thickness d and length l, aligned with the x,y,z axes respectively. An external field, H_{app}, is applied along the y-axis, parallel to the thickness. In this scenario, the currents and fields only vary along the x-axis.

$$\partial_x H_{\text{y}} = \pm J_{\text{c}} \tag{2.2}$$

Induced screening currents flow in the z-direction to oppose the externally applied field. The Bean critical state model applied to this configuration is shown in 2.3. Shown are the field profiles over the width as the applied field is increased from zero to $2H_{\text{pen}}$ in plot (a) and reduced back to zero in plot (B). The corresponding

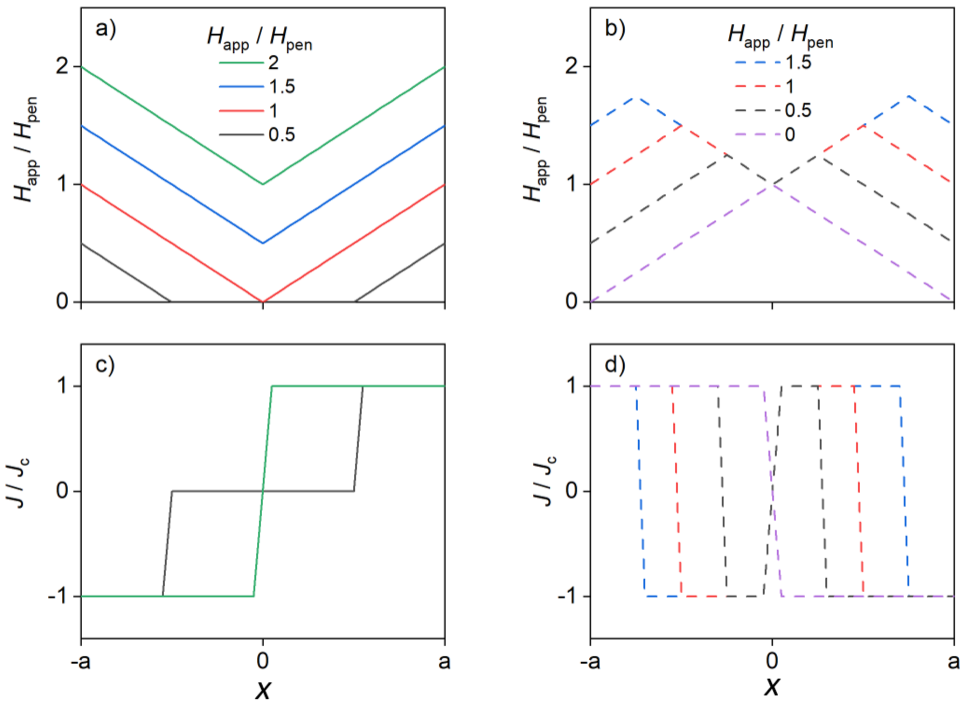

Figure 2.3: Magnetic field and current distributions within a thick superconducting slab with the field applied parallel to the broad faces of the conductor. Plots (a) and (c) show the magnetic field and current distributions for a virgin conductor across the conductor width as the applied field is ramped to twice the penetration field. Plots (b) and (d) show the magnetic field and current distributions as the applied field is then decreased back to zero

current profiles are given in plots (c) and (d). Once the external field is returned to zero, there are remnant screening currents which leave the slab with a net magnetic moment. Here, H_{pen} is the external field such that flux penetrates across the entire sample, $H_{\text{pen}} = J_{\text{c}}a$.

It is worth noting that there have been modifications to the Bean critical state model such as those by Anderson [36] and Kim [37] in which an arbitrary function is employed to describe the variations of the critical current density with magnetic field. However, a large number of fundamental properties can be explained with a constant J_{c} critical state model.

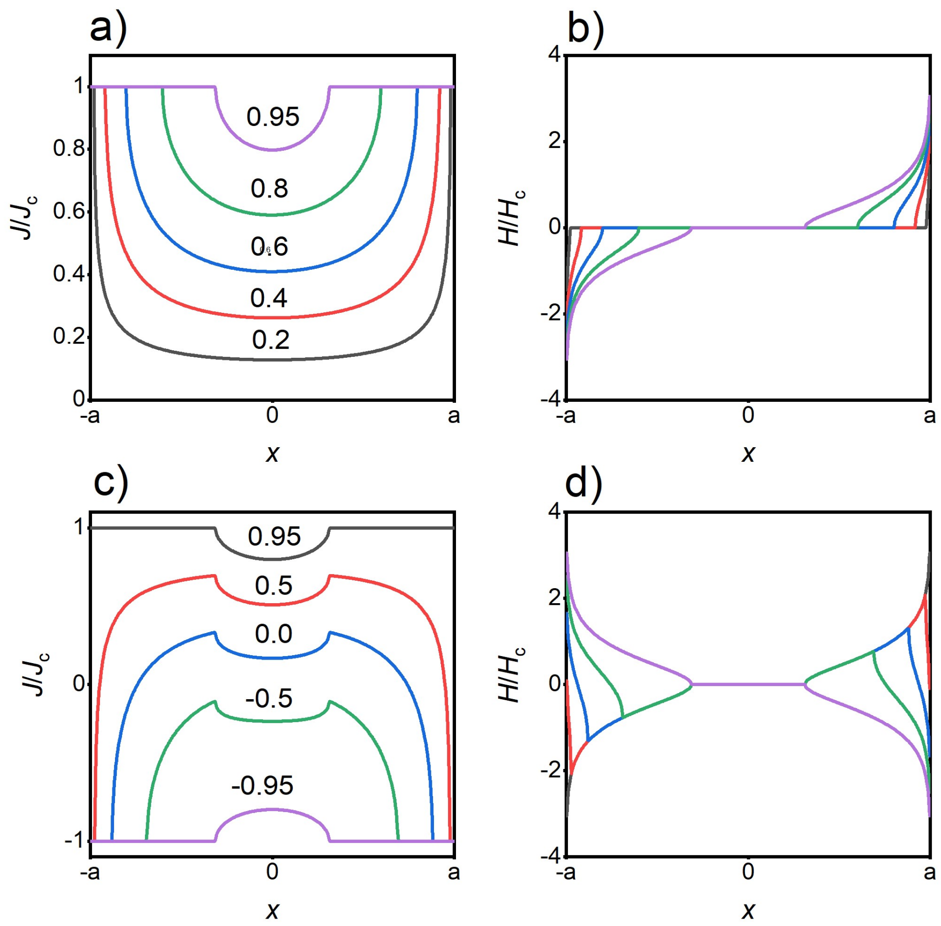

Figure 2.4: Magnetic field and current distributions within a thin superconducting film carrying a transport current. Plots (a) and (b) show the current density and magnetic field distributions across the width of a virgin conductor as the transport current is ramped from zero to 95% of I_c. Plots (c) and (d) show the current density and magnetic field as the current varies from 95% of I_c to -95% of I_c.

2.3.2 Infinitesimally Thin Film carrying a Transport Current

In practice, commercial HTS coated conductors are thin films which are often exposed to perpendicular magnetic fields. The current distribution within an infinitesimally thin film with constant J_c was first presented by Norris [38] where the strip problem was conformally mapped to that of a superconducting cylinder and then solved using the method of images. This work was later expanded in [39–41] to describe the current and field profiles in thin films carrying transport currents, exposed to external magnetic fields, and combinations of the two. The results are quite different to those from the slab model. For a superconducting thin film of width $2a$ along the x-axis, thickness $d \ll a$ along the y-axis, infinitely long in the z-direction and carrying a transport current parallel to the length, the following solutions for the current and perpendicular magnetic field distributions across the width are given by:

$$J_{\mathrm{z}}(x) = \frac{2J_{\mathrm{c}}}{\pi}\arctan\left(\frac{a^2-b^2}{b^2-x^2}\right)^{1/2} \quad \text{for } |x| < b \tag{2.3}$$

$$J_{\mathrm{z}}(x) = J_{\mathrm{c}} \quad \text{for } b < |x| < a \tag{2.4}$$

$$H_{\mathrm{y}}(x) = 0, \quad \text{for } |x| < b \tag{2.5}$$

$$H_y(x) = \frac{H_{\mathrm{c}}x}{|x|}\mathrm{arctanh}\left(\frac{x^2-b^2}{a^2-b^2}\right)^{1/2} \quad \text{for } b < |x| < a \tag{2.6}$$

$$\tag{2.7}$$

Under self-field conditions, there is a region of width b in the conductor,

$$b = a\sqrt{1-\frac{I_{\mathrm{t}}^2}{I_{\mathrm{c}}^2}} \tag{2.8}$$

inside of which no magnetic field penetrates and the current density is below J_{c}. Outside of this, the current density is J_{c}. The above expression is valid for a virgin conductor where the transport current is increased from zero to I_0. When an alternating current is applied, and the current is now at an intermediate current I, the current and field distributions can be found from a superposition of the virgin state and another conductor with twice the critical current and current (I_{t}-I_0).

$$J_{\downarrow}(x, I_{\mathrm{t}}, J_{\mathrm{c}}) = J(x, I_0, J_{\mathrm{c}}) - J(x, I_{\mathrm{t}} - I_0, 2J_{\mathrm{c}}) \tag{2.9}$$

$$H_{\downarrow}(x, I_{\mathrm{t}}, J_{\mathrm{c}}) = H(x, I_0, J_{\mathrm{c}}) - H(x, I_{\mathrm{t}} - I_0, 2J_{\mathrm{c}}) \tag{2.10}$$

for intermediate applied currents -$I_0 < I_{\mathrm{t}} < I_0$, there is a new penetration depth,

$$b' = a\sqrt{1-\frac{(I_0-I_{\mathrm{t}})^2}{4I_{\mathrm{c}}^2}} \tag{2.11}$$

inside of which flux is frozen in. By $I =$ -I_0, the virgin state has been reestablished with the transport current flowing in the opposite direction. Examples of current and field distributions during virgin ramping and upon current reversal are shown in figure 2.4.

2.4 E-J Power Law

The Bean critical state model assumes a step relationship between the current density and the electric field. The maximum lossless current density is the critical current density J_c. This model is applicable to many type-I superconductors and some HTS materials, however there are many where the onset of dissipation is continuous and a critical current is not so well defined. Instead, it is a universal practice to use a power-law

$$\mathbf{E} = \frac{E_c}{J_c}\left|\frac{J}{J_c}\right|^{n-1}\mathbf{J} \tag{2.12}$$

to describe the I-V characteristics of superconducting materials where the critical current density J_c and the flux creep exponent n are the two fitting parameters. As discussed by Rhyner [42], the power law provides an interpolation between the two limiting cases of an Ohmic material ($n = 1$) and the critical state model ($n = \infty$). The power-law is used to describe many high temperature superconductor materials with the variation in behaviour as a function of n shown in figure 2.5. This is based on a wide range of transport measurements which have empirically demonstrated that the power law can fit a substantial range of HTS materials including BSCCO, GdBCO and YBCO [43].

2.4.1 Constant vs Field Dependent J_c

The critical current density J_c is one of the most important parameters when it comes to designing superconducting devices. There are a number of phenomena exhibited by superconducting materials that can be explained assuming a field independent function for J_c. In practice however, J_c is typically dependent on temperature, the local magnetic field and its orientation relative to the wire [43]. In the case of commercially manufactured $ReBa_2Cu_3O_7$ wire, J_c can be highly anisotropic with respect to the applied field angle which can result in large variations in the local I_c along the length of a given wire. In many cases, it becomes desirable to account for this variation within the material. There exist a number of analytical models which assume J_c depends on the applied field (such as Kim's modification of the bean

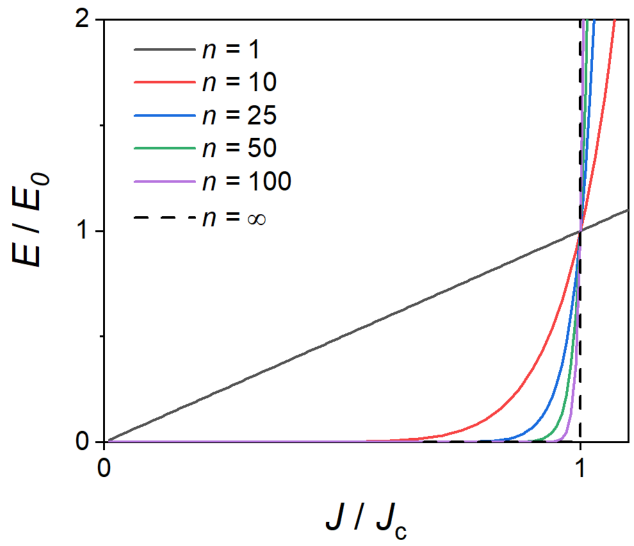

Figure 2.5: The E-J power law with varying flux creep exponent n. Ohm's corresponds to $n = 1$ while the critical state model is given by $n = \infty$

model [44]).

The data presented in figure 2.6 shows the variation in performance of commercial wire (manufactured by SuperPower) as the applied magnetic field is orientation relative to the wire is varied.

Measurements of J_c can also be obtained from superconducting films or bulks through parameter fits to measured magnetisation curves [44–46]. However, magnetisation current distributions differ substantially from the transport condition, leading to different internal field distributions, which then affect the local value of $J_c(B)$. Furthermore, the absolute accuracy of current values obtained via this approach is highly dependent on the homogeneity of the sample, as well as prior calibration of the magnetometer instrument and geometric demagnetisation factors. Reel-to-reel magnetisation measurements are also routinely made on HTS tapes [47, 48], but are subject to similar accuracy limitations, and this is also the case for magneto-optical techniques [49–51].

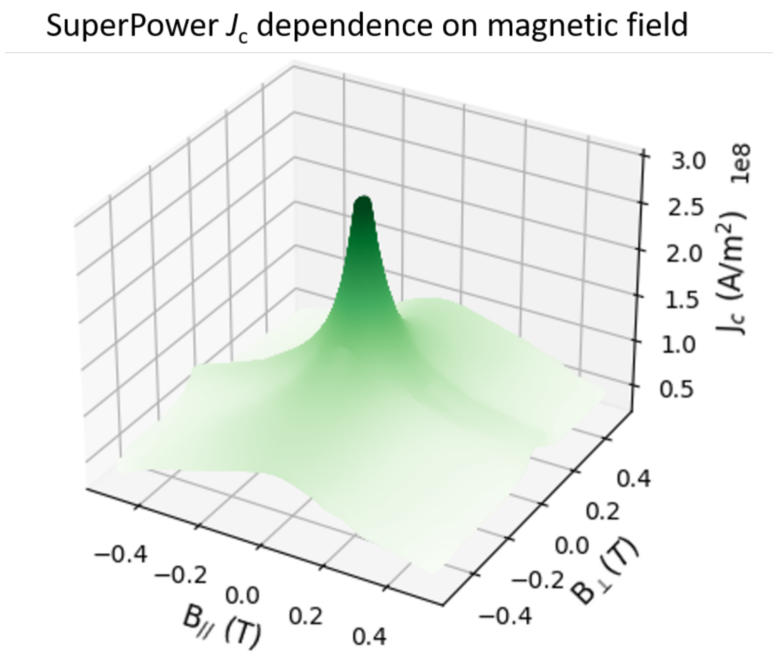

Figure 2.6: Example of the J_c field dependence of a SuperPower coated conductor measured in the SuperCurrent system at Robinson Research institute

2.5 Dynamic Resistance

2.5.1 Slabs and Strips

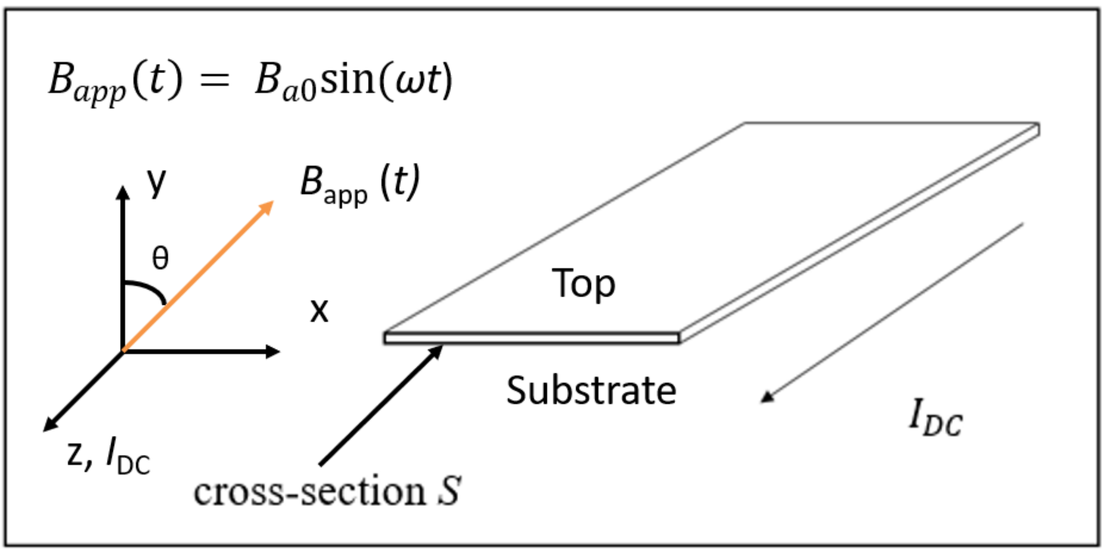

Figure 2.7: Example of a superconducting strip in an environment that leads to dynamic resistance. A transport current flows parallel to the length of the tape and an external AC field is applied at some angle relative to the tape.

When superconducting devices are exposed to time-varying fields while carrying DC transport currents, dissipative interactions occur between moving flux vortices and the transport current, generating a time-averaged net DC electric field [52]. This electric field results in an effective resistance, termed the dynamic resistance [53, 54]. This DC resistance is conventionally discussed in terms of the net volume of flux which traverses the DC current carrying region of the superconductor during each cycle [52, 55, 56], which requires that work is done. There exist a number of studies on this subject including theoretical analysis [53, 54, 56–64], experimental measurements [61, 62, 65–78] and finite element modelling [62, 63, 74–84]. Much of this recent work has been motivated by a need to understand loss in coated conductors that may occur in HTS AC machines such as motors, generators, and dynamos.

2.5.1.1 Analytical Derivation

As described by [53, 58, 60], when a superconducting thin film is exposed to an alternating magnetic field, magnetisation currents flow in the outer regions of the conductor. If the amplitude of the applied field is less than some sample-dependent threshold value B_{th}, the applied field fails to fully penetrate the conductor and there is an interior region of frozen flux. Any transport current flowing in this region does not experience a change in magnetic field and is able to flow with zero electrical resistance. However, once B_{th} is exceeded this interior region experiences a change in flux and a non-zero dynamic resistance is observed. This resistance is due to the work done by the power supply in applying a Lorentz force to the net flux traversing the film. Note here that this view is adopted in order to obtain an analytical expression for the DC resistance. However, as will be demonstrated in chapter four, the transport current does not occupy a constant fraction of the conductor, nor is it confined to the centre of the tape. Both [58, 61] state that for a superconducting strip of width $2a$ and thickness d filling the space $|x| \leq a$, $|y \leq d/2$ and $|z <\infty$, centred at $(x,\ y) = (0,\ 0)$ and experiencing a homogeneous magnetic field $B_{\mathrm{app}}(t) = B_{\mathrm{a0}}$ $\sin(\omega t)$ applied along the y axis, the total dynamic resistance per cycle is given by

$$\frac{R_{\mathrm{dyn}}}{fL} = \frac{4a}{I_c}(B_{a0} - B_{th}) \tag{2.13}$$

Several differing expressions have been derived for the threshold field of a single strip are compared to experimental and numerical results in this thesis. They are listed here along with an expression for the threshold field of a slab in a parallel field, and with brief description of how each expression is derived. All expressions are given in terms of the reduced current $i = I_{\mathrm{t}}\ /\ I_{\mathrm{c}}$ where I_{t} is the applied transport current. The threshold field for a slab is given by

$$B_{\mathrm{th,slab}} = \mu_0 J_{\mathrm{c}} a(1-i) \tag{2.14}$$

This expression is given in [58]. The prefactor is the penetration field for a slab given from the Bean critical state model and multiplied by a fill factor representing space lost to the transport current. There are a number of differing expressions for the threshold field in strip geometries. These are listed below.

$$B_{\mathrm{th,strip}} = \frac{\mu_0 J_{\mathrm{c}} d}{2\pi}\left[\frac{1}{i} ln\left(\frac{1+i}{1-i}\right) + ln\left(\frac{1-i^2}{4i^2}\right)\right] \tag{2.15}$$

is first given in [58]. This is derived using the conformal mapping methods outlined in [38–40]. As discussed in [85], the literature surrounding these derivations typically provide a very condensed description of the conformal mapping technique, hampering adoption in the wider community. However, [85] demonstrates that these expressions can be arrived at numerically for various HTS geometries.

$$B_{\mathrm{th,Jiang}} = \frac{4.9284\mu_0 J_{\mathrm{c}} d}{2\pi}(1-i) \tag{2.16}$$

Here, [61] describes B_{th} as the field at which it is no longer energetically favourable for flux to be screened from the central region of the conductor. In the limit of the transport current tending to zero, B_{th} occurs at the peak of the normalised AC magnetisation loss [39]. This is computed numerically and then multiplied by a filling factor to account for space in the conductor lost to the transport current [56].

An expression has been proposed for the threshold field in a parallel connected and vertically stacked HTS tapes. This was derived concurrently with the finite element analysis of stacks presented in this thesis. In that paper, B_{th} for a stack is given by [86]

$$B_{\text{th,stack}}(N) = \frac{\mu_0 a^{0.8} I_c(1-i)}{2D^2 ln\left[cosh\left(\frac{\pi a}{D}\right)\right](N^{0.8}-1)+\pi^2 a^2} \tag{2.17}$$

Equation 2.17 uses the same linear superposition of screening and transport currents (in conjunction with the external susceptibility computed by Fabbricatore [87]) for infinite vertical stacks. This expression accounts for both shielding and demagnetising effects from the neighbouring tapes.

2.5.2 Hollow Slab

In the previous section, the DC output of a single continuous piece of superconductor was discussed. However, during the writing of this thesis, it was demonstrated that a general expression for the dynamic resistance of a hollow slab (superconducting loop) can also be obtained [88]. The derivation is presented below

Consider a hollow superconducting slab which has four branches as shown in figure 2.8 (a). The left and right branches have width b and the hollow gap has width $2l$, all in the x-direction. The slab has length L along z and thickness w in y. A homogeneous magnetic field, $\boldsymbol{B}_{\text{app}} = B_{\text{a0}}\sin(\omega t)\hat{y}$, is applied normal to the loop and the transport current is flowing in the z-direction. In this geometry, it is assumed that $L \gg 2(b+l)$ and $w \gg 2(b+l)$. Thus there is no variation in the magnetic field in the y-direction.

Application of Faraday's law to the loop gives

$$\oint_{c=\Lambda_{1324}} \boldsymbol{E}\cdot \boldsymbol{dl} = \int_S \frac{d\mathbf{B}}{dt}\cdot \boldsymbol{dS} \tag{2.18}$$

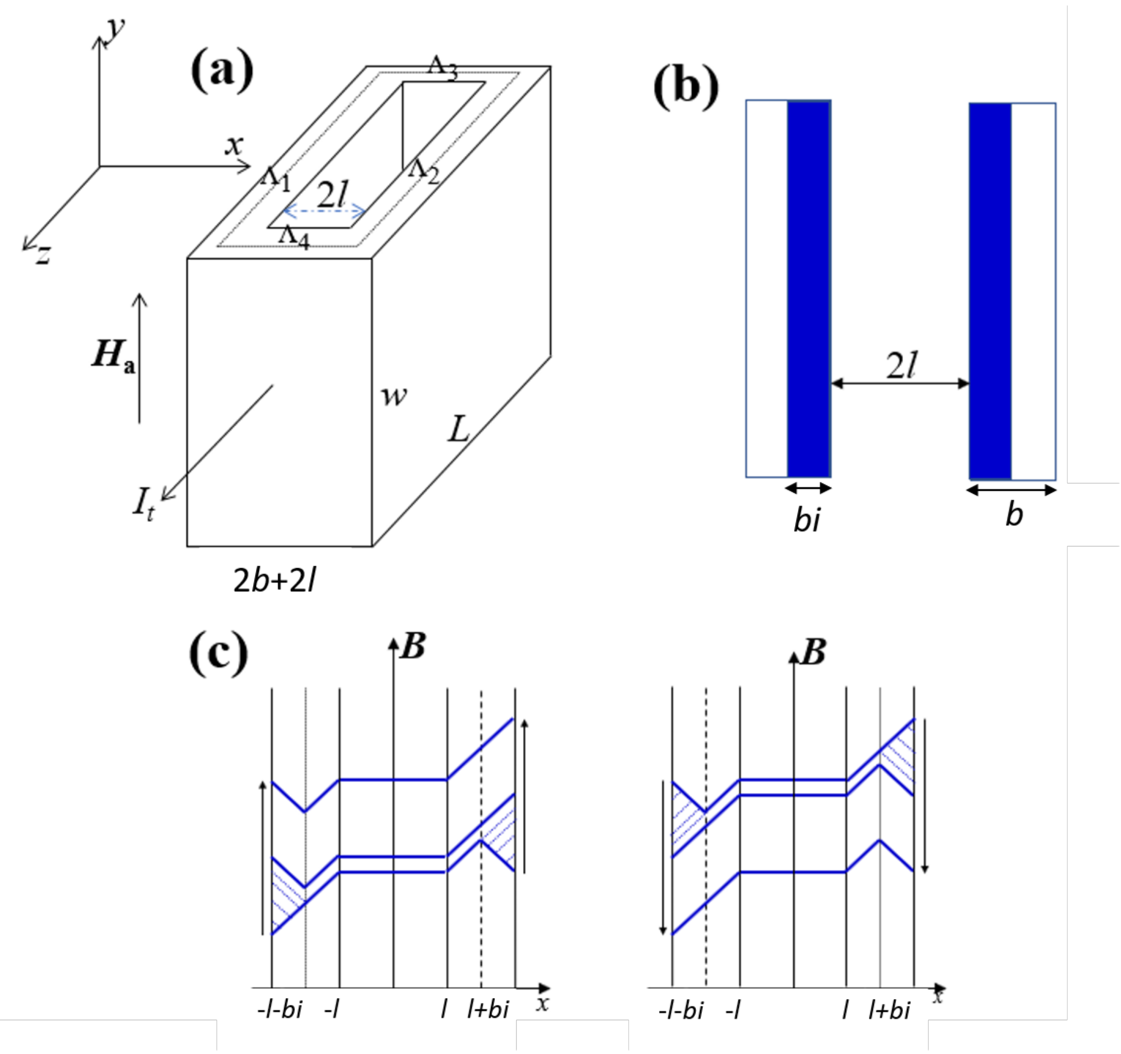

Figure 2.8: The geometry of the superconducting hollow slab and the magnetic field distribution within the loop during one ac-field cycle. (a) 3D schematic of the geometry showing the superconducting hollowed slab, formed by 4 branches, the left and right branches both having width, b, the distance between these two branches is $2l$, the thickness of the slab is w, and the length of the slab is L. (b) Cross-section of the slab under time-varying magnetic field. The transport current flows in the inner part of each branch (shown in blue), whilst shielding currents flow in the outer parts (shown in white). Here, $i = I_t/I_c = 0.5$. (c) Magnetic field profile inside the loop. Left figure: Profile whilst the applied field increases, the electric-centre line is located at -l-bi. Right figure: Profile whilst the applied magnetic field decreases, the electric-centre line is shifted to l+bi. Reproduced with permission from [88].

where S is the area formed by the contours $\Lambda_1, \Lambda_2, \Lambda_3$, and Λ_4. The slab is assumed to be sufficiently thick along Λ_3, and Λ_4 so that no flux penetrates the loop through the front and back sides. Therefore, the electric field along Λ_3, and Λ_4 is zero such that

$$\int_{\Lambda_2} \boldsymbol{E} \cdot \boldsymbol{dl} - \int_{\Lambda_1} E \cdot \boldsymbol{dl} = \int_S \frac{d\mathbf{B}}{dt} \cdot \boldsymbol{dS} \tag{2.19}$$

The problem is 1D where the electric field and current density are parallel, each having a component only in the z-direction and the magnetic field has a component only in the y-direction. It is further assumed that these slabs behave according to the Bean critical state model with a constant J_c. The threshold field is the same for a single slab and is given by equation 2.14.

When $\boldsymbol{B}_\mathrm{app}$ is applied to the loop, the transport current will occuppy the central regions of the inner edge of each branch, as shown in figure 2.8 (b). If the amplitude of the applied field is less than the threshold field, ie, $B_\mathrm{a} < B_\mathrm{th,Slab}$, then neither branch is fully penetrated by the external field and the current density on the inner edge of each branch is less than J_c. As a result, the transport current carrying regions experience no electric field. If the applied field amplitude is larger than $B_\mathrm{th,Slab}$, then each branch is fully penetrated such that the screening and transport currents interact. In the following, only the case where $B_\mathrm{app} > B_\mathrm{th,Slab}$ is considered. During the part of the cycle when the magnetic field is increasing, ($\uparrow$), the zero crossing of the electric field is positioned at the left hand edge of the transport current [53, 57], x = -l-bi. Choosing this location for contour Λ_1 and any position of the transport current, $x \in$ (-l-bi,-l)$\cup$ (l,l+bi) as Λ_2, equation 2.19 becomes

$$E_\uparrow(x,t) = (x + l + bi)\frac{dB}{dt} \tag{2.20}$$

During the descending ($\downarrow$) part of the cycle, the electric zero crossing is now located at (l+bi). Now choosing this location for Λ_2 and $x \in$ (-l-bi,-l)$\cup$ (l,l+bi) as Λ_1, equation 2.19 becomes

$$E_{\downarrow}(x,t) = -(l+bi-x)\frac{dB}{dt} \tag{2.21}$$

The EC electric field, E_{DC} is given by the mean value over one period of the applied field, T, of the spatially averaged electric field in the transport current carrying region.

$$E_{\mathrm{DC}} = \frac{1}{T}\int_T \frac{1}{2bi}\int_X E(x,t)dxdt \tag{2.22}$$

where $X = x \in$ (-l-bi,-l)$\cup$ (l,l+bi). Substitution of equations 2.20 and 2.21 into 2.22 yields

$$E_{\mathrm{DC}} = \frac{4}{T}(l+bi)(B_{\mathrm{a}} - B_{\mathrm{th,Slab}}) \tag{2.23}$$

where $\mathrm{d}B/\mathrm{d}t = \pm 2(B_{\mathrm{a}}$-$B_{\mathrm{th,Slab}})$. It is important to note that equation 2.23 relies on having a well defined electric centre line [53]. As we shall see in chapter 7, at low transport currents the electric centre line does not lie in either branch, meaning that equation 2.23 is not applicable. However, it is clear that as $l \to 0$, the expression for the dynamic resistance of a single piece of conductor, equation 2.13 is recovered.

2.6 Numerical Finite Element Methods

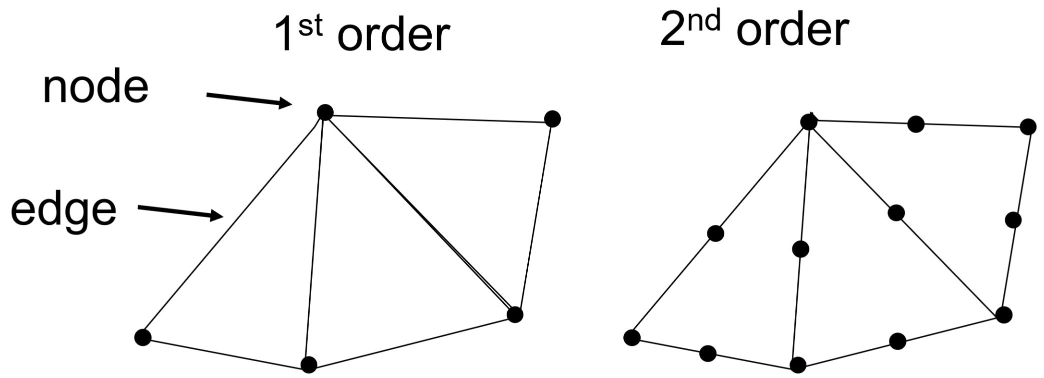

Figure 2.9: Diagram showing 1^{st} and 2^{nd} order finite elements. The elements are comprised of edges and nodes.

As discussed in section 2.5, analytical models for superconducting devices exist for simple geometries. For more complicated shapes and conditions, a number of numerical methods have been developed in which Maxwell's equations are solved in conjunction with an E-J power-law that describes the superconductor resistivity. The numerical methods are typically named after the variables in which the governing partial differential equations are given. These include the $\boldsymbol{A}$-V (vector and scalar potentials) [89–91], $\boldsymbol{T}$-$\boldsymbol{A}$ (current and vector potentials), [92, 93], $\boldsymbol{H}$ (magnetic field) [94, 95], and minimum electromagnetic entropy (MEMEP) [96, 97].

In this thesis, all of the chapters include finite element numerical analysis (chapters 6 and 7 present data solely from numerical methods) which has been performed using the $\boldsymbol{H}$-formulation, implemented in the commercial software COMSOL. This software solves Maxwell's equations in a given geometry for a collection of boundary conditions and constitutive relations for the magnetic and electric fields. The $\boldsymbol{H}$-formulation has been chosen as it is capable of solving numerical problems with high aspect ratios and non-linear resitivities as demonstrated in its extensive use in the existing literature [81, 94, 95]. It is also particularly easy to implement with the commercial software COMSOL when compared with other methods which are developed and implemented 'in-house' such as MEMEP. The numerical method used is the finite element method, which works by discretizing the continuous space where the problem is defined into a finite number of points or nodes where the differential equations will be solved. The nodes are connected into sub-domains which are known as elements. The solution is arrived at by solving a collection of equations across all of the nodes and then interpolated for the space between. The solution obtained in each element provides an approximation to the true solution of whatever partial differential equation is being considered.

Figure 2.9 gives an example of 2D triangular elements that are 1^{st} and 2^{nd} order. Each element consists of three edges with either corner nodes (1^{st} order) or corner and side nodes (2^{nd} order). The interpolation between nodes is described by a polynomial and the element order refers to the order of the polynomial. Using higher order elements is more computationally expensive as they have more unknown coefficients which must be solved for while simultaneously offering curvature of the solution between elements. In the following finite element models, first order elements are used in both the superconducting and air domains [98].

3
Methods

This chapter provides an outline of the various experimental procedures and specifics concerning numerical methods. This includes a description of finite element models, differential equations, and boundary conditions which these models solve as well as the experimental equipment and measurement routines used in later results chapters.

3.1 The Finite Element Method

In this thesis, a number of superconducting configurations are modelled. All are 2D with the HTS cross-section in the xy-plane, and having infinite length along z (see figure 2.7).

3.1.1 $\boldsymbol{H}$-Formulation

As mentioned above, the $\boldsymbol{H}$-formulation solves Maxwell's equations in terms of the magnetic field $\boldsymbol{H}$. The space is divided into two sub-domains the superconducting domain such as a tape, stack or loop, and the surrounding air. It is assumed the magnetic flux density and the magnetic field are related by

$$\mathbf{B} = \mu_0 \mathbf{H} \tag{3.1}$$

in all domains (ie the magnetic field is generated by conduction charge carriers rather than by bound currents [99]). Faraday's and Amperes laws expressed in terms of $\boldsymbol{H}$ are given by

$$\nabla \times \mathbf{H} = \mathbf{J} \tag{3.2}$$

and

$$\nabla \times \mathbf{E} = -\mu_0 \frac{d\mathbf{H}}{dt} \tag{3.3}$$

without the displacement current. Because the $\boldsymbol{B}$ lies in the plane of the conductor cross-section, the vector potential satisfying

$$\nabla \times \mathbf{A} = \mathbf{B} \tag{3.4}$$

$\boldsymbol{A}$ only has a component in the z-direction. Noting that we have already assumed translational symmetry along the z-direction, $\nabla \cdot \boldsymbol{A}$ is therefore zero and the Coulomb gauge condition is satisfied. Amperes law in terms of the vector potential then simplifies to a Poisson equation

$$\nabla^2 \mathbf{A} = -\mu_0 \mathbf{J} \tag{3.5}$$

Equipped with both $\boldsymbol{E}$ and $\boldsymbol{A}$, the electric potential can be found from the relationship

$$\mathbf{E} = -\nabla V - \partial_t \mathbf{A} \tag{3.6}$$

for comparison with values measured experimentally. A magnetic field boundary condition is imposed on the perimeter of the surrounding air domain using the magnetic field node in Comsol. This node enforces

$$\mathbf{n} \times \mathbf{H} = \mathbf{n} \times \mathbf{H}_0 \tag{3.7}$$

on the chosen boundary where the external magnetic field, $\mathbf{H}_0$, is prescribed by the user. Throughout this thesis, $\mathbf{H}_0$ is either zero (to model self-field conditions) or a sinusoidal function ($B_{\mathrm{app}} = B_{\mathrm{a0}}\sin(\omega \mathrm{t})$ to simulate the given configuration inside a uniform, alternating magnetic field. It is assumed that the electric field and current are parallel and have a component in the z direction while the magnetic field has components in the plane (see figure 2.7). The electric field and current density are related by

$$\mathbf{E} = \rho \mathbf{J} \tag{3.8}$$

The resistivity in air, $\rho_{\mathrm{n}} = 1\ \Omega\mathrm{m}$. In the superconducting domain, the resistivity is given by a power law

$$\rho_{\mathrm{sc}} = \frac{E_0}{J_c} \left| \frac{J_z}{J_c} \right|^{n-1} \tag{3.9}$$

Field dependent J_c and n values are incorporated within the model via lookup tables (the wire characterisation process which generates these lookup tables is discussed in section 3.2.1).

3.1.2 Meshing and Error Tolerances

An important aspect of finite element modelling is the setting of error tolerances and the meshing of the finite domain. The impact of changing the tolerance settings and using different shapes for the finite elements are discussed here for a model of a single HTS tape with a constant J_c

There are two important error tolerances which are set by the user, the absolute tolerance and the relative tolerance. Both of these parameters are used internally in COMSOL's time dependent solver to determine whether or not the solution is convergent. The relative tolerance gives the largest acceptable solver error relative to the size of each state as time steps are taken. The absolute tolerance provides the largest acceptable solver error relative to the size of each state when the state values are near zero [98]. If the determined relative or absolute error, exceeds either of these parameters, the solver reduces the time step and tries again.

When meshing the model, the mesh density must be greatest where it is expected that there will be large spatial variations in the computed variables. In the models used through this thesis, the greatest spatial variation is expected within the superconducting domain and the immediately surrounding air. Figure 3.1 shows examples of the meshing in a model comprised of a single tape. Figure 3.1 (a) shows the entire circular air domain and (b) a closer view towards the HTS tape.

Three different examples of meshing for the HTS cross-section are considered; triangular, square and rectangular which are shown in (c), (d), and (e). An *E-I* test for a single HTS tape is simulated where J_c and n are assumed to be constant (100 A and 30 respectively). The model is run using the three different element

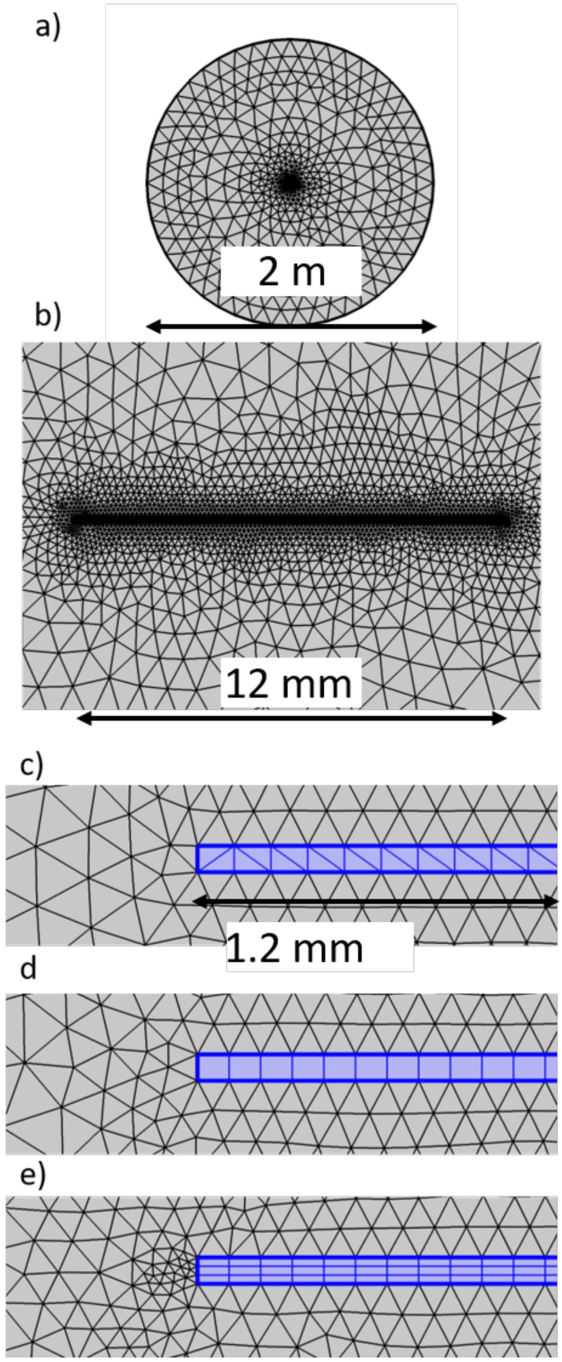

Figure 3.1: Meshing of finite element domains for a single HTS tape. Plot (a) shows the entire model with a view of the surrounding air domain and meshed with triangular elements. (b) shows a magnified image of the meshing nearer to the tape. (c-e) shows examples of the meshing inside the HTS tape using triangular, square, and rectangular meshing elements.

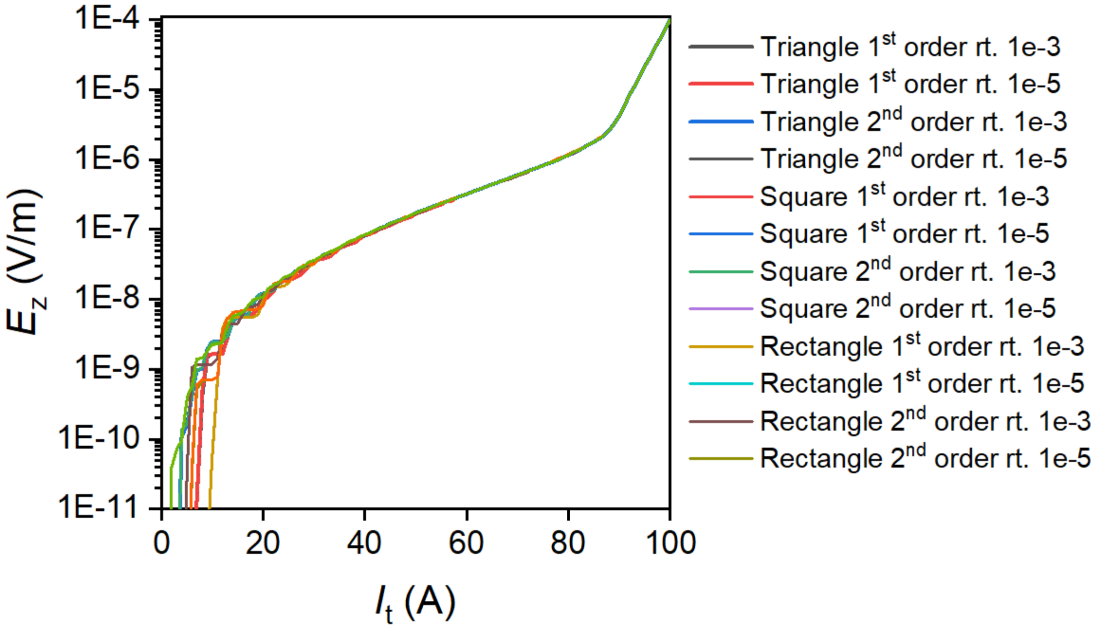

Figure 3.2: Calculated *I*-*V* response of a superconducting tape with a linearly increasing transport current for triangular, square, and rectangular mesh elements and varying relative tolerance settings. The absolute tolerance was set to 1e-7.

shapes (both first and second order) for the HTS domain and for two different values of the relative tolerance, 1e-3 and 1e-5. The results are given in table 3.1 and the resultant *E*-*I* curves are shown in figure 3.2. The computed *E*-*I* curves show little variation in the electric field above 1e-7 V/m regardless of the choice in element shape, order, and relative tolerance. In all models used throughout this thesis, first order elements are used in the HTS domain and the absolute and relative tolerances are set to 1e-3 and 1e-5 respectively [98].

Shape	Order	DoF	Time (s)
triangle	1st	6739	24 / 43
triangle	2nd	22394	60 / 87
square	1st	7212	31 / 43
square	2nd	24104	192 / 163
rectangle	1st	7729	27 / 45
rectangle	2nd	26094	151 / 228

Table 3.1: Table detailing meshing shape, degrees of freedom to be solved and solver time for relative tolerance settings of 1e-3 (left) and 1e-5 (right).

3.1.3 Visualising Data through Contour Plots

The 2D finite element models used in this thesis calculate currents and fields within the HTS wires which vary in both space and time. To graphically visualise these calculated values, it is convenient to consider the equivalent 'sheet value' that would be present in a planar superconductor of infinitesimal thickness. These sheet values are obtained by integrating (or averaging depending on the variable of interest) over the thickness of the superconductor layer, d, as shown in the following equations. The geometry is the same as that shown in figure 2.7. These equations define the equivalent sheet current density K_z, the equivalent sheet critical current K_c, the equivalent sheet perpendicular magnetic field B'_y and the equivalent sheet electric field E'_z.

$$B'_y(x,t) = \frac{1}{d}\int_{-\frac{d}{2}}^{\frac{d}{2}} B_y(x,y,t)dy \tag{3.10}$$

$$E'_z(x,t) = \frac{1}{d}\int_{-\frac{d}{2}}^{\frac{d}{2}} E_z(x,y,t)dy \tag{3.11}$$

$$K_z(x,t) = \int_{-\frac{d}{2}}^{\frac{d}{2}} J_z(x,y,t)dy \tag{3.12}$$

$$K'_c(x,t) = \int_{-\frac{d}{2}}^{\frac{d}{2}} J_c(x,y,t)dy \tag{3.13}$$

3.2 Experimental Methods

The following section outlines the various experimental procedures employed to collect the experimental data presented in chapters 4 and 5. These include transport (in self-field and AC field conditions) and magnetic field measurements. While experiments typically involved combinations of these procedures run in parallel, they can be broken down into the following techniques.

3.2.1 HTS Wire Characterisation

As discussed in section 3.1, field dependent J_c values are included in the FE model using lookup tables. The data within the lookup tables were meausured using the Super-Current system [32, 100] from Robinson Research institute. Super-Current I_c measurements are performed by mounting a coated conductor on a G10 holder positioned between a superconducting magnet. This sample holder is able to freely rotate within the bore of the copper magnet and can obtain data over a full 360°. The Super-Current system is capable of applying magnetic fields up to 10 T, however, no characterisation data was obtained at fields greater than 500 mT within this thesis.

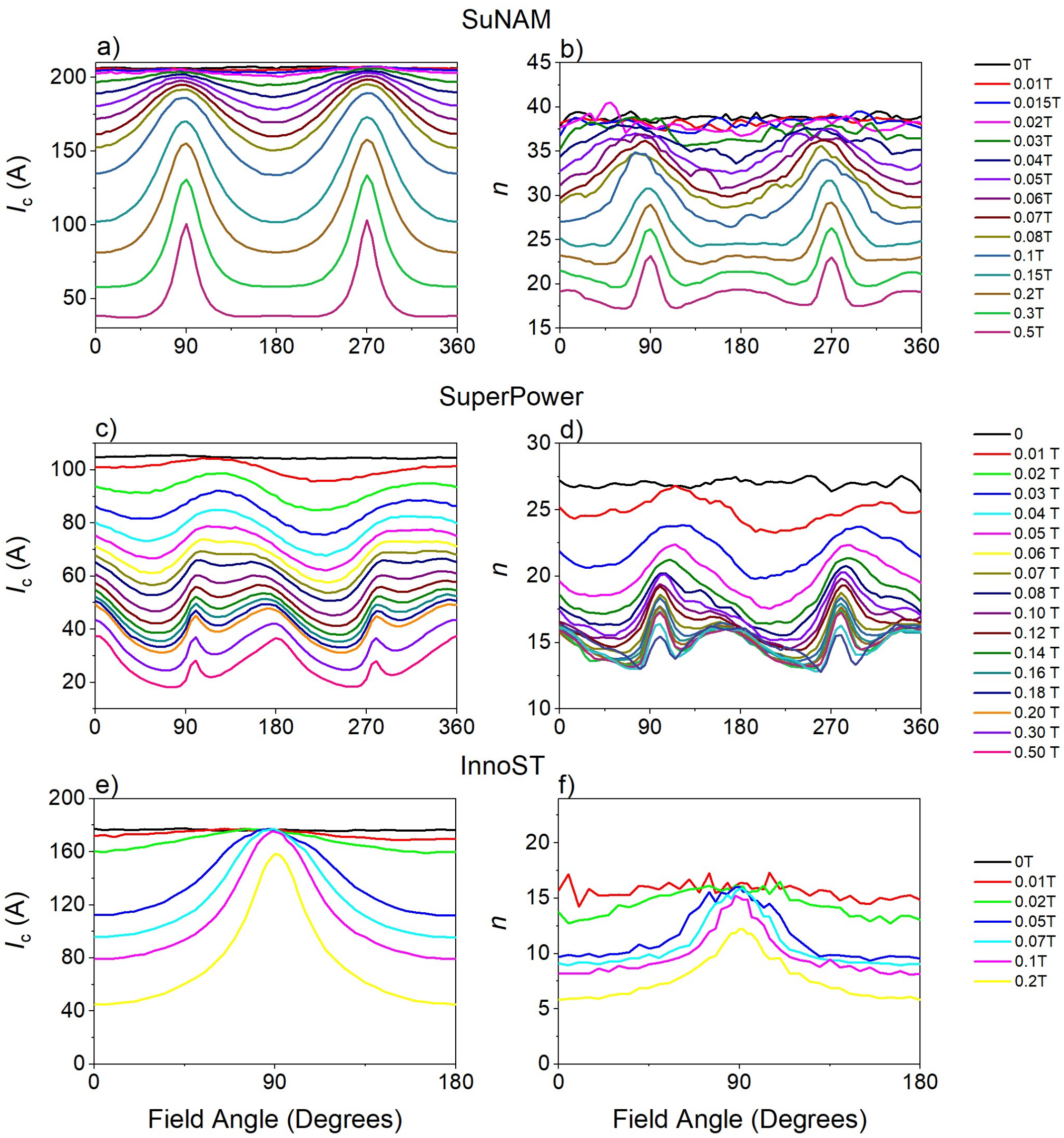

Figure 3.3: Experimentally measured I_c(B, θ) and n(B, θ) data at 77 K as a function of applied magnetic field amplitude and orientation relative to the sample ($\theta = 0°$corresponds to the field applied perpendicular to the conductor). Plots (a), (b) show the SuNAM data, plots (c), (d) show the Super Power data, plots (e), (f) show the InnoST data

In this work, all results were performed in LN_2 environments and all SuperCurrent data was obtained at 77 K. An example of the measured $I_c(B,\theta)$ and $n(B,\theta)$ data for three commercially manufactured tapes is presented in figure 3.3.

3.2.2 Stepped *I-V* Measurements

In chapter four of this thesis, a number measurements are made as the transport current is increased. Both stepped and linearly ramped transport measurements are performed.

In stepped transport measurements, the voltage is measured along the length of an HTS coated conductor submerged in a LN_2 bathtub. Transport currents were applied using an Agilent 6680A power supply with a 2 second period between steps and voltage measurements. The voltage was measured using twisted pairs of enamelled copper wire connected to an Agilent 34420 nano-voltmenter. The transport currents were increased in 2 A increments from zero to 80% of the target current. The steps were then reduced to 0.5A to obtain finer resolution around the target current.

Note that as discussed earlier, current cycling results in a remnant magnetisation in the conductor. Where relevant, virgin measurements refer to a conductor which has been reheated above T_c (90 K) and had any remnant super-currents purged prior to that measurement being made.

3.2.3 Ramped *I-V* Measurements

I-V measurements were also taken during linear ramping of an injected transport current. The Agilent 6680A was driven using an analogue signal produced from an NI DAQ USB-9263 analogue output module. The current was measured using a HAL-600 open loop current sensor. The measured voltage signal was amplified using an A10 DC nano-volt amplifier connected to a NI DAQ USB-6211 module.

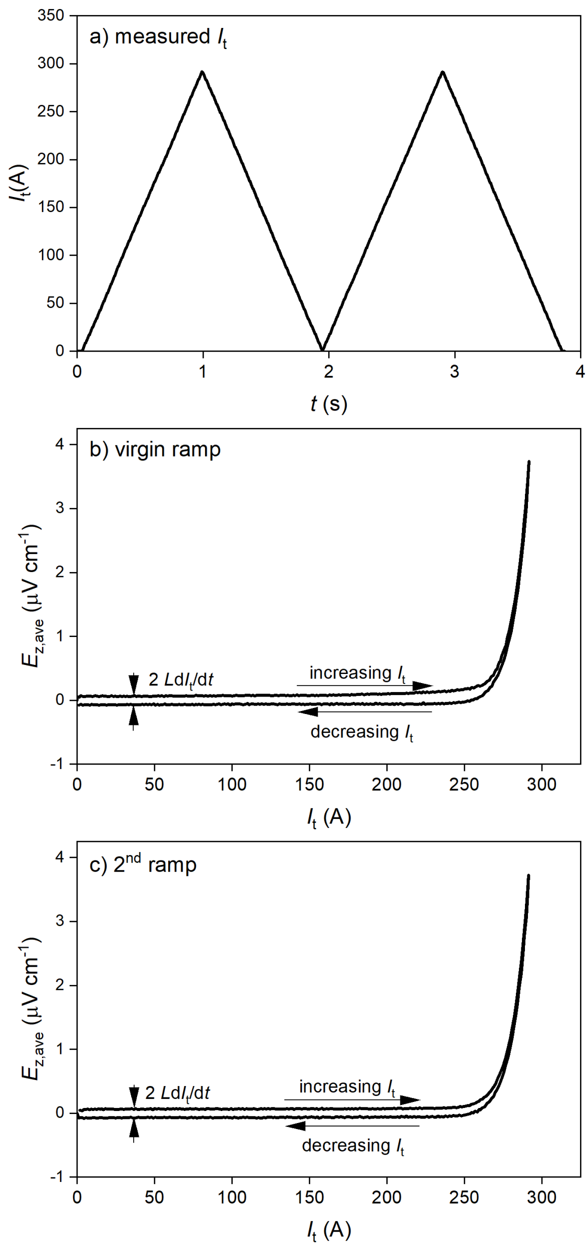

Figure 3.4: Example of I-V measurement on SuperPower wire with $\mathrm{d}I_\mathrm{t}/\mathrm{d}t$=300As^{-1}. (a) the measured current using the open loop sensor (b) shows the measured electric field on ascending and descending legs of the virgin cycle. (c) shows the measured electric field on ascending and descending legs of the 2$^{\mathrm{nd}}$ cycle with the inductive pickup visible in both cycles.

As the current is ramped, there is a constant inductive component which must be subtracted to obtain the signal due solely to the transport current flowing within the conductor. Figure 3.4 shows an example of a dataset from a ramped transport measurement. Figure 3.4 (a) shows the current measured using the open loop sensor. Also shown are the voltage measurements obtained on ascending and descending legs of the measurement for a virgin conductor (plot (b)) and during the second cycle (plot (c)). The inductive voltage to be subtracted is shown in both cases.

3.2.4 Surface-Field Measurements

Throughout this thesis, magnetic field data has been obtained using one of two separate Hall Sensor Arrays. The two arrays were employed to measure orthogonal components of the magnetic field at the surface of a HTS coated conductor.

The perpendicular magnetic field was measured at the surface of five different HTS tapes from three different manufacturers. These comprised ReBCO tapes of different widths from SuperPower: 12 mm wide (SCS12050-AP M4-382-5); 4 mm wide (SCS4050-AP M3-774); and 2 mm wide (SCS2030-AP M4-479-3 0910). A 12 mm wide ReBCO tape from Sunam (HCN12500-190726) was also studied, as well as a 4 mm wide Bi-2223 tape manufactured by InnoST.

A linear array of cryogenic Hall sensors (Arepoc THV-MOD 7U) was mounted within a G10 board, flush to its surface. The sensors were aligned so that they capture the perpendicular magnetic field component at the tape surface. The array consists of seven individual sensors with each having an active area of 0.1 mm^2, Each sensor was calibrated before use, with signals measured using a custom made low-noise instrumentation amplifier. The Hall sensors have a horizontal spacing of 1.5 mm.

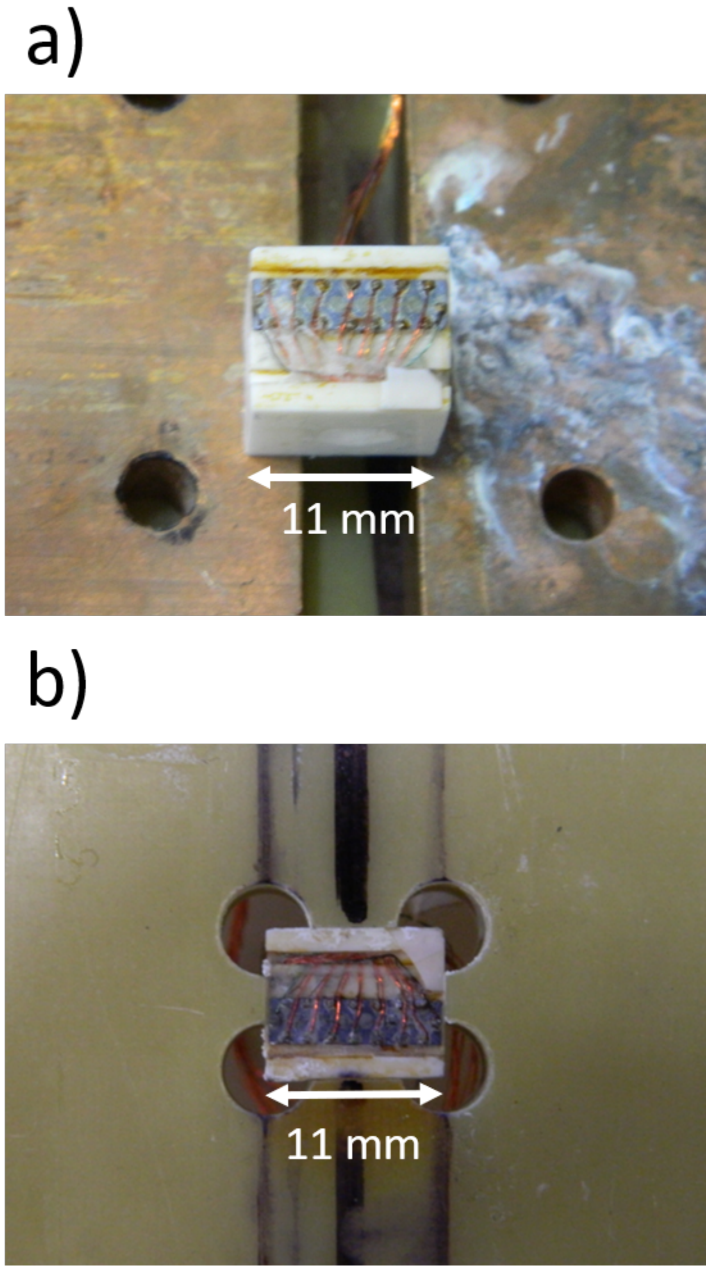

Figure 3.5: (a) shows the Arepoc Hall Sensor array, (b) shows the same array housed inside a G10 sample board. The black lines indicate where the coated conductor sits with the array positioned approximately 1mm from the conductor surface

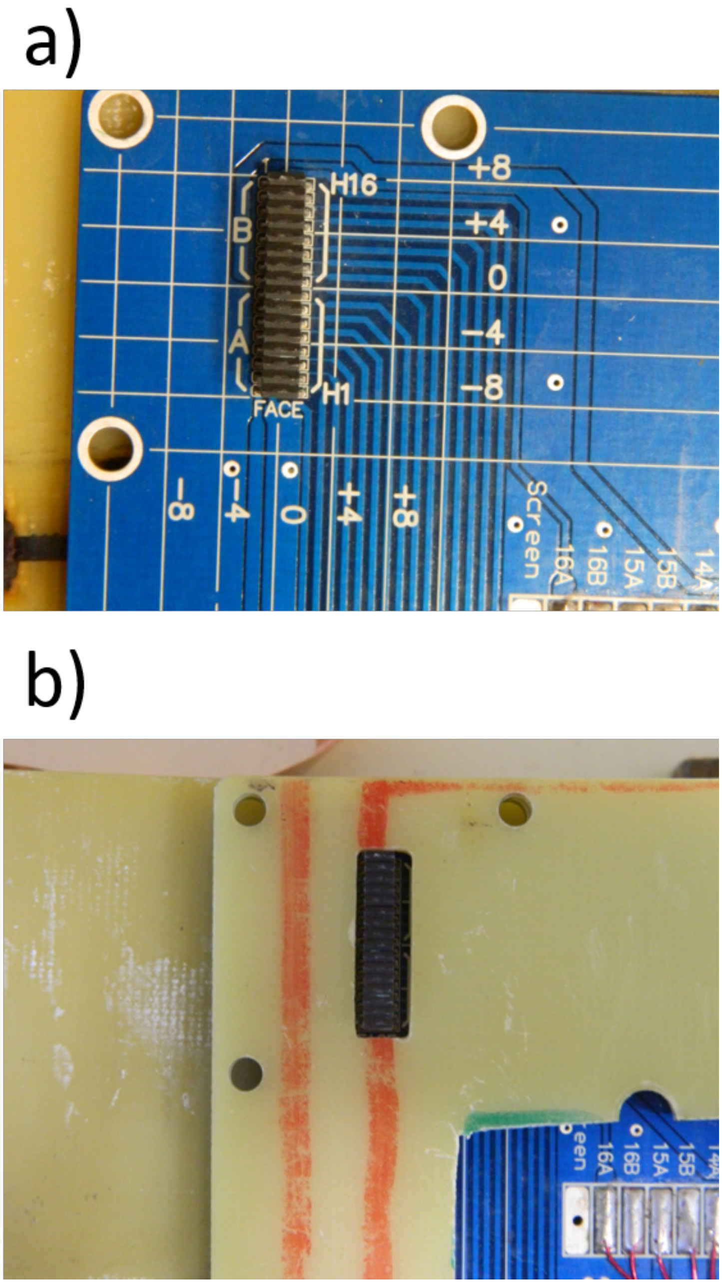

Figure 3.6: (a) shows the P15A Hall Sensor array

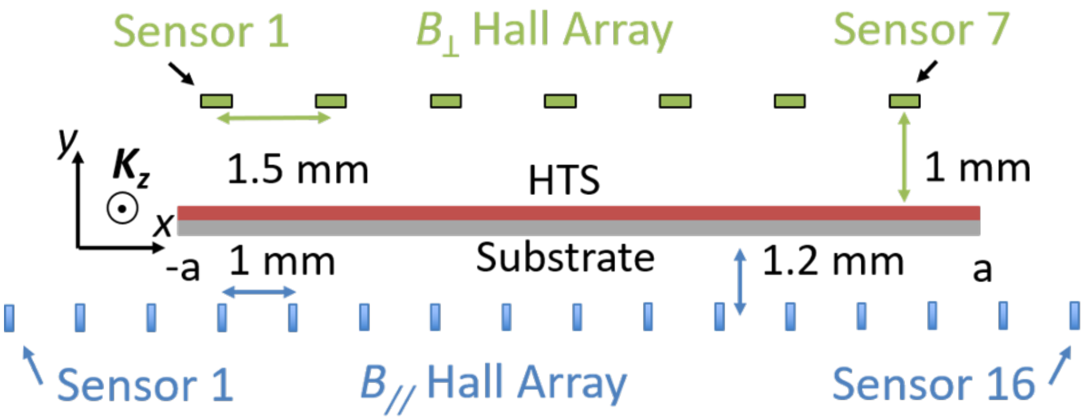

Figure 3.7: Schematic showing the typical position of the Hall sensor arrays relative to a coated conductor.

Another linear array comprised of P15A through-slot sensors from Advanced Hall Sensors [101] were employed. the sensors were aligned to capture the magnetic field component that is parallel to the width of the coated conductor. The array is comprised of 16 sensors mounted on a custom PCB (see figure 3.6 (a) and (b)). Similar to the Arepoc array, the P15A array was calibrated before use, using a Helmholtz coil, with the signal measured using custom made, low noise, instrumentation amplifiers. The sensors have a horizontal spacing of 1 mm and a vertical separation from the HTS conductor of approximately 1 mm.

Figure 3.7 shows the positioning of the two Hall sensor arrays relative to a coated-conductor wire in a typical experiment.

3.2.5 Dynamic Resistance Measurements

Dynamic resistance measurements were performed using 30 cm lengths of individual coated conductor tape mounted on a G10 sample board. This was positioned between a pair of copper-wound racetrack coils capable of producing sinusoidal AC magnetic fields with a peak amplitude up to 100 mT and frequencies of the order of 100 Hz. Two separate voltage measurements were obtained using two pairs of voltage taps 20 cm apart. One pair was helically wound around a cylindrical sheath encapsulating the sample board, whilst the other was a twisted pair running up the centre of the sample. The racetrack coil, HTS tape positioning on the sample board and voltage tap diagrams are shown in figure 3.8. The measurement procedure was as follows. Firstly, the magnet was energised, and a zero-transport current voltage measurement was taken over two seconds. The transport current through the sample was then increased to the reduced current values $i = 0.3$, 0.5, and 0.7, and voltage measurements were taken for each current. The current was then reset to zero and the magnet re-energised to produce a larger AC field. This process was repeated until the desired parameter space had been covered. The voltage

waveform measured at zero transport current for each AC field amplitude is due solely to inductive pick-up from the loop formed by the connecting leads between the sample and instruments. This provided a calibration baseline which was then subtracted from subsequent measurements performed at each non-zero current, in order to yield a signal solely due to the interaction of the AC field with the transport current flowing through the coated conductor tape. The measured voltage signal passed through an NF Electronics 5325 Isolation Amplifier before being measured by an NI DAQ USB-6210 module, recording at a sampling rate of 50 kHz. The collected waveforms were also digitally processed to produce an averaged single cycle waveform for comparison to the model results. The DC resistance was obtained through time-averaging the voltage waveform over this full cycle.

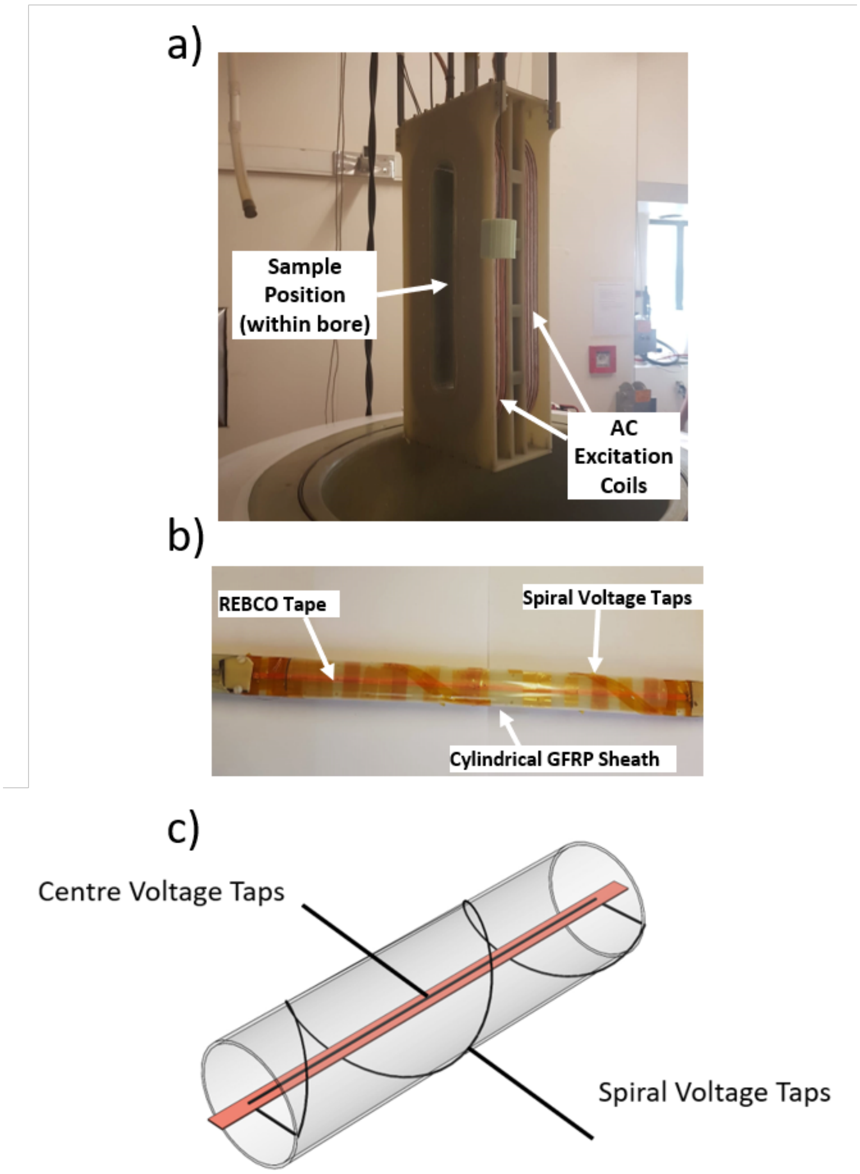

Figure 3.8: a) Photograph of the experimental apparatus used to perform dynamic resistance measurements. b) Photograph of the experimental sample holder in which a REBCO tape is mounted (within the cylindrical sheath). c) Schematic diagram showing the geometry of the sample voltage taps used in the experimental sample holder. Both consist of a twisted pair of copper wires. The centre voltage taps run along all the broad face of the conductor while the spiral pair are wound around a cylindrical sheath surrounding the sample.

4
Critical Currents in Coated Conductors

In the following chapter, we demonstrate that the current saturated state in both virgin and previously magnetized HTS coated conductor wires can be identified by near surface magnetic field measurements. A simple analytical model is presented which requires only that the material has a non-linear $\boldsymbol{E}$-$\boldsymbol{J}$ relationship. The analytical model is validated against FE model results which employ a power-law $\boldsymbol{E}$-$\boldsymbol{J}$ relationship as well as experimental data obtained on a variety of different commercial tapes using both perpendicular and parallel field measurements. Finally, it is demonstrated that the rate at which current is increased has a significant effect on the measured saturation current.

Sections 4.1 to 4.4 have been published in Superconductor Science and Technology in 2021 https://doi.org/10.1088/1361-6668/ac068b. Sections 4.5(concerning perpendicular / parallel field measurements on virgin and previously magnetized samples) and 4.6 (the effect of ramp rate on the saturation current) are additional unpublished material.

The self-field critical current, I_c, of a superconducting wire is determined by the material, geometry, and local flux pinning landscape of the wire [102, 103]. It is a technologically important parameter as it sets a maximum limit on the injected transport current, beyond which damage is likely to occur due to the onset of localised resistive heating. It is also a key input parameter for several widely used analytical equations which are derived from the critical state model (CSM) [35, 40], such as those used to calculate hysteretic AC loss [38, 39, 41, 58, 63]. In the CSM, I_c=AJ_c, where A is the cross-sectional area of the conductor, and J_c is a constant critical current density which results in a Lorentz force equal to the flux pinning force [102]. As described in section 2.3, when a transport current is injected into a superconducting tape starting from the virgin state, the critical state is first established at either edge of the conductor and then fills towards the middle [35, 38–40]. The critical current is reached once the local current density at all points within the conductor is equal to J_c. At this moment supercurrents have 'saturated' the entire conductor volume indicating that it has reached its maximum capacity for current transport. Herein the geometrically saturated critical transport current is referred to as $I_{c,S}$.

The CSM assumes that supercurrents above I_c cannot flow (i.e. the conductor immediately transitions to the normal state). However, practical high-T_c superconductors differ markedly from this ideal behaviour, as they exhibit a gradual onset of flux-flow dissipation over a wide current range prior to the onset of normal conduction [104]. As discussed in section 2.4, transport resistance measurements of HTS tapes do not produce a well-defined threshold value for the transition from the zero-resistance state. Instead, the conventional approach is to define the transport critical current of an HTS tape as the current at which the resistive voltage drop across the conductor is equal to 1 μV cm^{-1} [32, 103, 105]. Here this value is referred to as $I_{c,\mu V}$. The $I_{c,\mu V}$ criterion presents a signal threshold which is readily detectable by experimental voltage measurements, but the arbitrary choice of magnitude is inherently unsatisfying. Furthermore, measurement of any resistive voltage drop necessitates that the superconductor must already be in the dissipative flux-flow regime. This is distinctly different to the 'current-saturated but fully-pinned' definition of I_c that is invoked in the critical state model.

It has been reported that a transition in the evolution of the near-surface perpendicular magnetic field above a coated conductor tape can be observed when ramping the transport current, which appears to correlate with the transition to flux-flow dissipation within the tape [106–108]. The authors of that work have attributed this effect to a novel London-Meissner-type effect occurring at the surface layers of the tape. In this Chapter, it will be shown that it is not necessary to invoke any new physics in order to explain the observed near-surface-field behaviour. In fact, it simply arises from the established model of electrical conductivity in a type II superconductor due to flux pinning/creep/flow [42]. This now provides a much clearer understanding of the origin of the effect, and offers the opportunity to apply this technique to define and measure the $I_{\mathrm{c,S}}$ of practical HTS tapes in the non-dissipative regime. However, this task is complicated by the fact that the onset of this surface-field transition occurs gradually with increasing current. This problem is addressed by presenting a robust criterion which unambiguously defines the self-field 'saturated critical current', $I_{\mathrm{c,S}}$, for any high-aspect ratio tape, via a Hall sensor measurement of the near-surface magnetic field.

4.1 Finite Element Model

The finite element geometry used in this chapter is a 2D model of the rectangular cross-section of an HTS wire in the xy-plane. The governing $\boldsymbol{H}$-formulation equations are given in Section 3.1.1.

Two different function are used for $J_{\mathrm{c},\mu\mathrm{V}}$ and n:

1. A quasi critical state model (QCSM) with constant $J_{\mathrm{c},\mu\mathrm{V}}$ and artificially high n value. In this model,$J_{\mathrm{c},\mu\mathrm{V}} = J_{\mathrm{c0}}$ (the experimentally measured value) with n=100.

2. An interpolated $J_{\mathrm{c},\mu\mathrm{V}}(B,\theta)$ model which uses experimentally measured values for $J_{\mathrm{c},\mu\mathrm{V}}$ and n as outlined in section 3.2.1. Several tapes are considered here, the measured $J_{\mathrm{c},\mu\mathrm{V}}(B,\theta)$ properties for each tape are shown in figure 3.3

Meshing of the FE model consists of 200 elements along the conductor width and 3 elements across the conductor thickness. The elements have a growth ratio of 3 which results in finer meshing at the conductor surface. This is illustrated in Figure 4.1(c). This results in a higher degree of smoothness when compared with uniform meshing, particularly at lower currents. The surrounding air sub-domain is automatically meshed using COMSOL's in built free triangular meshing tool with

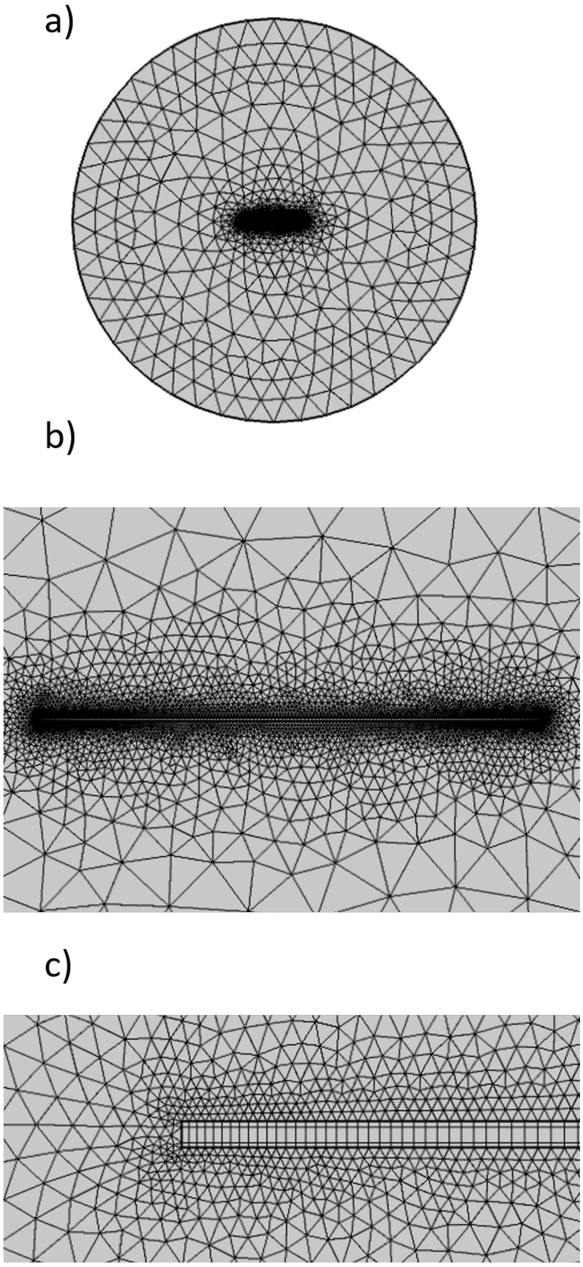

Figure 4.1: (a) Complete view of the FE model geometry with triangular mesh in the air subdomain, (b) Magnified region showing the HTS tape cross-section, (c) Highly magnified region showing the left hand HTS tape edge, illustrating the high mesh density at the tape edges

the boundary sufficiently far away (0.5m) such that the magnetic field produced due to currents in the HTS coated conductor is zero.

Transport current is applied using an integral constraint of the form:

$$I_{\mathrm{t}} = \int_S \mathbf{J} \cdot dS = I_{app}(t) \tag{4.1}$$

where $\mathrm{d}I_{\mathrm{t}}/\mathrm{d}t$ is $10\mathrm{A}s^{-1}$. Only ramping from the virgin state is considered until Section 4.5 where the $I_{\mathrm{app}}(t)$ has the form of a tent function ie $I_{\mathrm{app}}(t)$: 0A $\rightarrow$ 600A $\rightarrow$ 0A $\rightarrow$ 600A.

Because the hall array spacing from the tape is several orders of magnitude further away from the conductor than the conductor thickness, the measured magnetic field profile is indistinguishable to that produced by a 1D distribution of currents. Thus it is reasonable to transform our our 2D model data into 1D data using the equations given in Section 3.1.3

The average electric field over the conductor cross-section is equivalent to the experimentally measured voltage drop in steady electromagnetic fields, and is given by

$$E_{\mathrm{z,ave}} = \frac{L}{2ad} \int_{-a}^{a} \int_{-d/2}^{d/2} \rho J_{\mathrm{z}}(x, y) dy dx \tag{4.2}$$

where L is the separation between the voltage taps along the length of the conductor for a given measurement.

Finally, the perpendicular and parallel components of the magnetic field are examined at a 1mm separation from the broad face of the conductor which approximates to the sensor array position during measurements.

4.2 Identifying the Saturation Current

Before considering the FE and experimental results, it is useful to consider a simple analytical description of the impact of current filling in an HTS tape on the magnetic field signature. Consider a tape comprising a superconducting film of infinitesimal height and width $2a$, and which has a field-independent constant critical sheet current density, K_c . This geometry is shown in Figure 4.2(a).

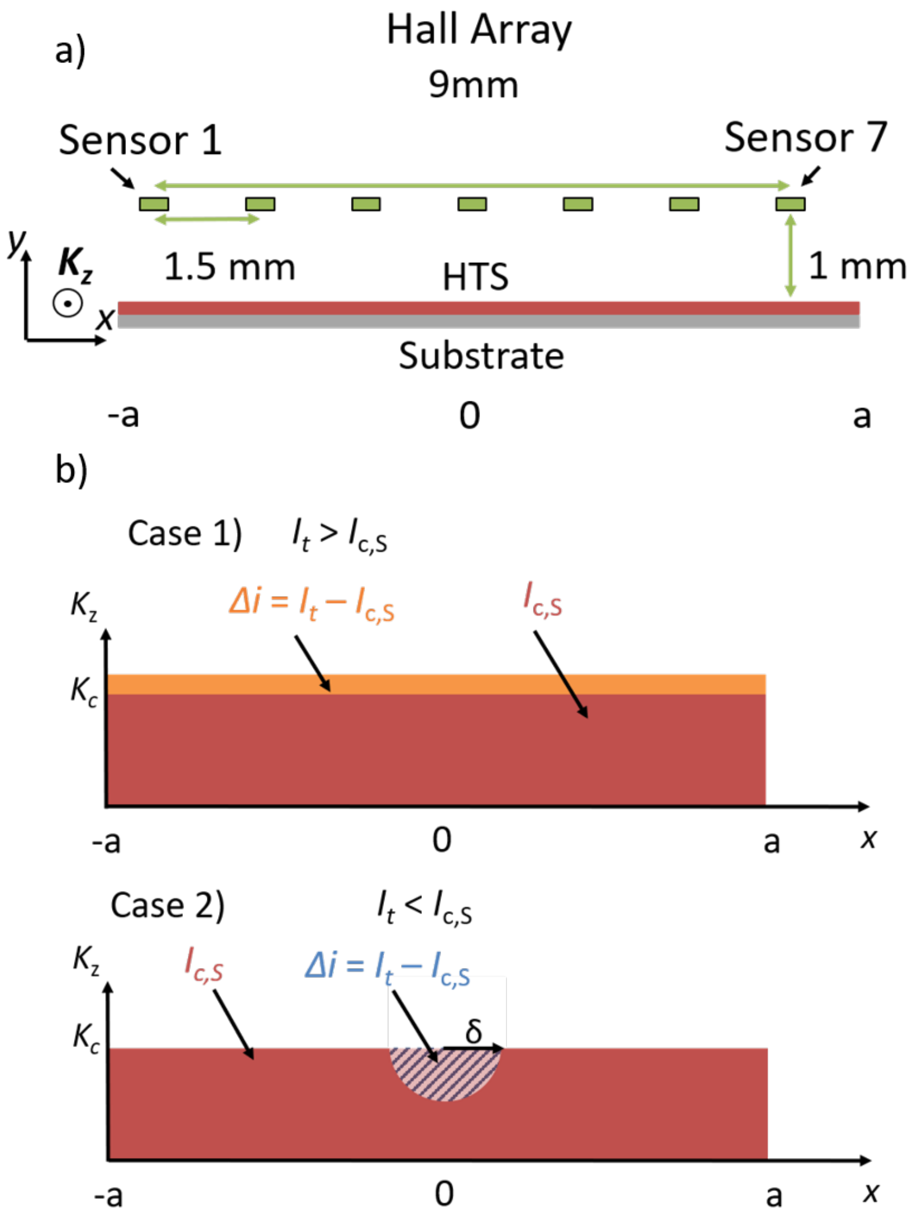

Figure 4.2: (a) Experimental arrangement and orientation of the coated conductor tape and Hall sensors which is also utilised in the FE models. Each individual sensor is numbered 1 to 7 from left to right. (b) Schematic plots depicting the current distributions (during ramping) in a superconducting tape for the two cases: $I_t > I_{c,S}$ and $I_t < I_{c,S}$.

The local sheet current density is $K_z\ (x)$ at each point within the film, such that the total transport current along the tape, is obtained as $I_t{=}\int_{-a}^{a} K_z(x)\mathrm{d}x$.

The perpendicular component of the magnetic field measured within the plane of the conductor is then given by [39, 40, 109]:

$$B_{\perp,x_i}(I_{\rm t}) = \frac{\mu_0}{2\pi}\int_{-a}^{a}\frac{K_z(x_i, I_{\rm t})y_i}{(x_i - x)}dx \tag{4.3}$$

Considering the two cases illustrated in Figure 4.1(b).

Case 1. When $I_t > I_{\rm c,S}$, the magnetic field can be considered a superposition of the contribution from the saturated current distribution at $I_{\rm c,S}$ plus an additional contribution from the excess current $\Delta {\rm i} = I_t - I_{\rm c,S}$, which is uniformly distributed over the entire cross-section of the conductor. This can be expressed as:

$$B_{\perp,x_i}(I_{\rm t}) = \frac{\mu_0}{2\pi}(\int_{-a}^{a}\frac{K_{\rm c,S}(x)}{x_i - x}dx + \int_{-a}^{a}\frac{\Delta i}{2a(x_i - x)}dx) \tag{4.4}$$

Differentiating with respect to I_t and integrating with respect to x, yields:

$$\frac{dB_{\perp,x_i}(I_{\rm t})}{dI_{\rm t}} = \frac{\mu_0}{4\pi a}\ln\left(\frac{|x_i - a|}{|x_i + a|}\right) \tag{4.5}$$

Hence, it can be seen that in this regime, $B_\perp$ is expected to increase linearly with I_t at all points across the tape (i.e. for $x_i < a$).

Case 2. When $0.8I_{\rm c,S} < I_t < I_{\rm c,S}$, the current density at the edges of the tape ($x{=}\pm a$) is $K_{\rm c,S}$ but the current density at centre ($x{=}0$) is $< K_{\rm c,S}$ (See Figure 4.3(b)). This distribution can be considered as the superposition of the saturated current distribution, plus an additional region of negative current Δi occupying a central region of total width 2δ. For $x_i \gg \delta$, integration of Ampere's law for current filaments flowing within the tape yields:

$$B_{\perp,x_i}(I_{\rm t}) = \frac{\mu_0}{2\pi}\int_{-a}^{a}\frac{K_{\rm c,S}(x)}{x_i - x}dx + \frac{\mu_0\Delta i}{2\pi x_i} \tag{4.6}$$

This can be differentiated to obtain:

$$\frac{dB_{\perp,x_i}(I_{\rm t})}{dI_{\rm t}} = \frac{\mu_0}{2\pi x_i} \tag{4.7}$$

Note that $B_{\perp,x_i}$ in this regime is also expected to increase linearly with I_t at all points across the tape (subject to appropriate constraints on position). However, in general

$$\left.\frac{dB_{\perp,x_i}(I_\mathrm{t})}{dI_\mathrm{t}}\right|_{I_\mathrm{t}<I_\mathrm{c,S}} \neq \left.\frac{dB_{\perp,x_i}(I_\mathrm{t})}{dI_\mathrm{t}}\right|_{I_\mathrm{t}>I_\mathrm{c,S}} \tag{4.8}$$

(except for two locations, one near to each edge of the coated conductor). The transition between these two expressions occurs when δ=0, and corresponds to the point when I_t=$I_\mathrm{c,S}$. As the transition between two linear regimes must occur through a point of maximum curvature,one can thus define the saturated critical current $I_\mathrm{c,S}$ as:

$$I_\mathrm{c,S} = \mathrm{argmax}(-\mathrm{sgn}\left(B_{\perp,x_i}(I_\mathrm{t})\right)\frac{d^2B_{\perp,x_i}(I_\mathrm{t})}{dI_\mathrm{t}^2}, \text{ for } 0 < |x_i| \ll a \tag{4.9}$$

Conceptual understanding of this criterion can be gained by considering that $d^2B_{\perp,x_i}/\mathrm{d}I_\mathrm{t}^2$ represents the 'acceleration' of $B_{\perp,x_i}$ with increasing I_t. The transition between 2 regions of constant 'speed', $(\mathrm{d}B_{\perp,x_i}\ (I_\mathrm{t})/\mathrm{d}I_\mathrm{t})$, (see equations 4.5 and 4.7) can then be defined as occurring at the intervening point of maximum acceleration. A similar 'maximum curvature' criterion is widely used to determine the Curie temperature of ferromagnetic materials from magnetisation measurements [110, 111] (where in the case derivatives of magnetisation with temperature are instead used). The following sections present results from FE modelling and experiment which validate this choice of criterion for $I_\mathrm{c,S}$, and demonstrate its utility with a variety of commercially supplied HTS tape aspect ratios and pinning landscapes.

4.3 Finite Element Results

In the following section, FE model results for the computed perpendicular magnetic field are examined, and correlated with the current filling behaviour in a virgin HTS conductor.

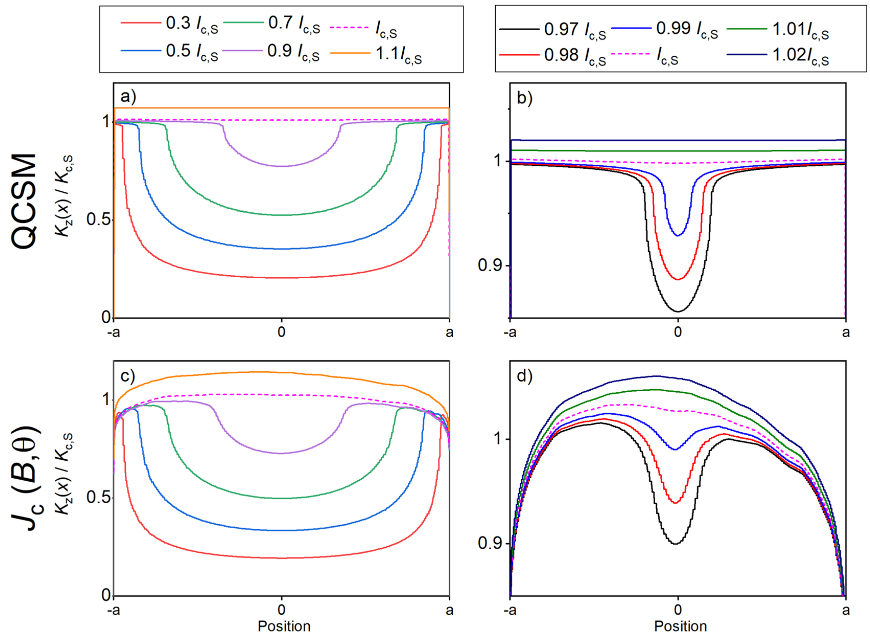

Figure 4.3: Calculated profiles for the sheet current density, $K_z(x)$, across the tape for transport currents ranging from zero to within a few percent of the saturated current, $I_{c,S}$. Data is shown normalised to $K_{c,S}$ (for the $J_{c,\mu V}$ (B,θ) model $K_{c,S}$ is the average sheet current density at $I_{c,S}$) which denotes the average value of K_z across the whole tape at I_t=$I_{c,S}$. Plots (a,b) shows the profile obtained from the QCSM model. Plots (c,d) show the profile obtained from the $J_{c,\mu V}$ (B,θ) model for the 12mm Superpower tape

4.3.1 Current Filling Near $I_{c,S}$

Plots of the current distribution across an HTS tape are shown for the low and high current regimes, calculated from both the QCSM (Figure 4.3 a and b) and $J_{c,\mu V}$ (B,θ) model (Figure 4.3 c and d).The results from the QCSM model are clearly consistent with the regimes described in Figure 4.2 and in section 4.2. For all values of I_t shown, current flows across the entire tape width, with $K_z(x)$ having saturated to a constant value ($K_{c,S}$) at both edges of the tape. For currents less than $I_{c,S}$, there is a small region at the centre of the tape in which $K_z(x) < K_{c,S}$. This region decreases in size as I_t increases until it disappears at $I_{c,S}$, at which point the current distribution across the entire tape saturates to a constant value (pink dashed line). Any additional current is then distributed uniformly over the tape cross-section, so that the current distribution remains uniform across the width.

The $J_{c,\mu V}$ (B,θ) model exhibits suppression of K_c at the tape edges due to the penetrated perpendicular field component. This manifests as a domed shape in K_z when $I_t \geq I_{c,S}$. This dome is not symmetrically aligned with the centre of the tape, which is a result of the non-symmetric $J_{c,\mu V}$ (B,θ) properties measured for the superpower wire [76]. Nonetheless, below $I_{c,S}$ the current density is at its minimum at the centre of the tape, which is consistent with the concept of a superposition of a central region of negative current with the current distribution obtained at $I_t = I_{c,S}$.

Figure 4.4 shows the evolution with increasing transport current of the local values for K_z, $B_\perp$, $\mathrm{d}^2B_\perp/\mathrm{d}I_t^2$ and $E_{z,ave}$ for both J_c models. Figures 4.4(a) and (b) show the same data set as presented in Figure 4.3, but now plotted versus current (for each position). It is clear that K_z shows similar behaviour for both the QCSM and $J_{c,\mu V}$ (B,θ) models. K_z first saturates at the edges, where it then remains approximately constant until current fills to the centre of the tape (i.e. K_z $(x = 0)$ $= K_{c,S}$). Beyond this point K_z(x) increases linearly for all x. A minor difference observed between the QCSM and $J_{c,\mu V}$ (B,θ) models is that the former saturates to the same $K_{c,S}$ value for all x, but the $J_{c,\mu V}$ (B,θ) model exhibits an x-dependent $K_{c,S}$ due to the variation in internal field across the tape width. Plots (c) and (d) show the values for $B_\perp$ at discrete points across the tape (calculated at a displacement of y = 1 mm above the tape). Both above and below $I_{c,S}$, all of the sensors located within $|x| \geq 0.9a$ show regions of constant $\mathrm{d}B_\perp/\mathrm{d}I_t$, with the gradient below $I_{c,S}$ being steeper. This is consistent with the expectations from equations 4.5, 4.7, and 4.8. Plots (e) and (f) show that positive peaks in $\mathrm{d}^2B_\perp/\mathrm{d}I_t^2$ are observed for all sensor positions. Whilst the magnitude of each peak varies, the peak position is independent of sensor location. It can also be seen for both the QCSM and the $J_{c,\mu V}$ (B,θ) models, that the positive peak in $\mathrm{d}^2B_\perp/\mathrm{d}I_t^2$ is strongly aligned with transitions to the upper linear region in both K_z and $B_\perp$.Once again, this is consistent with the superposition of a negative central current region on the saturated current density obtained at $I_{c,S}$ (as discussed in Section 4.2).

4.4 Experimental Results - $B_\perp$ from the Virgin State

This section describes experimental data obtained using the $B_\perp$ Hall Array (section 3.2.4), as well as I-V characteristics obtained using the DC measurement routine outlined in 3.2.2. It is important to note that the current was monotonically stepped and allowed to settle for 20 milliseconds before the voltage measurement is made.

Figure 4.5 shows experimentally measured data for the 12 mm SuperPower tape. This closely resembles the FE model data shown in Figure 4.4(c)-(f) (noting that the ± asymmetry observed in 4.5(a) arises because the centre of the sensor array is not perfectly aligned with the centre of the tape). A family of curves is obtained for $\mathrm{d}^2B_\perp/\mathrm{d}I_\mathrm{t}^2$ with a consistent peak location which is independent of sensor location. For the data presented in figure 4.5, the mean value across the 6 peaks yields $I_\mathrm{c,S}$ = 419 A with a maximum variation (given by sensor 3) of 6 A (=1.4% of $I_\mathrm{c,S}$). It can also be seen that the largest amplitude signal in $\mathrm{d}^2B_\perp/\mathrm{d}I_\mathrm{t}^2$ is given not by the sensor closest to the electrical centre (sensor 3), but by those located midway between the centre and edge of the tape (sensors 2 and 5). This is also consistent with the FE model data in Figure 4.4. Most importantly the $I_\mathrm{c,S}$ value obtained from equation 4.9 is substantially lower (by ~15%) than the conventionally-defined transport critical current $I_{\mathrm{c},\mu\mathrm{V}}$, and occurs at

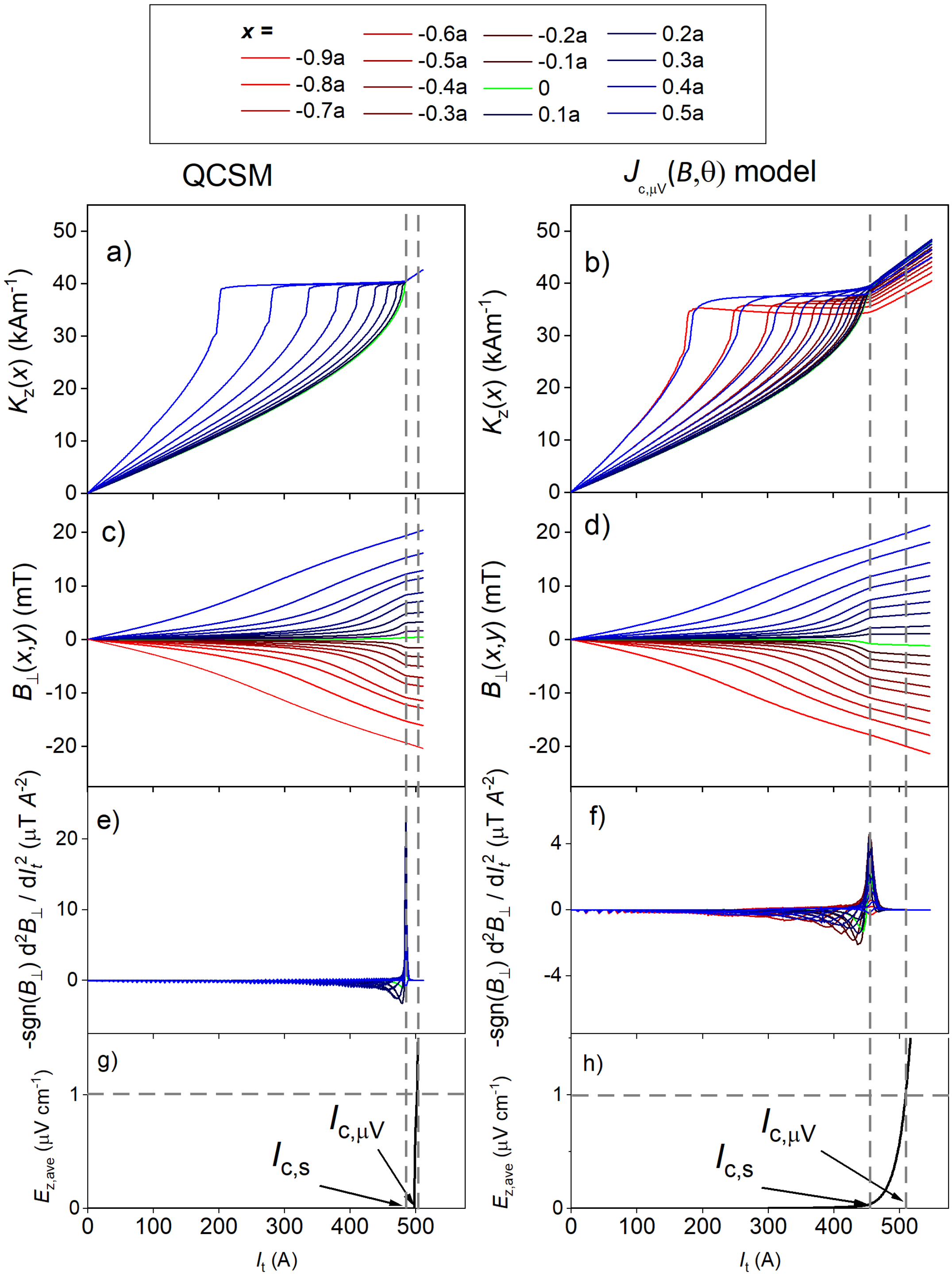

Figure 4.4: Data calculated from the FE model. The interpolated $J_{c,\mu V}$ (B,θ) model uses J_c data measured from a short sample of the same SuperPower 12 mm tape used in the experiment shown in section 4.4. Plots (a) and (b) show K_z as a function of I for several x locations in the tape. Plots (c) and (d) show simulated $B_\perp$ at the indicated x locations and at height $y = 1$ mm approximating the sensor location. Plots (e) and (f) show the calculated values of $\mathrm{d}^2\ B_\perp/\mathrm{d}I_t^2$. Plots (g) and (h) show the calculated E-I curves.

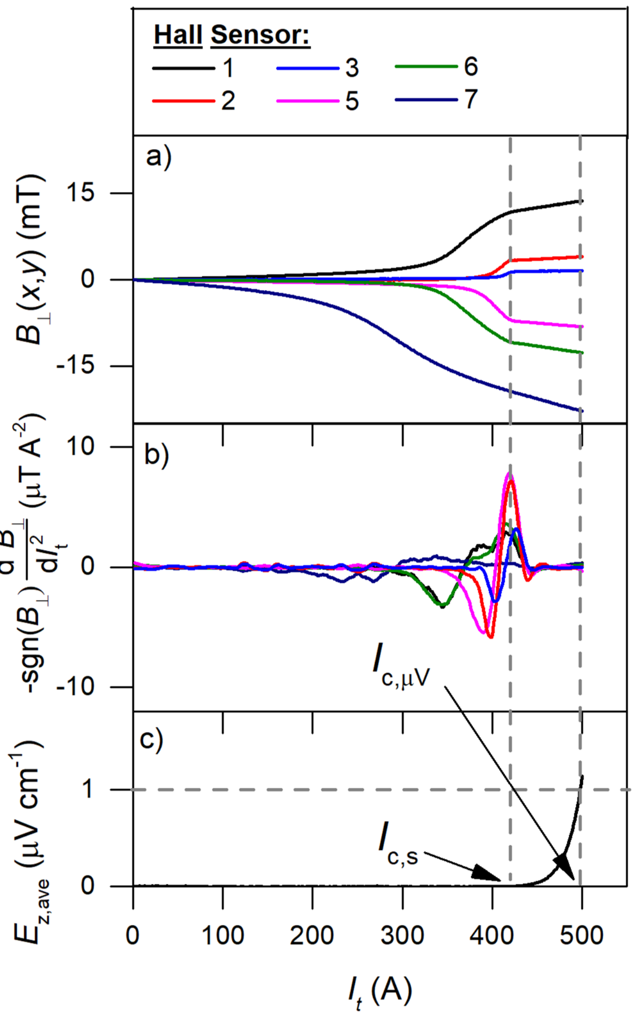

Figure 4.5: Experimental data obtained from the SuperPower 12 mm tape. (a) shows the measured $B_{\perp}$ at each sensor position across the tape width. (b) shows $\mathrm{d}^2\, B_{\perp}/\mathrm{d}I_{\mathrm{t}}^2$ (which is the numerical differential of the data presented in (a) and has been smoothed using Savitzky-Golay filtering with a 15-point window). (c) shows the measured E-I curve for taps placed along the length of the tape.

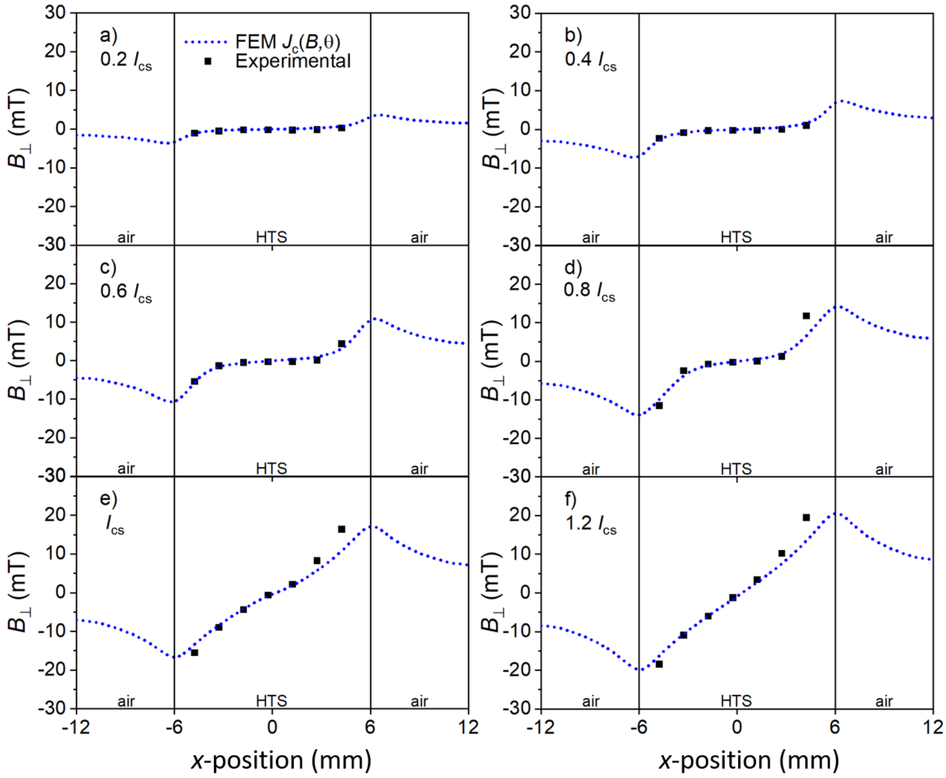

Figure 4.6: Plots showing the perpendicular magnetic field (for y= 1mm) at various x-positions across the Superpower 12mm coated conductor tape. Both experimental and FEM data is shown, showing close agreement. I_t = 0.2 $I_{c,S}$ or 82A in a), 0.4 $I_{c,S}$ or 164A in b), 0.6 $I_{c,S}$ or 246A in c), 0.8 $I_{c,S}$ or 328A in d), $I_{c,S}$ or 410A in e), and 1.2 $I_{c,S}$ or 492A in f).

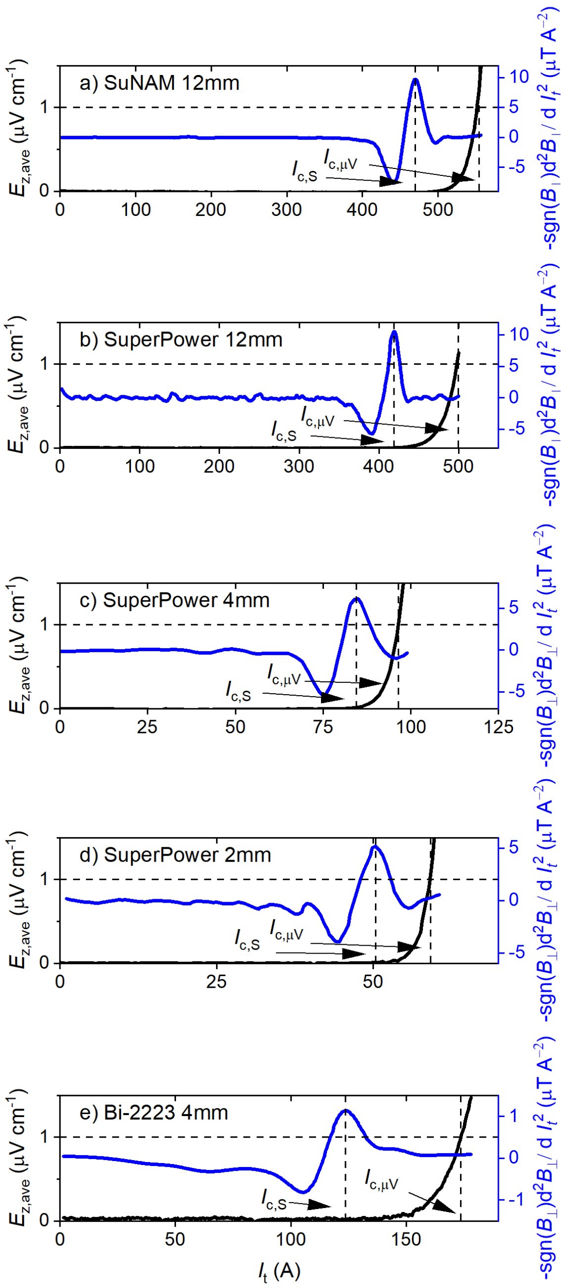

Figure 4.7: Examples of the measured $\mathrm{d}^2B_\perp/\mathrm{d}I_t^2$ obtained from a single Hall sensor placed upon each sample. Data has been smoothed using Savitzky-Golay filtering (15-point window), and is plotted alongside the corresponding *E*-*I* curve obtained from a simultaneous voltage measurement. Plots (a)-(d) show measurements of REBCO coated conductor tapes for various tape widths and suppliers. Plot (e) shows measurement of a 4mm Bi-2223 tape.

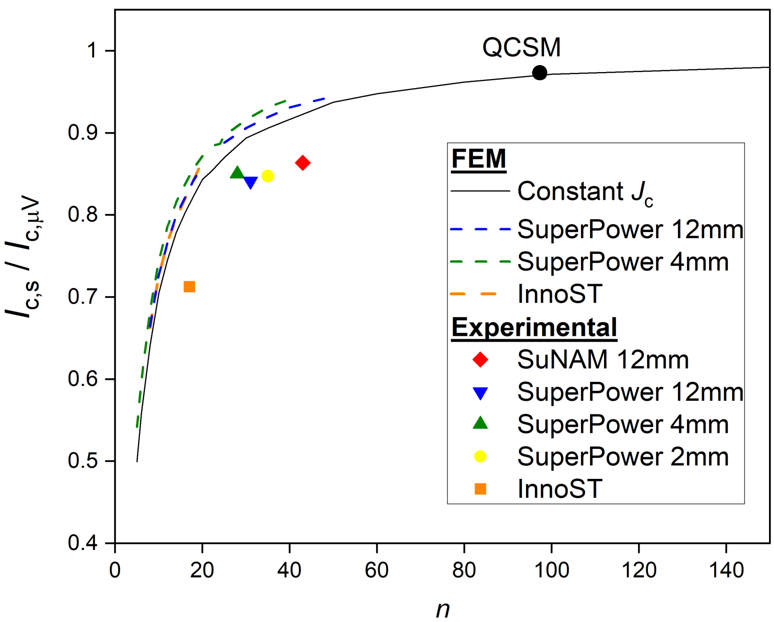

Figure 4.8: A summary of the experimental and FEM data obtained for $I_{c,S}$ and $I_{c,\mu V}$. for the various tapes studied here. Experimental data is plotted as points, FE model data plotted as lines. FE data includes both the constant J_c and QCSM model, as well as $J_{c,\mu V}$ (B,θ) models for the REBCO tapes (SuperPower 4 mm, 12 mm), and Bi-223 tape (InnoST).

a measured electric field that is several orders of magnitude smaller than 1 μV cm^{-1}.

Further validation of the FE model results can be obtained by comparing the measured field profile across the tape width at specific transport currents. These results are shown in Figure 4.6. It is clear that the calculated FE data closely follows the experimental results at all values, both above and below $I_{c,S}$. The slight discrepancy observed on the right hand side of the tape at the highest current levels is most likely due to material inhomogeneity over the sample width. This could be consistent with edge damage caused as a result of the slitting process. Overall the comparison with experiment provides a high level of confidence that the FE model contains all of the physics necessary to describe the evolution of the near surface field across this entire current range. Notably, this differs from the view given in [106, 107], which proposed entirely new physics based on a London-Meissner effect for thin-film type-II superconductors. This London-Meissner effect is not described by the FE model presented, which is instead based solely on a power-law conductivity model which describes conventional type-II behaviour due to flux creep/flow within the superconductor.

Figure 4.7 shows examples of the $\mathrm{d}^2B_{\perp}/\mathrm{d}I_{\mathrm{t}}^2$ signal measured from a variety of different sample tapes, using just a single Hall sensor placed approximately midway between the centre and edge of the tape. In all cases, a clearly discernible peak $\mathrm{d}^2B_{\perp}/\mathrm{d}I_{\mathrm{t}}^2$ is apparent, and this is plotted alongside the corresponding measured *E*-*I* curve obtained using voltage taps. As expected, for all samples $I_{\mathrm{c,S}}$ is consistently lower than $I_{\mathrm{c},\mu\mathrm{V}}$. The Bi-2223 sample shows the smallest ratio of $I_{\mathrm{c,S}}$ / $I_{\mathrm{c},\mu\mathrm{V}}$, due to its lower n-value (n= 18) which corresponds to a slower onset of dissipative flux-flow above $I_{\mathrm{c,S}}$.

Figure 4.8 summarises the ratio $I_{\mathrm{c,S}}/I_{\mathrm{c},\mu\mathrm{V}}$ obtained for the various tapes studied in this work. It can be noted immediately that the ratio of $I_{\mathrm{c,S}}$ to $I_{\mathrm{c},\mu\mathrm{V}}$ is generally insensitive to the tape's underlying microstructure and $J_{\mathrm{c},\mu\mathrm{V}}$(B,$\theta$) properties, as all of the interpolated the FE models show similar behaviour - namely that the ratio is divergent at low n-values, and tends towards unity as n tends to infinity. This is because a power-law resistivity with a larger n-value more closely approximates the critical-state model (as this corresponds to a sharper flux-flow transition between 'zero-resistance' and the resistive state). As a result, at large n the onset of a measurable dissipative voltage more closely approximates to the current saturation threshold. However, for real tapes, n-values in the range $15 < n < 40$ are typical [43], and in this range, the saturated critical current $I_{\mathrm{c,S}}$ is consistently found to be 15-30% lower than $I_{\mathrm{c},\mu\mathrm{V}}$.

4.5 Perpendicular vs Parallel Field Measurements

The previous section has shown that $I_{c,S}$ can be clearly identified from analysis of the perpendicular field component during ramping from the virgin state. In the following section, a comparison between the efficacy of measurements of $B_{\perp}$ or $B_{//}$ to identify $I_{c,S}$ is given. This section presents a combination of FE data from the SuNAM interpolated $J_{c,\mu V}$ (B,θ) model as well as experimental data collected from the SuNAM tape using both the $B_{\perp}$ and $B_{//}$ Hall sensor arrays. The experimental procedure for current stepping and voltage measurements is given in Section 3.2.2

4.5.1 $B_{\perp}$ Measurements over Repeated Cycles

Figure 4.9 shows the evolution of the $B_{\perp}$ for both virgin and hysteretic cycles of the SuNAM wire. The left-hand column shows calculated values from the interpolated $J_{c,\mu V}$(B,θ) FE model. Experimental data is shown in the right-hand column. The hall array is positioned with sensor 4 very near to the conductor centre, as indicated by the particularly low measured field at this position and the FE data is calculated at approximate x-locations corresponding to the $B_{\perp}$ Array.

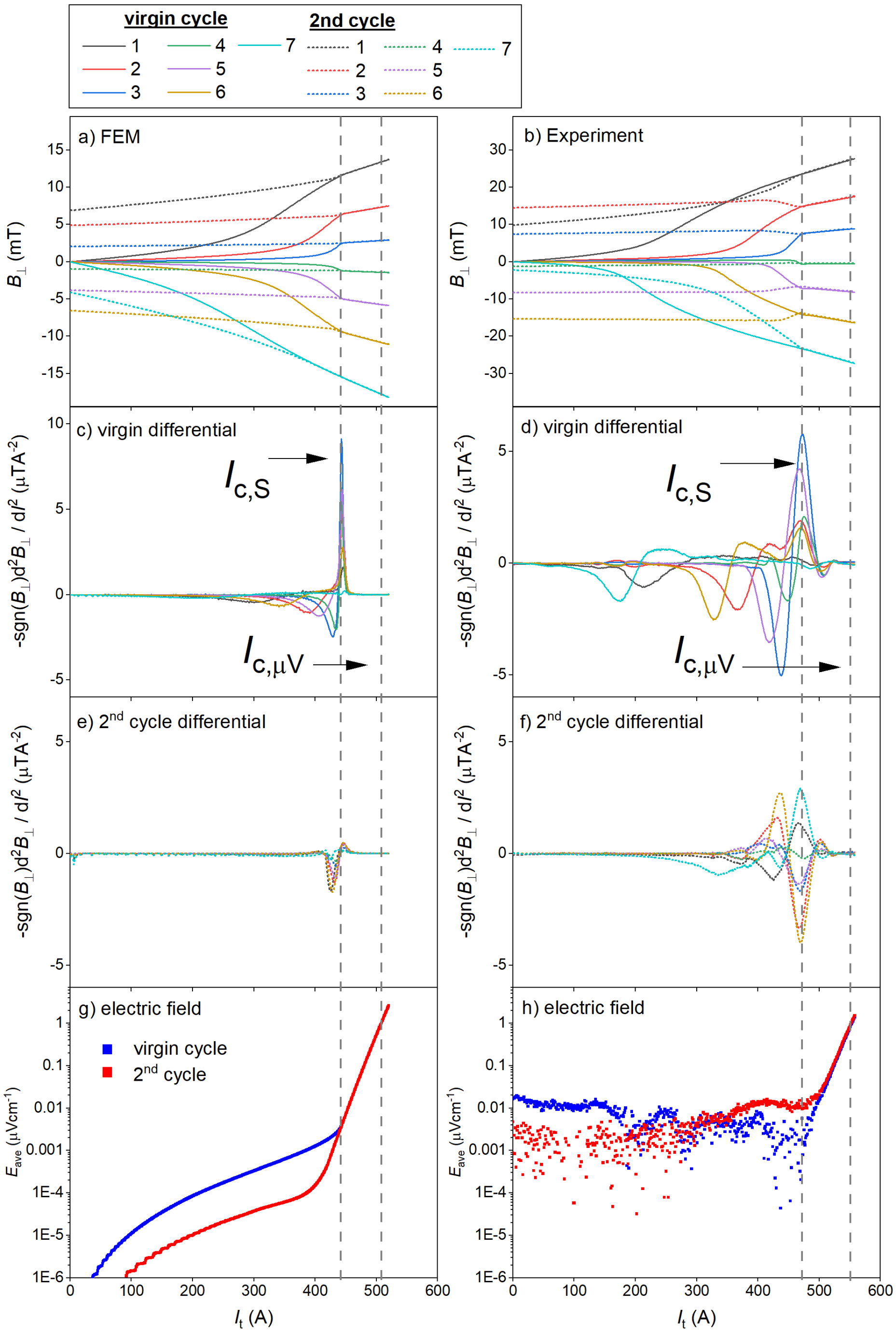

Figure 4.9: Plots show results from the interpolated $J_{c,\mu V}(B,\theta)$ model (left column) and, experimentally measured (right column) data. Plots a) and b) show $B_\perp$ during current ramping from the virgin state (solid) and during the 2nd cycle (dot). Plots c) and d) show $d^2B_\perp/dI_t^2$ during the virgin ramp, e) and f) show $d^2B_\perp/dI_t^2$ during the 2nd cycle and g) and h) show the calculated / measured electric fields during the virgin and second cycles. The experimental data is smoothed using a Savitsky-Golay filter with a 15-point window. The legend indicates the sensor number across the Hall Array.

The virgin field data behaves as expected from section 4.3 and 4.4. The second order differential signal produces a family of peaks with a well defined $I_{\mathrm{c,S}}$ value. In the second cycle each Hall sensor acquires a DC offset due to remnant magnetization currents from the previous ramp cycle[35, 44]. These field offsets reduce the change in magnitude of $B_{\perp}$ over the second ramp, thus resulting in a smaller peak in the differential signal. The electric field at low current is also significantly lower during the second ramp as the rearrangement of existing remnant currents results in a lower net change in flux across the conductor width. The virgin and hysteretic field profiles come together at $I_{\mathrm{c,S}}$. It is also immediately clear from both the FE and experimental data that equation 4.9 is no longer valid for identifying $I_{\mathrm{c,S}}$. In the FE data, there are precursory peaks which are larger in amplitude than the final peaks, which correspond to the erasure of screening currents from the previous cycle. More puzzling perhaps in the experimental data, is the reversal of the polarity from of the differential signal obtained from all but the outermost sensors. However, this presents no limitation as it is the final peak in $\mathrm{d}^2B_{\perp}/\mathrm{d}I_{\mathrm{t}}^2$ before tending to zero which captures the current saturation across the conductor width. Most importantly, the collection of experimentally measured peaks in both the virgin and subsequent cycle present at the same value of I_{t}.

4.5.2 $B_{//}$ Measurements over Repeated Cycles

Figure 4.10 shows the evolution of $B_{//}$ in the same manner as the previous figure. The $B_{//}$ Hall array used in this work has finer resolution across the width compared to the $B_{\perp}$ array and as such, data is presented from every second sensor to avoid clutter. For $B_{//}$, the largest field amplitude is generated above the centre of the tape, corresponding to sensor 8. The finite element locations plotted are chosen to approximate the experimental arrangement assuming that sensor 8 lies directly above the tape centre. Many of the same general features observed here are common to the perpendicular field component. During the virgin ramp, all sensors increase from zero and undergo a transition from non-linear to linear at a single value of I_t. In the following cycle, each sensor measures a position-dependent DC offset due to the presence of remnant magnetization currents which again suppress the non-linearity at low I_t, and hence the $d^2B_{//}/dI_t^2$ signal is significantly diminished when compared with the virgin case. In both the FE and experimental data, the parallel magnetic field lies on top of the virgin field data after reaching saturation. For $B_{//}$ measurements, the field polarity varies depending on which face of the conductor the Hall array is located and equation 4.9 is therefore no longer valid. However, as was noted in the case of $B_\perp$, one can identify $I_{c,S}$ from the final collection of peaks before tending to zero. Importantly, measurements of $B_{//}$ in both the virgin and hysteretic conditions yield the same value for $I_{c,S}$ as determined from $B_\perp$ measurements.

4.6 Effect of Ramp Rate on $I_{c,S}$

In the following section, the dependence of $I_{c,S}$ on the rate of change of current, dI_t/dt is considered. Data is presented from both the $J_{c,\mu V}$(B,θ) FE model, as well as experimental data obtained from the corresponding coated conductor. The details for the experimental procedure are given in section 3.2.3.

4.6.1 FE modelling of $I_{c,S}$ at Different Ramp Rates

It has been previously reported that the measured *I*-*V* characteristics of HTS tapes are sensitive to the rate at which current is injected into the material [112–115] in both thin film and cylindrical wire geometries. In that work an analytic model has been presented in which the electric field in the edge regions can be several orders of magnitude larger than at the tape centre. Similarly, fast pulse *I*-*V* measurements made in pulsed magnetic fields > 1T [105] have exhibited non power-law behaviour at measured electric fields $\gg 1\mu$V cm^{-1}.

Figure 4.11 shows the evolution of FE computed values for $B_\perp$, $d^2B_\perp/dI_t^2$, and $E_{z,ave}$ as a function of transport current for several different values of dI_t/dt. In (a) as $\mathrm{d}I_{\mathrm{t}}/\mathrm{d}t$ increases, the non linear region for $B_{\perp}$ persists to higher transport currents before collapsing onto the linear regime. As a result the $I_{\mathrm{c,S}}$ values determined using equation 4.9 vary with ramp rate from 230A at 3 As^{-1} to 303A at 3 kAs^{-1}. This is shown in plot (b). Plot (c) shows the calculated $E_{\mathrm{z,ave}}$ alongside a power-law fit using equation 2.12 to the slowest ramp rate. Not only do the $E_{\mathrm{z,ave}}$ values vary by several orders of magnitude with varying $\mathrm{d}I_{\mathrm{t}}/\mathrm{d}t$, but there is clear deviation from the pure power law behaviour at low currents for all ramp rates. Interestingly, $I_{\mathrm{c,S}}$ denotes the current at which pure-power law behaviour is recovered which occurs only once the conductor is fully saturated. It is also noteworthy that if the current is ramped sufficiently fast, then the 1 μV cm^{-1} criterion can be driven into this alternate regime, highlighting the ambiguity of this electric field criterion for determining I_{c}.

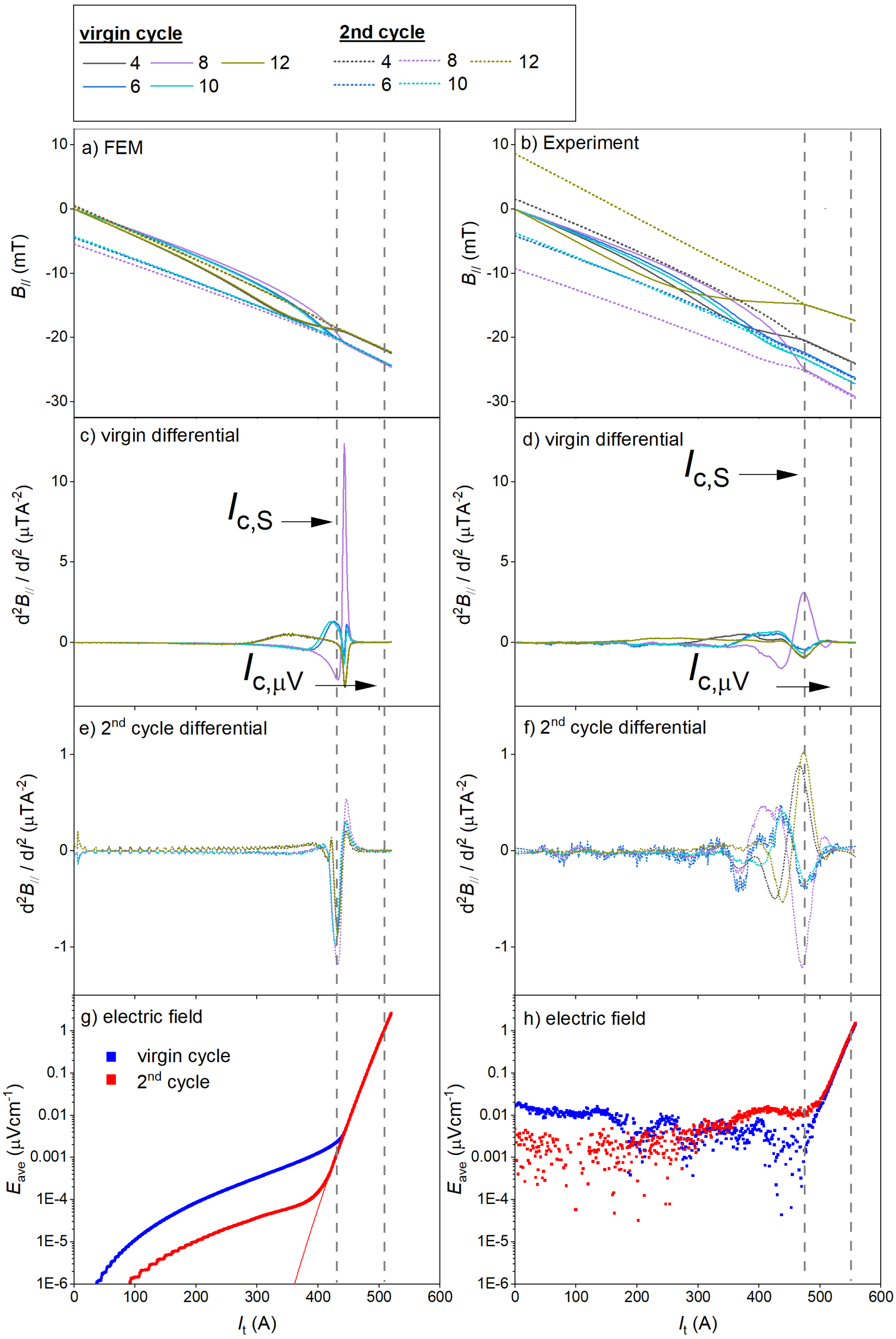

Figure 4.10: Plots showing results from the interpolated $J_{c,\mu V}$(B,θ) model (left column) and, experimentally measured (right column) data. Plots a) and b) show B// during current ramping from the virgin state (solid) and during the 2nd cycle (short dot). Plots c) and d) show $d^2B_\perp/dI_t^2$ during the virgin ramp, e) and f) show $d^2B_\perp/dI_t^2$ during the 2nd cycle and g) and h) show the calculated / measured electric fields during the virgin and second cycles. The experimental data is smoothed using a Savitsky-Golay filter with a 15-point window. The legend indicates the sensor number across the Hall Array.

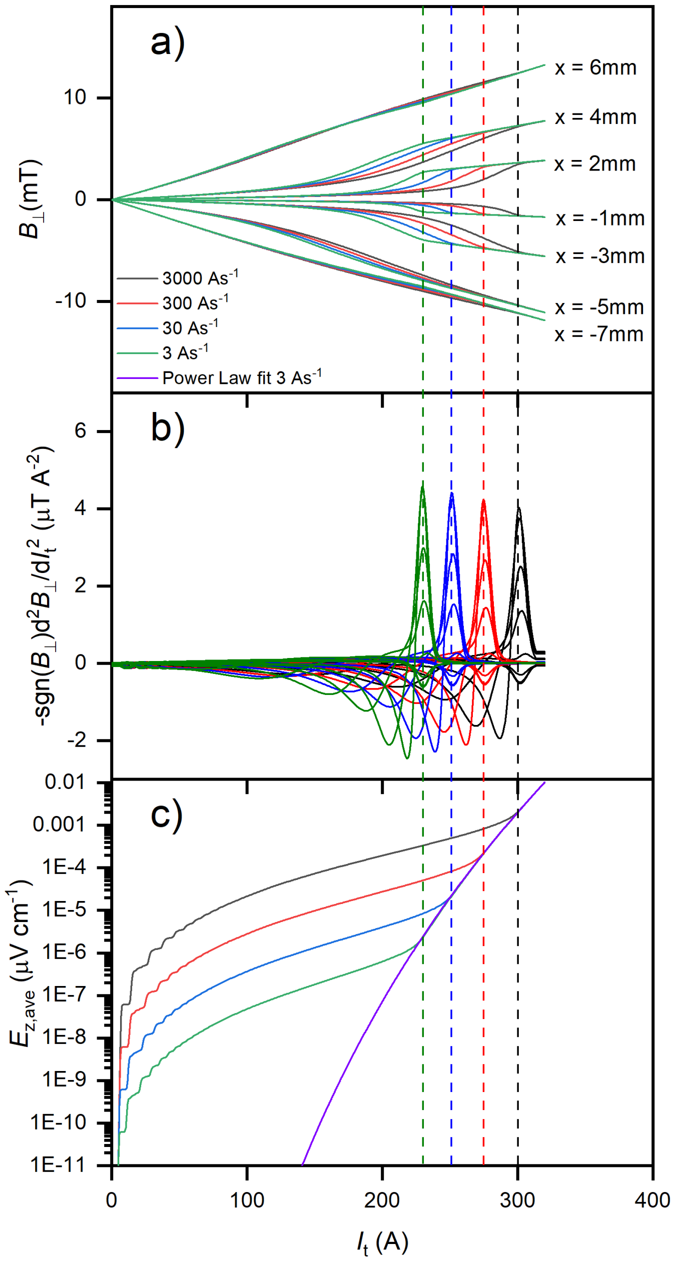

Figure 4.11: Plots showing the interpolated $J_{c,\mu V}(B,\theta)$ model calculated values for (a) $B_\perp$ at the indicated x locations 1mm above the HTS tape, (b) $d^2B_\perp/dI_t^2$ from (a), (c) electric field and ideal power law behaviour. The curves are coloured according to their dI_t/dt value.

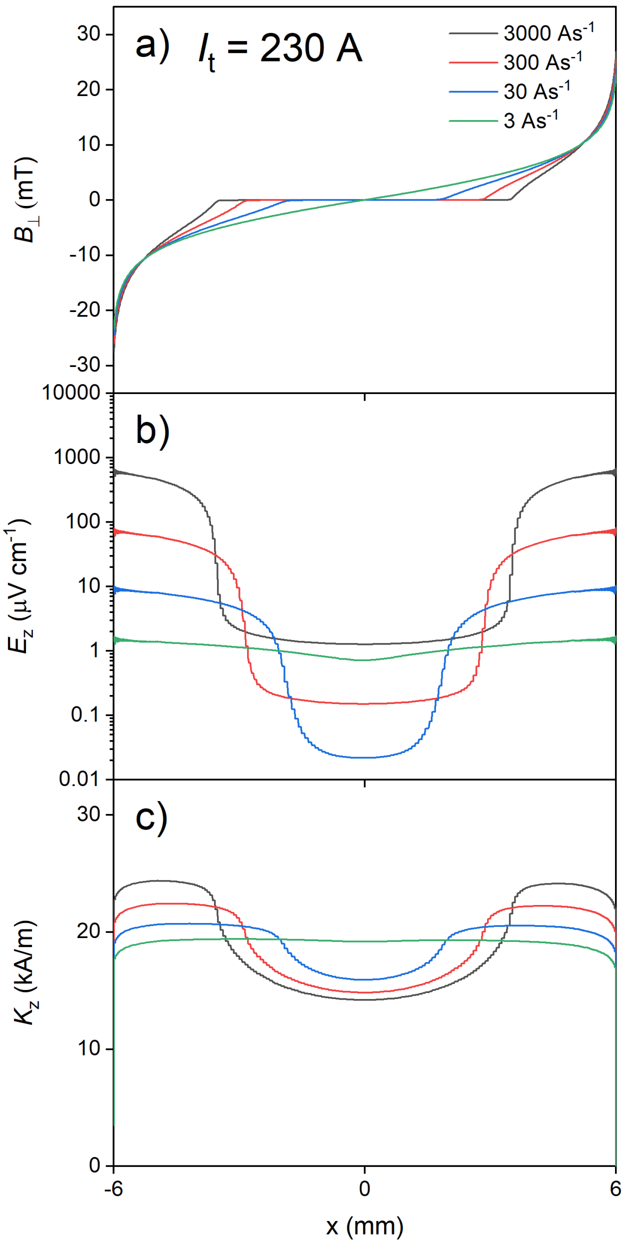

Figure 4.12: Plots showing the interpolated $J_{c,\mu V}(B,\theta)$ model calculated values for (a) $B_\perp$, (b) E_z, and (c) K_z when the total transport current is 230A ie $I_{c,S}$ when $dI_t/dt = 3$ As^{-1} This corresponds to the green dashed line in Figure 4.11.

The variations of both $I_{\mathrm{c,S}}$ and $I_{\mathrm{c},\mu\mathrm{V}}$ with ramp rate can be understood by examining the local$B_{\perp}$, E_{z}, and K_{z} during the ramp. These are presented in Figure 4.12. Data is shown at I_{t} = 230A which corresponds to the green dashed line in Figure 4.11. Figure 4.12 (a) shows the local perpendicular magnetic field. For the slowest ramped case, 230A corresponds to $I_{\mathrm{c,S}}$ and flux has fully penetrated to the centre of the sample. Similarly, the local electric field and sheet current are uniform across the conductor width. As the ramp rate increases, a larger proportion of the conductor centre remains flux-free. Increasing rates of $\mathrm{d}I_{\mathrm{t}}/\mathrm{d}t$ increase the rate of change of flux entry at the tape edges, which in turn generates a larger electric field at the tape edges as can be seen in plot (b). By examining the fastest ramped case of 3000 As^{-1}, it is clear that although $E_{\mathrm{z,ave}}$ is now well above $1\mu\mathrm{V\ cm}^{-1}$, this is generated almost entirely in the edge regions of the conductor. This dominant contribution to $E_{\mathrm{z,ave}}$ does not obey the same power-law behaviour as is observed in the current saturated state. Plot (c) shows the local K_{z}, which is necessarily larger at the tape edges to produce these larger electric fields.

4.6.2 Experimental Measurements at Different Current Ramp Rates

Finally, experimental data is shown for comparison to the Interpolated $J_{\mathrm{c},\mu\mathrm{V}}(\mathrm{B},\theta)$ model in Figure 4.13. In plot (a), measured $B_{\perp}$ data obtained from a single sensor is shown alongside the corresponding $\mathrm{d}^2B_{\perp}/\mathrm{d}I_{\mathrm{t}}^2$ and measured $E_{\mathrm{z,ave}}$ data. The experimental data shows excellent agreement with the FE data in terms of both the predicted $I_{\mathrm{c,S}}$ and $E_{\mathrm{z,ave}}$ values. As $\mathrm{d}I_{\mathrm{t}}/\mathrm{d}t$ increases, so too do the values for $I_{\mathrm{c,S}}$. In all cases, for $I_{\mathrm{t}} < I_{\mathrm{c,S}}$, there is a non power-law electric field regime which increases in magnitude with ramp rate. As indicated by FE analysis, this occurs due to over-currents at the tape which are generated by the rapid flux penetration. For the fastest ramped measurement, the 1 $\mu\mathrm{Vcm}^{-1}$ criterion occurs well below the onset of power law behaviour. However, in all cases, the $\mathrm{d}^2B_{\perp}/\mathrm{d}I_{\mathrm{t}}^2$ signal consistently identifies the saturation current $I_{\mathrm{c,S}}$ which corresponds to the current at which power-law behaviour of the electric field begins to dominate.

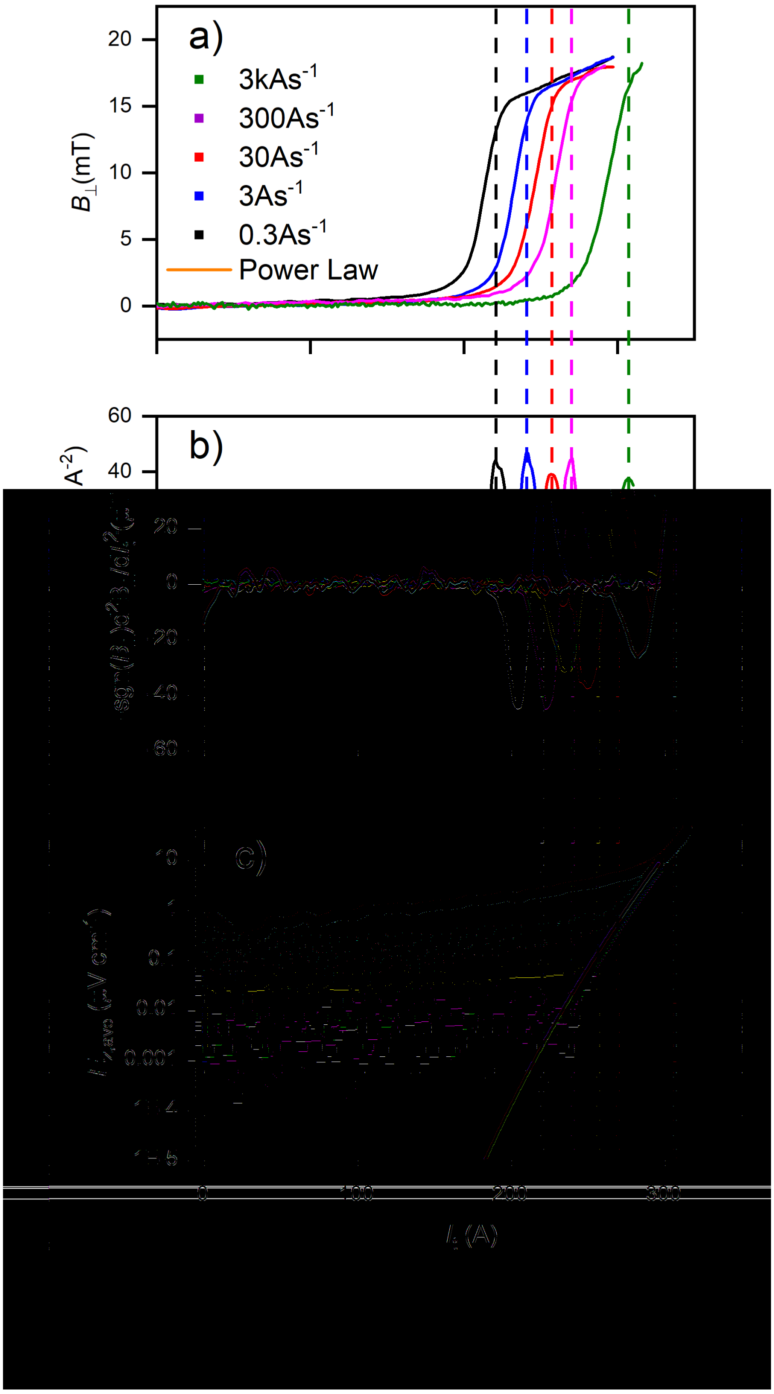

Figure 4.13: Experimental data obtained from the SuperPower Coated conductor with ramp rates varying from 0.3As^{-1} to 3kAs^{-1}. (a) shows the measured $B_{\perp}$, (b) shows the $\mathrm{d}^2B_{\perp}/\mathrm{d}I_{\mathrm{t}}^2$ values obtained from (a), smoothed using Savitsky-Golay filter with a 15 point window and, (c) the measured $E_{\mathrm{z,ave}}$ with a power law fitted to the slowest ramp.

4.7 Summary Discussion

In this chapter, a robust definition which enables the 'saturated critical current' of a superconducting tape to be unambiguously measured via surface perpendicular or parallel field measurements from one or more Hall sensors has been presented. In practice, a single Hall sensor can be used, as long as it is positioned near to the conductor for an appreciable field signal and in a location appropriate for the field component being measured. Geometric saturation of the transport current within a superconducting tape under DC conditions occurs prior to the onset of a measurable dissipative voltage (under DC conditions), and can be observed from the evolution of the perpendicular field profile across the tape width. Geometric saturation over the width is observable under fast-ramping conditions in the same manner as indicated by finite element modelling, although in the low-current regime, a non power-law dissipative voltage is expected due to the presence of over-currents at the conductor periphery.

The utility of this approach using $B_{\perp}$ to measure $I_{\mathrm{c,S}}$ for samples of various commercial HTS tapes of different aspect ratios, down to widths of 2 mm and up to thicknesses of several hundred microns has been demonstrated. As the evolution of $\mathrm{d}^2B/\mathrm{d}I_{\mathrm{t}}^2$ is determined only by the onset of current saturation across the conductor width, it is entirely independent of the superconducting material and $J_{\mathrm{c},\mu\mathrm{V}}(\mathrm{B},\theta)$ properties under consideration. This is demonstrated by the success of this approach for both ReBCO and Bi-2223 tapes. Indeed, the only criteria required to obtain a clearly discernible peak in $\mathrm{d}^2B/\mathrm{d}I_{\mathrm{t}}^2$ are that the tape should have a cross-section aspect ratio » 1, and a non-linear E-J relationship which leads to current-filling from the edge to the centre of this tape. Whilst a power-law resistivity has been adopted in the presented FE modelling, the approach is not restricted to that case and will yield a robust value of $I_{\mathrm{c,S}}$ for superconducting materials with any E-J dependence that delivers a current-filling evolution similar to the critical state model. Although $I_{\mathrm{c,S}}$ and $I_{\mathrm{c},\mu\mathrm{V}}$ are defined to be identical within the critical state model, measurements of real tapes show that $I_{\mathrm{c,S}}$ is typically 15-30% lower than $I_{\mathrm{c},\mu\mathrm{V}}$. It is clear that no constant electric field criterion is appropriate for a complete range of operating conditions. This is a direct consequence of the fact that $I_{c,S}$ always describes the threshold current at which geometric current saturation occurs, but practical superconductors exhibit some dissipative flux-flow resistance for currents well below the 1 μV cm^{-1} criterion. The difference between $I_{c,S}$ and $I_{c,\mu V}$ is largest for superconductors exhibiting a relatively slow onset of flux-flow resistance (i.e. a low n-value).

5 Dynamic Resistance in a Coated Conductor

As discussed in Chapter 2, dynamic resistance is a resistive phenomenon in type-II superconductors that carry a DC transport current while simultaneously being exposed to an alternating magnetic field. This resistance is attributed to interactions between vortices and the transport current, as the aforementioned flux traverses the transport current carrying regions of the conductor [52, 56, 58]. Understanding the origin and behaviour of this dynamic loss is relevant to optimising the management of heat dissipation for various HTS applications. In addition, dynamic resistance has been identified as playing a key role in the operating mechanism of HTS flux pumps [18, 20, 116, 117] and is an attractive candidate for persistent current switching in HTS circuits [83, 118–121].

In this chapter, experimental measurements are presented for the dynamic resistance of different REBCO tapes carrying a DC current and exposed to an oscillating perpendicular field. The exact details of the experimental methodology is outlined in section 3.2.3. Measurements of both the transient voltage waveforms and the time-averaged DC resistances are compared with numerical finite element simulations obtained using the $\boldsymbol{H}$-formulation. There are clear variations between the voltage response from different tapes, which can be understood in terms of their differing $J_\mathrm{c}(B,\theta)$ dependence. This emphasises the importance of employing experimentally measured $J_\mathrm{c}(B,\theta)$ data when simulating transient effects in HTS tapes and wires.

This Chapter has been published in Superconductor Science and Technology in 2019 https://doi.org/10.1088/1361-6668/ab6bfe.

5.1 Finite Element Model

The finite element model geometry considered here is identical to that presented in figure 4.1, consisting of a 2D cross-section of a HTS coated conductor in the xy-plane and assumed to have infinite length along the z-axis. The governing $\boldsymbol{H}$-formulation equations are given in 3.1.1.

Simulations have been performed using two different functions for $J_{\mathrm{c}}(B,\theta)$ and $n(\mathrm{B},\ \theta)$.

1. Constant J_{c} model ($J_{\mathrm{c}} = J_{\mathrm{c0}}$): In this model, the critical current and n-value are both assumed to be constant at all times, and are set equal to the values measured in zero applied field, i.e. $J_{\mathrm{c}}(B,\theta) = J_{\mathrm{c0}}$, $n = 20$. In sections 5.2 and 5.3, a modified version of the constant J_{c} model has also been considered, which uses an artificially high n-value of $n = 200$, as a close approximation to the critical state model.

2. Interpolated $J_{\mathrm{c}}(B,\theta)$ model: This model uses the two sets of experimentally-measured values shown in figure 3.3 corresponding to the two ReBCO tapes (SuperPower and SuNAM) on which dynamic resistance measurements were performed. Self-field effects are removed from the experimental measurements by the method described in [122], to provide a set of self-field corrected $J_{\mathrm{c}}(B,\theta)$ values. These describe the local critical current density at each point within the tape, as a function of the total local magnetic field. Both the J_{c} and n-values are then input into the numerical model using a two variable interpolation function, as described in [123, 124].

Meshing of the FE model consists of 200 elements along the width of the superconducting domain (in the x-direction), and 3 elements across its thickness (in the y-direction). This ensures that the computational time required for the models remains practical, while retaining enough resolution at the surface of the superconductor when simulating the current distribution. In the surrounding sub-domain, a free triangular mesh is used. The sub-domain boundary is sufficiently far away such that the normal component of the magnetic field due to the superconductor is zero. In the non-superconducting sub-domain, a linear Ohm's law is solved with the resistivity set to 1 Ωm. The computational model assumes that all losses occur entirely in the HTS layer, a reasonable assumption for low AC frequencies (e.g. < 1 kHz) where the eddy-current losses in the metallic layers are negligible [125, 126]. The HTS layer is also assumed to remain at a constant temperature. Thus, only contributions from the superconducting layer are included when calculating the dynamic resistance, and no temperature dependence is included.

The current and field distributions within the tape are computed using a two stage process. First, a DC transport current is applied to the superconductor, ramped from zero to the required value. Following this, a sinusoidal perpendicular magnetic field is then applied to the sample for two and a half AC field oscillations. Subsequent data analysis neglects the initial half cycle during which the superconducting strip is magnetised from its virgin state. This ensures that the computed values are periodic with the applied magnetic field. A DC transport current, I_t is applied via an integral constraint applied to the superconducting cross-section S of the form

$$I_{\mathrm{t}} = \int_S J \cdot dS = I_{\mathrm{app}}(t) \tag{5.1}$$

In the first stage of the computation, $I_{\mathrm{app}}(t)$ is a linear ramp function with a gradient of 10 A/s. This ramp function is run until the DC transport current is equal to the self-field critical current I_{c0}. Once completed, solutions are available at all stored time intervals and reduced currents. The second stage of the computation is then initiated using the solution which corresponds to the specified reduced current under study (i.e. $i = I_{\mathrm{t}}/I_{\mathrm{c}} = 0.3$, 0.5 and 0.7). A sinusoidal perpendicular AC magnetic field of the form $B_{\mathrm{app}}(t) = B_{\mathrm{a0}}\sin(\omega t)$ is applied using COMSOL's magnetic field boundary condition.

The dynamic resistance, R_{dyn}, results in the development of a voltage drop, ΔV, along the z-direction of the coated conductor. This is calculated from the 2D FE model using

$$\Delta V = L \cdot \frac{\partial V(t)}{\partial z} \tag{5.2}$$

where L is the length of the conductor in the z-direction.

Dynamic resistance is a low-frequency quasi-static phenomenon, such that the voltage drop is simply the difference in electrostatic potential across the conductor. In the Coulomb gauge (defined by $\boldsymbol{\nabla} \cdot \boldsymbol{A} = 0$, such that $\boldsymbol{\nabla}^2 \boldsymbol{A} = \mu_0 J$), the electrostatic potential is equivalent to the electric scalar potential, such that [127, 128]

$$\nabla V(t) = \mathbf{E}(t) + \frac{\partial \mathbf{A}(t)}{\partial z} \tag{5.3}$$

Note that taking the divergence of both sides of equation 5.3 yields the familiar definition of the electrostatic potential, $\boldsymbol{\nabla}^2 V = \boldsymbol{\nabla} \cdot \boldsymbol{E} = \rho/\varepsilon$. The magnetic vector potential, A, is calculated from the inverse curl of B, and by specifying a Dirichlet boundary condition that A_{z} is equal to $B_y x$ along the boundary of the surrounding air sub-domain. The 2D FE geometry constrains currents from flowing in the plane of the model, such that $J_x = J_y = E_x = E_y = A_x = A_y = 0$. As a result, equation 5.3 simplifies solely to the z components, with $\partial V/\partial z$ constant throughout the model plane for each moment in time. However, it should be noted that both $E_z(x, y, t)$ and $A_z(x, y, t)$ are functions of x and y, and hence do vary across the plane (see, for example, figure 5.3(c)). To minimise numerical error, the spatially-averaged value of ΔV(t) across the HTS cross-section is used, calculated using equation 5.4:

$$\nabla V(t) = L\frac{\partial V(t)}{\partial z} = \frac{-1}{S}\int_S (E_z + \partial_t A_z) \cdot dS \tag{5.4}$$

The time-averaged DC dynamic resistance, in units of $\mu\Omega$/m/cycle, is then calculated by integrating ΔV over a single cycle of the applied field and dividing by the transport current

$$R_{dyn} = \frac{1}{I_{\mathrm{t}}} \int^{1/f} \nabla V \mathrm{d}t \tag{5.5}$$

It is noteworthy that all dissipation within the superconductor is fully described by the E–J power-law and, as a result, the A-vector contribution can in fact be omitted from equations 5.4 and 5.5 without loss of accuracy [81].

5.2 Coated Conductor Samples

Two different samples of REBCO tape were investigated in this study: SuperPower SCS4050-AP and SuNAM HCN04200 with specifications given in [21, 22]. Measurements of the $J_{\mathrm{c}}(B,\theta)$ and $n(B,\theta)$ parameters for each tape were made using the method outlined in chapter 3 [32, 43]. Experimental measurements were made at 77 K on short length samples (~5–7 cm), in applied magnetic fields up to 500 mT and obtained for a full 360° range of field orientations at 5° increments. The measured values for these two particular samples are shown in figure 3.3, which illustrates the different dependencies of critical current upon applied magnetic field for each tape. Both tapes were 4 mm wide with the superconducting layer being either 1.3 μm or 1 μm thick, for the SuNAM and SuperPower tapes respectively. The SuNAM tape had a self-field I_{c0} of 205.5 A and its $J_c(B,\theta)$ behaviour is symmetric about $]\theta = 180°$, and periodic such that $I_c(B,\theta) \approx I_c(B,\theta + 180°)$. In contrast, the SuperPower tape had an I_{c0} value of 105.6 A and the measured critical current did not exhibit a symmetry plane with respect to the angle of the applied field.

5.3 DC Dynamic Resistance

Figure 5.1 shows the experimentally measured DC dynamic resistance, R_{dyn}, per cycle obtained at a frequency of 118.66 Hz for three different values of i for both tapes, and using the two different sets of experimental voltage taps ('spiral' and 'centre'). The R_{dyn} values are plotted as a function of the applied field amplitude B_{a0}. Also plotted are the analytical solutions obtained from equation (2.13) using either equations (2.15) or (2.16) to define the threshold field. Consistent with results reported in [61, 70, 129], there is very close agreement between these equations and experimental results. For comparison, figure 5.1 also shows the calculated values of R_{dyn} obtained from the numerical model.

The interpolated $J_{\mathrm{c}}(B,\theta)$ model is observed to deliver good agreement with experiment, although it does appear to slightly underestimate B_{th} in every case. However, the constant J_{c}, $n = 20$ model diverges substantially from experiment, and significantly understates the magnitude of $\mathrm{d}R_{dyn}$ / $\mathrm{d}B_{a0}$ at fields above B_{th}. This highlights the importance of including the full $J_{\mathrm{c}}(B,\theta)$ dependence within the FE model. It also raises the question as to why the analytical equations (2.13),(2.15) and (2.16) are so successful, despite employing a constant critical current value. On this point, it is instructive to note that the analytical approaches assume $n \to \infty$, whilst the constant J_{c} FE model uses the realistic finite value of $n = 20$. By contrast, if the FE model is instead run using a much higher n-value of $n = 200$, results are obtained which closely agree with equations (2.15) and (2.16). This suggests that the artificially high n-value within the critical state model can compensate for the error introduced by assuming a constant J_{c}. This appears to be a 'happy accident' that holds for the samples and experimental conditions considered here, but it is not clear how applicable these equations would be in other differing situations such as dynamic resistance measurements performed in DC background fields or more complicated geometries (ie cables comprising multiple tapes where shielding effects can be expected to play a significant role) [67, 68, 71, 72].

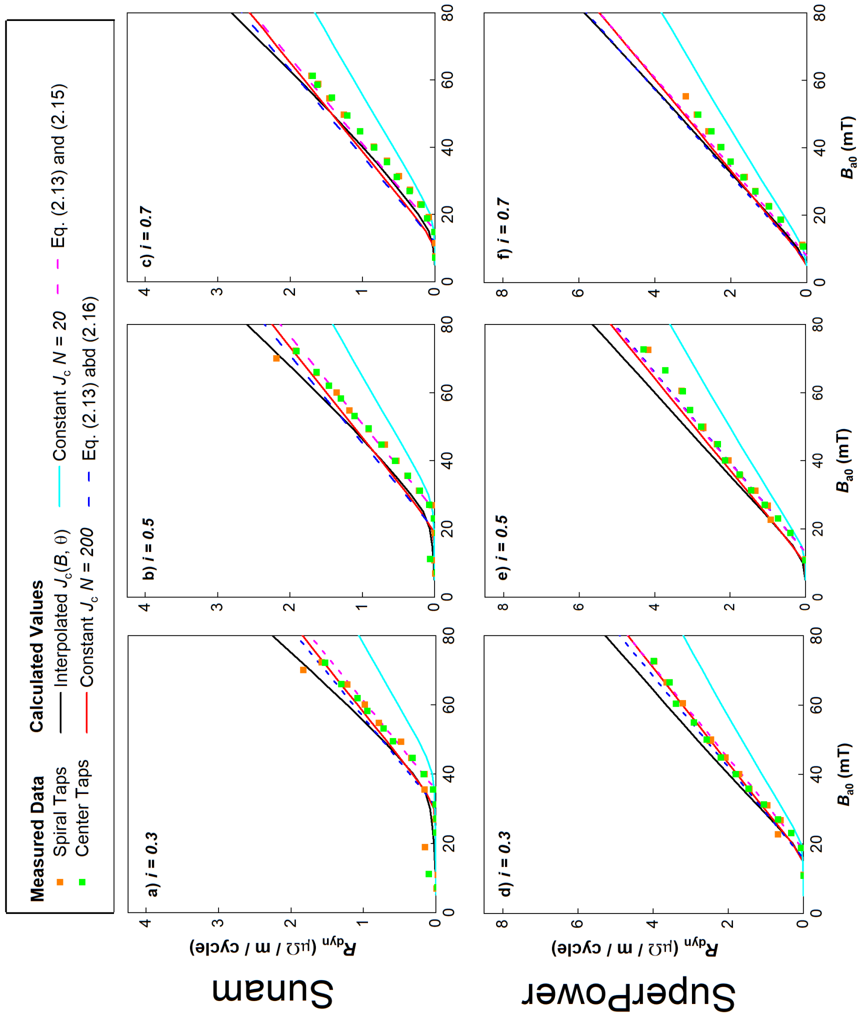

Figure 5.1: The dynamic resistance per cycle as a function of B_{a0}, for SuNAM (a)–(c) and SuperPower (d)–(f) tapes. The Data is shown for $i = 0.3$, 0.5 and 0.7 at a frequency, $f = 118.66$ Hz. Experimental data from both the spiral and centre voltage taps is shown, alongside values calculated from equations (2.13),(2.15), and (2.16). The numerically-modelled data is also shown for models run using various different functions to describe $J_c(B,\theta)$, namely: constant $J_c(n = 20)$, constant $J_c(n = 200)$ and interpolated $J_c(B,\theta)$.

5.4 Voltage Response to an AC Perpendicular Field

In addition to DC experimental measurements, transient time-resolved measurements were also performed to obtain the resistive voltage waveform across each sample tape. Figure 5.2 shows these experimentally-measured voltage waveforms, and compares these with the corresponding waveforms obtained from the numerical simulations using each of the $J_c(B,\theta)$ models. Each plot shows the response over two cycles of the applied field at 118.66 Hz for $i = 0.5$.

As expected [32, 56, 73], the numerical models all predict a voltage waveform that is periodic over one half cycle of the applied magnetic field (i.e., its fundamental frequency is twice that of the applied field). This is because applied flux interacts with the transport current whenever the magnitude of the applied field exceeds the shielding capacity of the tape. This occurs during each half cycle, irrespective of the polarity of the applied field. There is a noticeable difference in both the amplitude and shape of the waveforms calculated using the constant J_c model with $n = 200$ (approximating the critical state model), versus $n = 20$ (which is close to the actual measured value of n in self-field). In particular, the lower n-value exhibits both a smaller peak amplitude and a smaller peak width. This is the reason that it delivers a lower time-averaged DC resistance (shown in figure 5.1).

As with the constant J_c models, the experimental waveform data shows a doubling of the fundamental frequency of the voltage waveform compared to the applied field. However, striking differences are also apparent. Most notably, as the magnetic field amplitude increases well above B_{th}, a peak-splitting effect is observed whereby a non-zero minimum appears within each waveform at $B_{app}(t) \sim 0$. The only numerical model which reproduces this feature is the interpolated $J_c(B,\theta)$ model [32]. Understanding the origin of this 'peak-splitting' effect requires detailed scrutiny of the current and field distributions, and is explored in the following section.

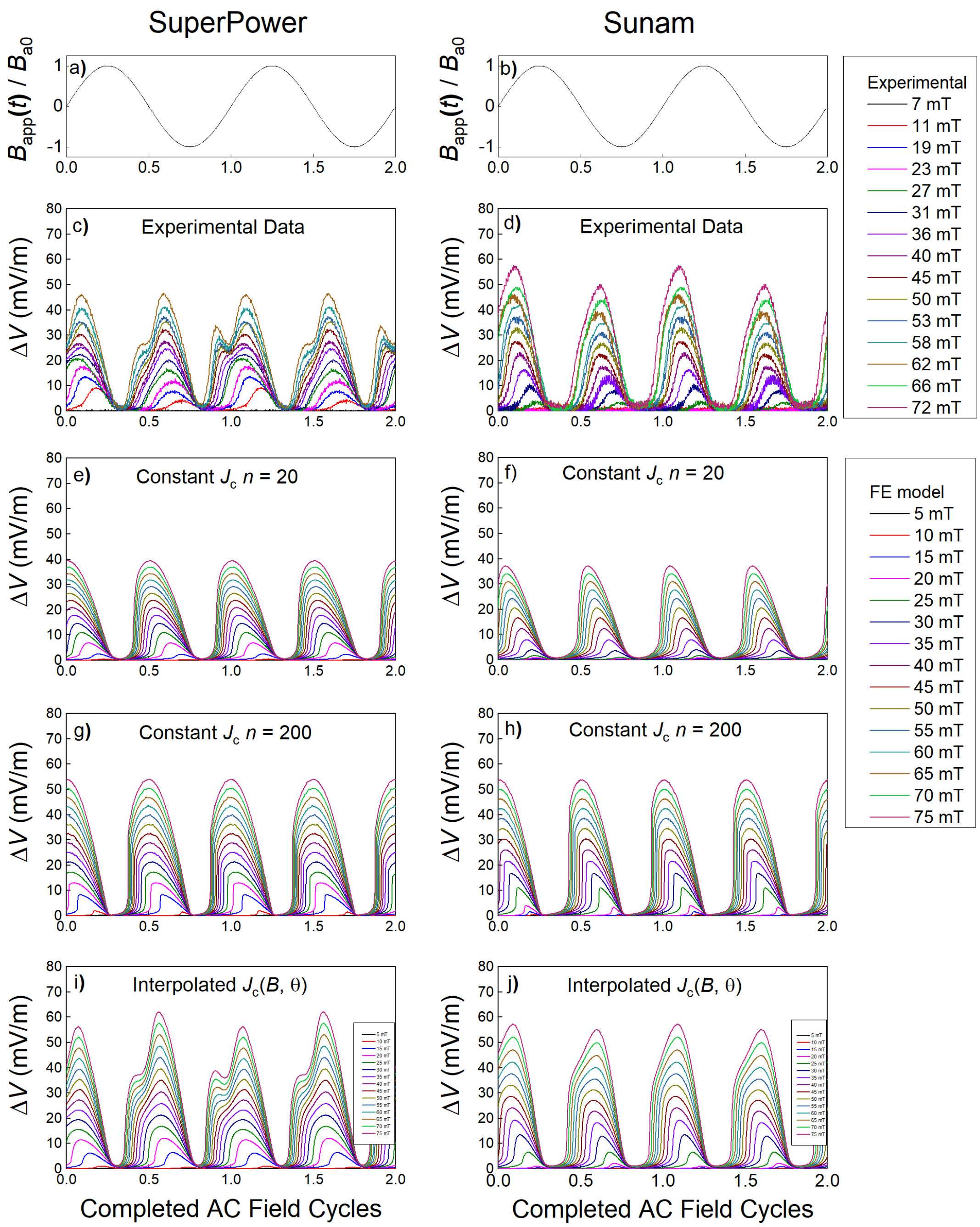

Figure 5.2: Experimental measurements of the instantaneous voltage, $\Delta V(t)$, across each REBCO tape sample, compared with numerically-modelled values obtained from the constant J_c and interpolated $J_c(B, \theta)$ models. The SuperPower and SuNAM data are shown in the left and right columns respectively. All plots are for $i = 0.5$ and $f =$ 118.66 Hz. Plots (a) and (b) show the applied field; (c) and (d) show the experimental waveforms; (e) and (f) show the constant J_c (n = 20) models; (g) and (h) show the constant J_c ($n = 200$) models; and (i) and (j) show the interpolated $J_c(B,\theta)$ waveforms.

In addition, the interpolated $J_c(B,\theta)$ model for the SuperPower tape also shows a small asymmetry in the amplitude of the voltage peaks observed during the positive and negative half-cycles of applied field. This is due to the asymmetric angular dependence of $J_c(B,\theta)$ for these tapes.

5.5 Cyclic Evolution of Sheet Currents and Electromagnetic Fields

In the following, the transient response of each FE model is investigated using contour plots, which show the temporal evolution of the local sheet current density K_z, critical current density $K_c(B)$, electric field E'_z, and magnetic field B'_y as explained in section 3.1.3.

5.5.1 Constant J_{c0} Model

Using figure 5.3, it is possible to examine the evolution of K_z, B'_y, and E'_z in the constant J_c model for the SuperPower tape at $i = 0.5$ and $B_{a0} = 100$ mT. Note that figure 5.4 shows these quantities using more conventional line plots at the moments in time indicated by the dashed horizontal lines in figure 5.3. Plot 5.3(a) shows that magnetisation screening currents occur at the edges of the film, but are only distinguishable on the side where the screening currents run anti-parallel to the DC transport current. These screening currents penetrate to an approximately constant depth in each half-cycle. This conforms with the conventional critical state model for dynamic resistance [56, 58], where the transport current is considered to occupy a constant width region at the centre of the tape. Once $\mathrm{d}B_{\mathrm{app}}/\mathrm{d}t$ changes sign (at $\omega t = (2m{+}1)\pi/2$ where m = integer), the existing screening current distribution begins to be erased by opposite polarity screening currents which enter from each side. The complete erasure of the previous anti-parallel component of the screening current on one side of the film occurs shortly after $\omega t \approx 2\pi/3$, and coincides with an increase from zero of ΔV in plot (d).

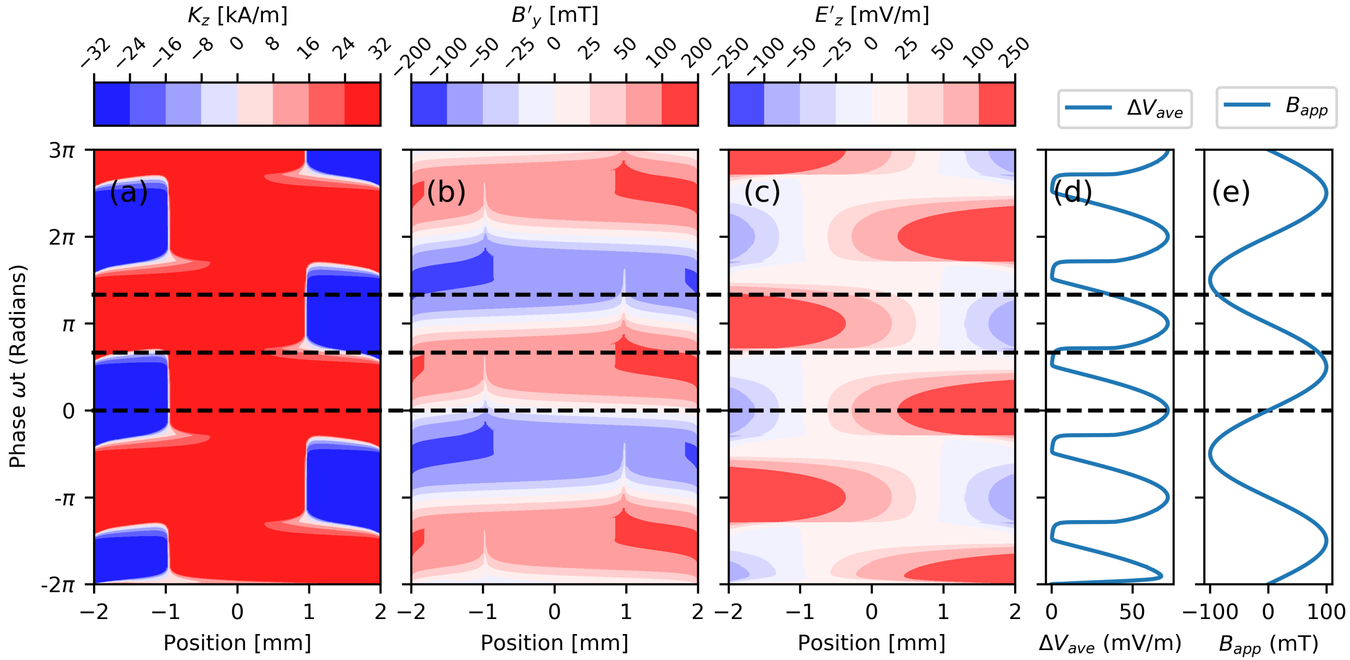

Figure 5.3: Plots (a),(b),(c) are contour plots of the time dependence of the sheet variables K_z, B'_y, and E'_z across the width of the conductor, alongside ΔV (d) and $B_{\mathrm{app}}(t)$ (e). All are shown for two and a half cycles of the applied field. Data is for the SuperPower constant J_c $n = 200$ model with $i = 0.5$, $f = 118.66$ Hz and $B_{a0} = 100$ mT.

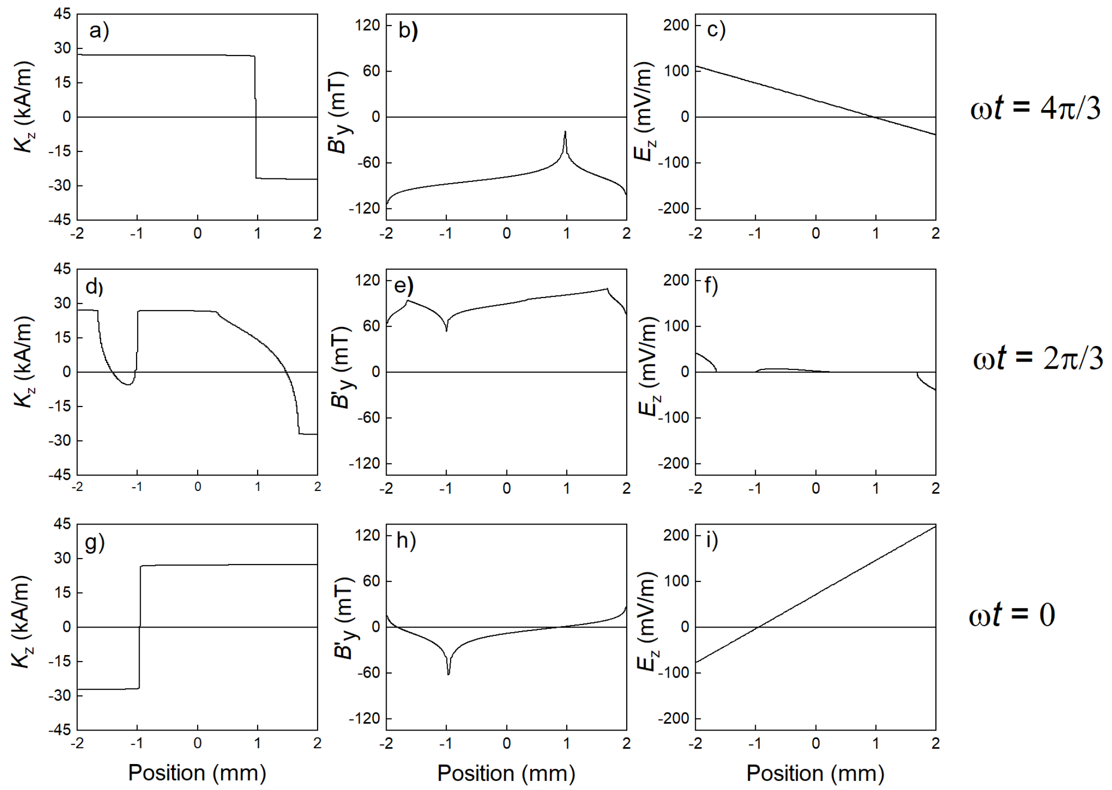

Figure 5.4: Shown are the instantaneous profiles across the conductor width for K_z (plots (a,d,g)), B'_y (plots (b,e,h)) and E'_z (plots (c,f,i)) for the SuperPower constant J_c $n = 200$ model at the three moments-in-time indicated by the dashed lines $\omega t = 0$, $2\pi/3$ and $4\pi/3$ in figure 5.3.

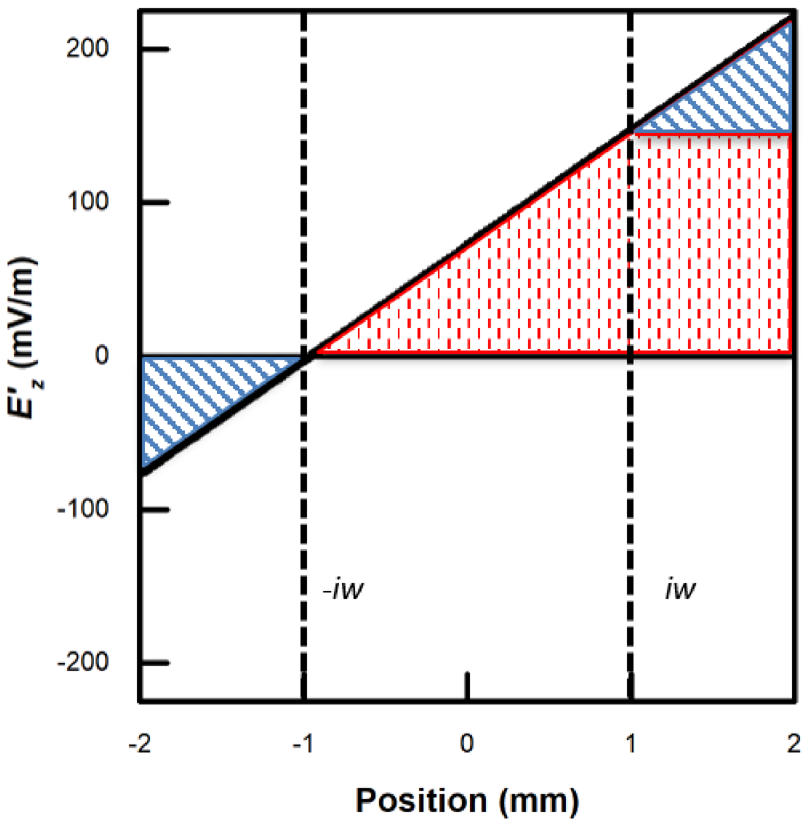

Figure 5.5: Illustrative plot showing E'_z as a function of position across the conductor width for the constant J_c ($n = 200$) model when $i = 0.5$, $B_{a0} = 100$ mT and $\omega t = 2\pi$. The blue-shaded regions represent equal and opposite contributions to the spatially averaged electric field which sum to zero. The red-shaded area shows the net averaged electric field at this moment in the cycle. Note that the same linear behaviour is observed in the $n = 20$ model. The dashed lines show $x = \pm\ iw$

Plot 5.3(b) shows that the behaviour of the magnetic field inside the superconductor broadly follows the periodic behaviour of the applied field, and reaches its maximum and minimum values at approximately the same time as the applied field. These peak internal fields occur at either edge of the superconductor in the region in which screening currents are being erased. At the edge where screening currents run parallel to the transport current, the local magnetic field within the superconductor is much larger than B_{a0}. Once the applied field magnitude passes its peak value (at $\omega t = (2m{+}1)\pi/2$), a new screening current distribution is established in the tape. The new screening current distribution then enables a very low magnetic field to persist throughout the superconductor whilst the applied field reverses polarity ($\omega t = m\pi$). At this point flux begins to enter the superconductor again from both edges, whilst a region of zero flux remains spatially-frozen close to the current-reversal zone [61]. This frozen flux gives rise to the characteristic contour spikes (i.e, 'spurs' and 'gullies') which are observed in the B-field plot.

Plot 5.3(c) shows the electric fields developed inside the conductor (in the z-direction). The electric field appears first at the edges, as soon as the screening currents have completed their reversal in each half cycle (e.g., shortly after $\omega t \approx 2\pi/3$). E-fields of opposite polarity occur at each edge, and decrease linearly towards the centre of the conductor (Figure 5.4 (c),(f) and (i)). The zone containing E-fields of the same polarity as I_{t} is always spatially larger than the zone of opposite polarity on the other side of the tape. Both zones achieve their maximum area when the magnitude of $\mathrm{d}B_{\mathrm{app}}/\mathrm{d}t$ is at a maximum, before then decaying again to zero as B_{app} reaches its positive or negative peak

The linear profile of E'_z across the tape is to be expected for a fully penetrated sample, as $\partial E_z/\partial x = \partial B_y/\partial t$. However, this E-field profile challenges the conventional viewpoint that the current source applies work only to the central region of the tape, where the DC transport current is assumed to flow [22, 56, 58, 61]. Figure

5.5 shows why this is the case.

Figure 5.5 illustrates the linear E'_z profile across the tape which occurs at all times in the cycle when flux penetrates throughout the tape. It is clear that the E-field at one edge of the tape is significantly larger than at the other edge, and hence the net sum of the E-field from both edge regions does not sum to zero. As a result, the net integrated E-field across the tape (as shown by red shaidng) extends all the way to the right-hand edge of the tape. This implies that a DC current source must do work on currents flowing throughout the red shaded region, and not just in the central region from x = -iw to +iw (as described in [18, 56, 58, 130]). This also confirms that it is not possible to spatially distinguish between the transport current and screening currents of the same polarity. In fact, the largest contribution to the dynamic resistance occurs at the right-hand edge of the tape in figure 5.5, contradicting the conventional assumption that solely screening currents flow in this edge region.

This observation raises in turn the interesting question: why the analytical equations discussed in Chapter 2 yield good estimates of R_{dyn}, despite being based on the flawed assumption of a centrally-localised transport current. The reason for this is that the derivation of equation (2.13) ultimately requires only that a quantity of net flux traverses a net total transport current, I_{DC} [61]. The differences in equations 2.15 and 2.16 relate to different approaches used to estimate the threshold field, but the precise location within the tape at which these interactions occur does not affect the derivation or resulting analytical expression.

5.5.2 SuperPower $J_c(B,\theta)$ Model

The internal fields and currents calculated by the interpolated $J_c(B,\theta)$ model can also be visualised in the same fashion as for the constant J_c model above. This is shown in figure 5.6, which also shows the evolution of the sheet critical current K_{cB} in time and space. The instantaneous sheet values are shown in figure 5.7 at the times indicated by the dashed horizontal lines in figure 5.6. Unlike the constant J_c model, K_c now varies as a function of the local field. Modelled data is shown for the same values of reduced current and applied field amplitude as were used in figure 5.3 ($i = 0.5$ and $B_{a0} = 100$ mT).

Several different features are apparent in the behaviour of the currents and fields from the interpolated $J_\mathrm{c}(B,\theta)$ model, compared to the constant J_c model for the SuperPower tape. Plot 5.6(a) shows the evolution of K_z and we see that in this case, screening currents running anti-parallel to the transport current do not occupy a constant width throughout the cycle. Instead, the maximum penetration width of screening currents into the tape occurs when $B_\mathrm{app} = 0$ ($\omega t = m\pi$), and retreats as B_app increases in magnitude. This is because the local K_{cB} decreases as $|B_\mathrm{app}|$ increases, meaning the transport current must occupy a wider fraction of the tape, which reduces the remaining space available for opposing screening currents to flow. As before, the complete erasure of the screening current distribution from the previous half-cycle coincides with ΔV increasing rapidly from zero (e.g, dashed line at $\omega t = 2\pi/3$). We can also see some subtle asymmetries between the current distributions for the positive and negative half-cycles of the applied field, which can be understood in terms of the asymmetric $J_\mathrm{c}(B,\theta)$ behaviour of the SuperPower tape shown in figure 3.3.

Plot 5.6(b) shows the evolution of B'_y within the conductor and its features are very similar to the constant J_c model. At the points in the cycle when the screening currents penetrate furthest into the tape ($\omega t = m\pi$), the perpendicular magnetic field is close to zero over the entire width of the conductor. This also corresponds to a peak in the local K_{cB} across the entire cross-section of the conductor – as shown in plot 5.6(c). The low-field contour spikes in B'_y are also present for the interpolated $J_\mathrm{c}(B,\theta)$ model, but exist for a shorter duration and move outwards to follow the retreating current reversal zone (between $\omega t = m\pi$ and $\omega t = m\pi{+}\pi/2$).

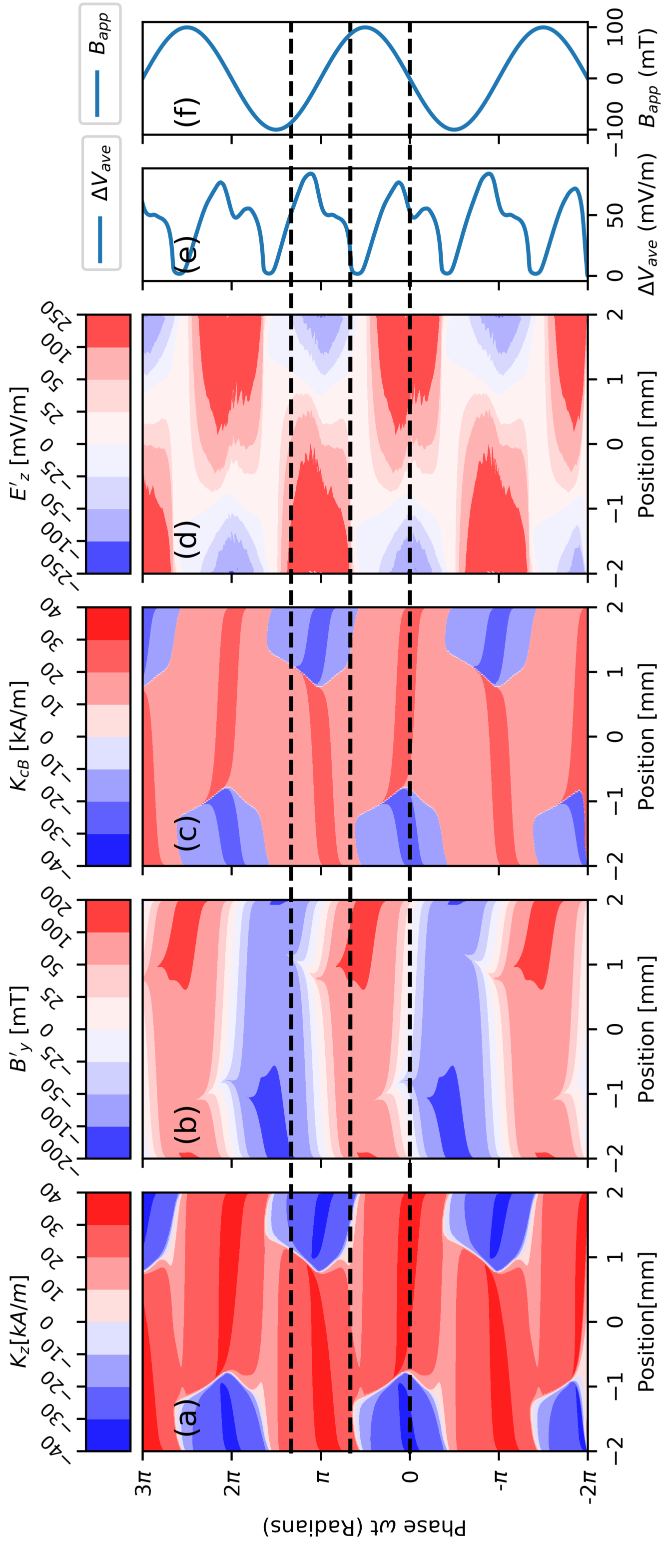

Figure 5.6: Time evolution of the interpolated $J_c(B,\theta)$ model for the SuperPower tape. The sheet variables K_z, B'_y, K_{cB} and E'_z (a,b,c,d) alongside ΔV (e) and $B_{app}(t)$ (f) are given for two and a half cycles of the applied field. Here $i = 0.5$, $f = 118.66$ Hz and $B_{a0} = 100$ mT.

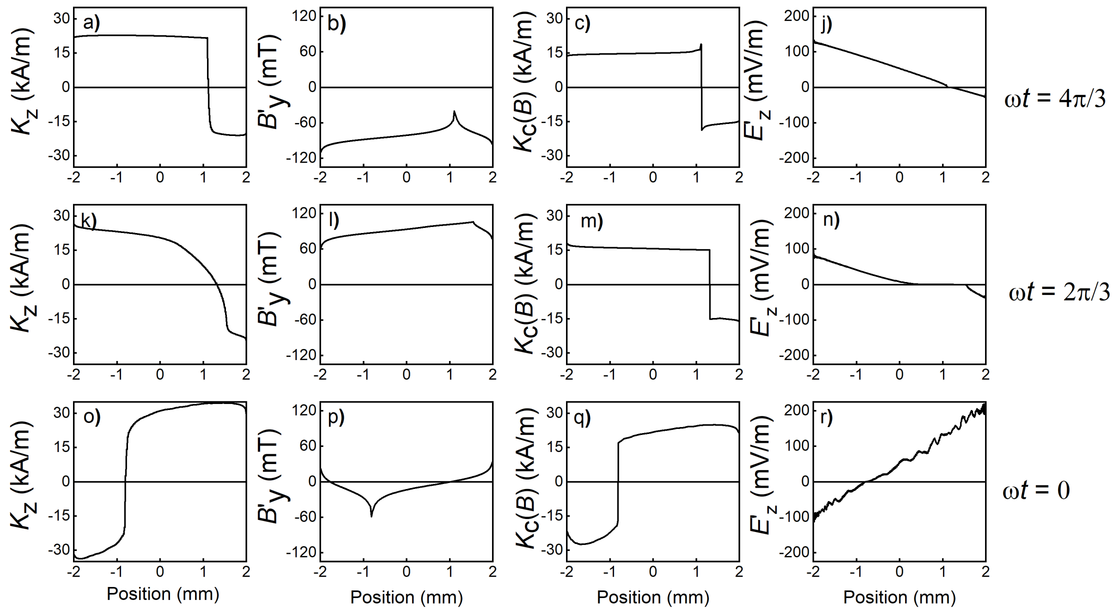

Figure 5.7: Shown are the instantaneous profiles across the conductor width for K_z (plots (a,k,o)); B'_y (plots (b,l,p)); K_{cB} (plots (c,m,q)); and E'_z (plots (j,n,r)) for the interpolated $J_c(B,\theta)$ model for the SuperPower tape at the three moments-in-time indicated by the dashed lines $\omega t = 0$, $2\pi/3$ and $4\pi/3$.

Plot 5.6(d) shows the E'_z-fields within the conductor, calculated using the interpolated $J_\mathrm{c}(B,\theta)$ model. These exhibit qualitatively similar behaviour to the constant J_c model, but there is a clearly noticeable difference to the shape of the resistive lobes (shown as red in this plot). These now show the 'peak splitting' phenomenon which was previously observed in the ΔV waveforms (see figure 5.2(c) and (d)). Comparing plots 5.6(c),(d) and (e), we see that the local minima in ΔV at $\omega t = m\pi$ coincides with the double-humped shape of the resistive E'_z-field lobe. We can now deduce that the short-lived reduction in ΔV is caused by the increase in K_c (and equivalently J_c) across the tape at this point in the cycle, which in turn arises because $|B_\mathrm{app}|$ has become sufficiently small. Equation (5.3) requires that the increase in local J_c must deliver a decrease in the electric field required for currents to flow at this point in the cycle, and hence the local minima in ΔV.

5.5.3 SuNAM $J_\mathrm{c}(B,\theta)$ Model

Figure 5.8 shows contour plots of the calculated sheet fields and currents for the SuNAM tape using the interpolated $J_\mathrm{c}(B,\theta)$ model. Again, the instantaneous sheet values are shown in figure 5.9 for the three times indicated by the dashed horizontal lines in figure 5.8. The same conditions are used as for the SuperPower tape shown in figure 5.6 (i.e., $i = 0.5$, $f = 118.66$ Hz and $B_{a0} = 100$ mT).

We see many of the same gross features are apparent as are observed for the SuperPower tape, but there are also some significant differences which arise from the differing $J_\mathrm{c}(B,\theta)$ properties of these two tapes. In particular, the screening currents shown in plot 5.8(a) do not show a maximum penetration width at $\omega t = m\pi$. There is also no obvious asymmetry in the distribution of currents between positive and negative halves of the oscillating magnetic field.

In figure 5.8(b) it can be seen that the low field regions near the current reversal zone persist longer than is the case for the SuperPower tape, due to the increased

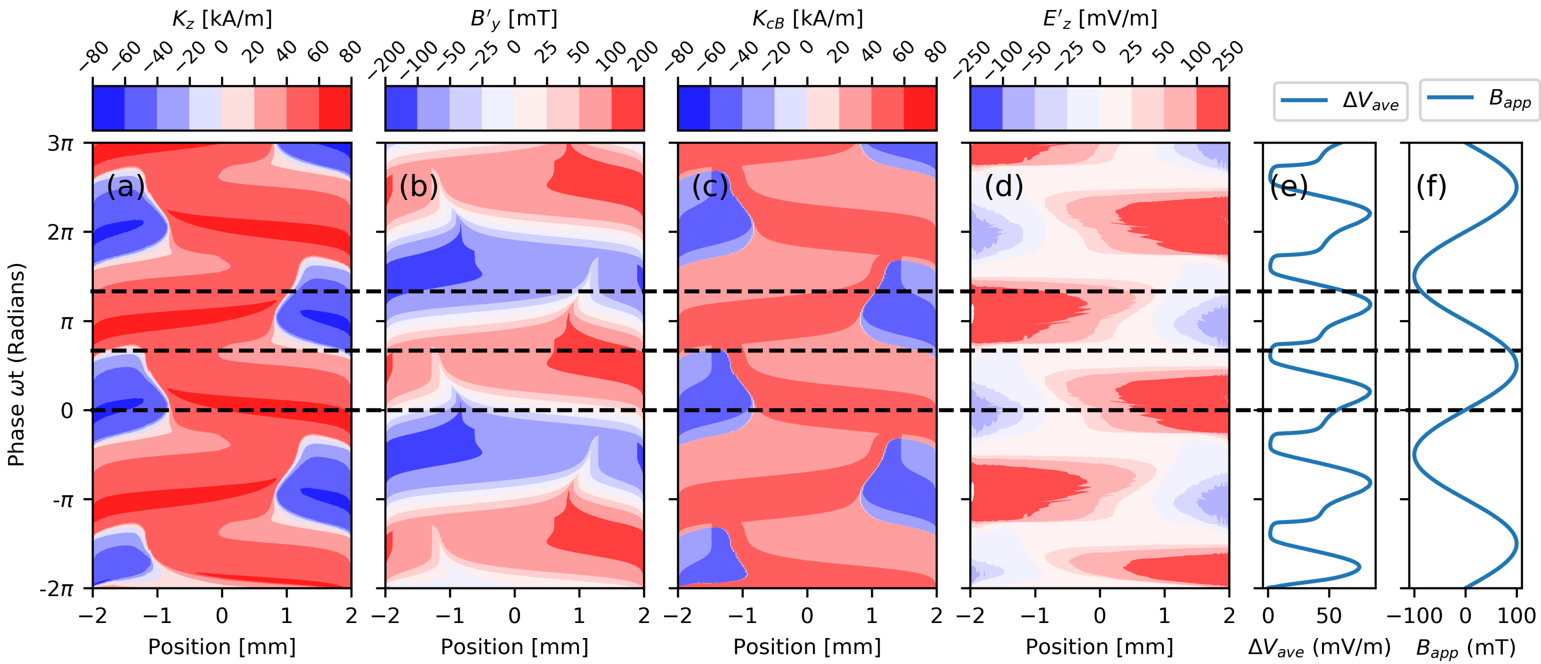

Figure 5.8: Time evolution of the interpolated $J_\mathrm{c}(B,\theta)$ model for the SuNAM tape. The sheet variables K_z, B'_y, K_{cB} and E'_z (a,b,c,d) alongside ΔV (e) and $B_\mathrm{app}(t)$ (f) are given for two and a half cycles of the applied field. Here $i = 0.5$, $f = 118.66$ Hz and $B_{a0} = 100$ mT.

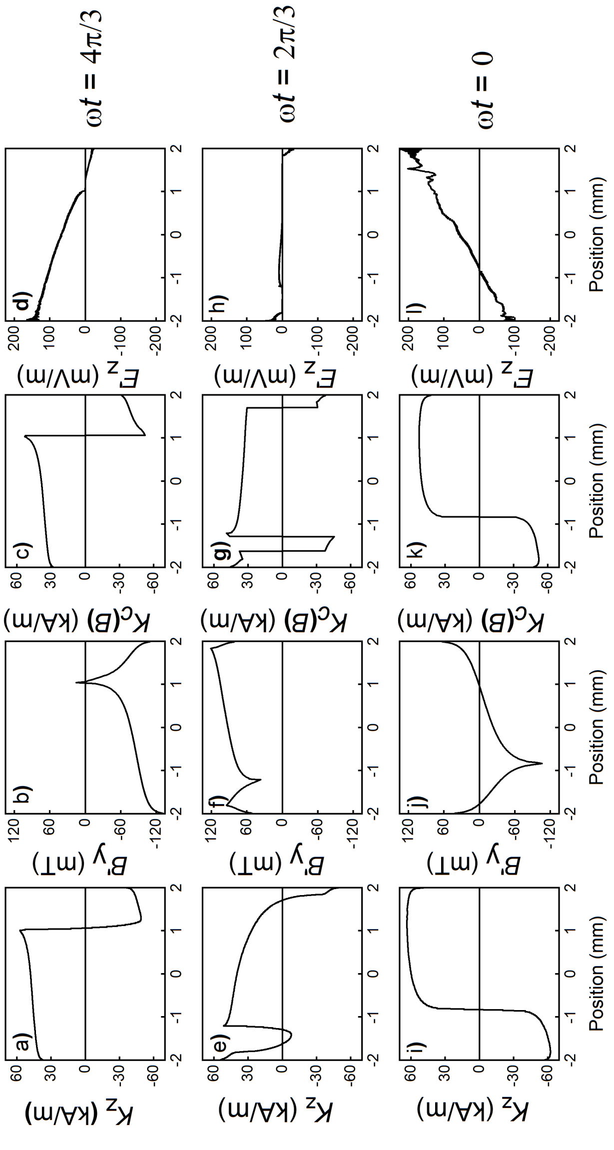

Figure 5.9: Shown are the instantaneous profiles across the conductor width for K_z (plots (a,k,o)); B'_y (plots (b,l,p)); K_{cB} (plots (c,m,q)); and E'_z (plots (j,n,r)) for the interpolated $J_c(B,\theta)$ model for the SuNAM tape at the three moments-in-time indicated by the dashed lines $\omega t = 0$, $2\pi/3$ and $4\pi/3$.

shielding from the larger critical current of the SuNAM tape. This results in a broadening of the periodic increase in K_c, visible in plot 5.8(c), that occurs when B_{app} is close to zero ($\omega t = m\pi$). This broadening 'smears out' the effect of the

increased K_c, which results in a less pronounced peak splitting of E'_z and ΔV. It should be noted that this smearing effect occurs even though the SuNAM tape exhibits a substantially stronger $J_{\text{c}}(B,\theta)$ dependence than the SuperPower tape. This emphasises the complex nature of these effects, which are only captured by the detailed finite element model.

5.6 Scaled Constant J_{c0} Model

A final comparison between the constant J_{c} and interpolated $J_{\text{c}}(B,\theta)$ models is shown in figure 5.10. This figure compares the voltage waveform, ΔV(t), obtained from the interpolated $J_{\text{c}}(B,\theta)$ model with the waveforms calculated from two different constant J_{c} models (n = 20). The first model used is the $J_{\text{c}} = J_{\text{c0}}$ model already presented, whilst the second model sets J_{c} equal to the minimum value during the cycle, such that $J_{\text{c}} = J_{\text{c}}(B_{a0})$. Figure 5.10 shows values obtained from these three models for both SuperPower and SuNAM tapes for the same ratio of B_{app} / $B_{\text{th}} \approx 6$ in each case, such that $B_{a0} = 60$ mT and 150 mT for the SuperPower and SuNAM cases, respectively (it should be noted that the 150 mT field simulated here for the SuNAM tape lies beyond the experimentally accessed conditions shown in figure 5.2).

In both cases, it is clear that the interpolated $J_{\text{c}}(B,\theta)$ waveform is essentially bounded by waveforms obtained from the two constant J_{c} models. The interpolated $J_{\text{c}}(B,\theta)$ model predicts the emergence of a non-zero voltage response at the same time as the constant $J_{\text{c}} = J_{\text{c}}(B_{a0})$ model and has similar peak values. However, in the sections shaded grey, the interpolated $J_{\text{c}}(B,\theta)$ model deviates away from this waveform and instead converges to the constant $J_{\text{c}} = J_{\text{c0}}$ model. The shaded grey regions denote those times in the cycle during which $B_{\text{app}}(t) = 0 \pm B_{\text{th}}$, such that the internal magnetic field is small. As such, the approximation $J_{\text{c}} = J_{\text{c0}}$ represents

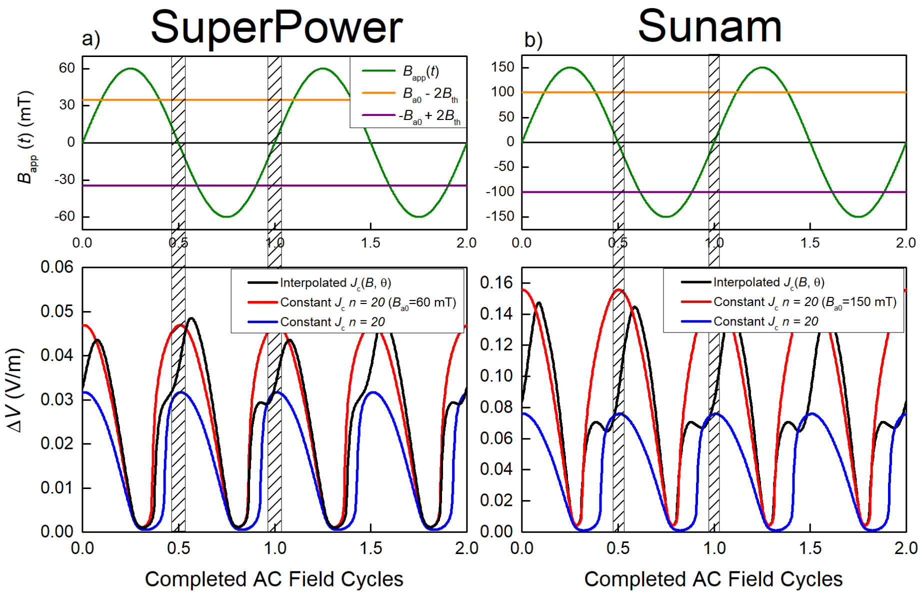

Figure 5.10: Comparison of the voltage waveform ΔV for a) SuperPower and b) SuNAM tapes from three different models. Two constant J_c models are considered, both of which employ $n = 20$; Constant $J_c = J_{c0}$ in blue and $J_c(B_{a0})$ in red. The interpolated $J_c(B,\theta)$ model is shown in black. $B_{a0} = 60$ mT in the SuperPower case and 150 mT for the SuNAM data. In both cases, $i = 0.5$.

a better description of the situation within the tape at these times.

Taken in conjunction with the previous analysis from figures 5.6 and 5.8, it can be concluded that the experimentally-observed peak splitting in $\Delta V(\mathrm{t})$ is due to the periodic increase of $J_c(B,\theta)$ across the entire conductor width at those times in the cycle when $B_{\mathrm{app}}(t)$ approaches zero.

5.7 Summary Discussion

In this chapter a 2D numerical finite element model based on the $\boldsymbol{H}$-formulation has been used to calculate the transient and DC dynamic resistance generated in two different coated conductor tapes. These modelling results have been analysed and compared with experiment.

In terms of the DC values for the dynamic resistance, the FE model employing a constant J_c with a realistic value of $n = 20$ significantly underestimates the experimentally measured values for both the SuperPower and SuNAM tapes. By contrast, the FE models which include the full $J_c(B,\theta)$ and $n(B, \theta)$ dependence of the tapes show excellent agreement.

The limitations of the constant J_c FE model are further highlighted when the transient time dependent voltage waveforms are compared with experiment. Contour plot visualisations of the time-evolution of the sheet currents and fields within the conductor show a rich variety of features which vary subtly depending on the applied fields and currents, and the specific $J_c(B,\theta)$ dependence. Only the interpolated $J_c(B,\theta)$ model is able to reproduce the peak-splitting effect observed in the experimental transient voltage waveforms. This effect arises due to a short-lived increase in the local critical current at the centre of the tape, caused by the varying local magnetic field. As the applied field passes through zero, the critical current at the centre of the tape reaches a maximum thus reducing the local E-fields throughout the tape.

It is interesting to note that a FE model approximating to the critical state (where n is taken to have a highly elevated value of 200) also shows good agreement with reality. This is despite the fact that neither the n-value nor J_c used in this FE model actually correspond to physical reality. Similarly, analytical equations 2.13, 2.15, and 2.16 (which are derived from critical state assumptions [18, 56, 58]) also show excellent agreement with our DC experimental data. A key assumption in the derivation of the analytical equations is that electrical work is performed upon a DC transport current which flows solely in the central region of the tape. However, our FE models show that resistive electric fields extend to the edge of the tape, implying that electrical work is being done throughout the region carrying positive current (i.e, in the same direction as the DC transport current). A corollary of this observation is that it is not possible to spatially distinguish between regions carrying the DC transport current and the screening current flowing in the same direction.

In light of these observations, it is perhaps surprising that the analytical equations based on the critical state do produce such close agreement with the experimental DC values. However, this can be understood by observing that equation (2.13) simply describes the electrical work required in each cycle to move a net packet of flux across a total DC transport current. The precise location at which this work is done is not relevant to the total work. A similar argument holds for the constant J_c ($n = 200$) FE model, which closely approximates to the critical state.

The different results obtained using the constant J_c ($n = 20$) model are perhaps more puzzling. Following the logic above, this implies that the constant J_c FE model predicts that less flux traverses the tape per cycle as the n-value decreases. This suggests that, for the range of experimental conditions examined here, the use of an artificially inflated n-value (e.g., $n = 200$) approximately compensates for the errors incurred by assuming a constant $J_\mathrm{c} = J_\mathrm{c0}$. However, it is not clear that this compensating effect will hold across a broader range of experimental parameters, and indeed there have been a small number of reported experimental results which are not well described by the analytical equations, such as those in [67, 68, 72]. As such, it is expected that the interpolated $J_\mathrm{c}(B,\theta)$ FE model presented here should generally deliver more reliable results for a coated conductor in an arbitrary field, current, and geometry.

6

Dynamic Resistance in Parallel Connected Vertical Stacks

In the previous chapter, the dynamic resistance of a single tape was investigated in detail. For high-current, high-field applications superconducting cables are often employed and thus exploration of switching phenomenon for these configurations is necessary. There are several different HTS cable designs[131–135], but a particularly simple variant is the vertical stack of parallel connected HTS tapes which is the subject of this chapter. Due to the low resistivity of HTS tapes, minor variations in solder resistance (at each tapes termination) can cause significant changes to the current sharing behaviour within the cable. This makes experimental measurements of short cable lengths very challenging, and for that reason only FE analysis is presented in the following chapter. First in Section 6.2, a small cable comprised of four tapes is studied. A comparison between the I-V characteristics of the cable and an isolated tape is given as well as analysis for the cable similar to that of chapter 5, i.e. the time averaged dynamic resistance and threshold fields are computed for a variety of transport currents and applied fields. The spatial distribution of the DC current within the cable throughout the cycle of the applied magnetic field is also presented. Subsequently in section 6.3, analysis is presented for stacks with an increasing number of tapes. The threshold fields are again computed as the number within the tapes is increased and the transition from strip to slab like behaviour is discussed.

This chapter contains the work of two publications. Both are published in IEEE Transactions on Applied Superconductivity. Section 6.2 10.1109/TASC.2020.2974860 and Section 6.3 10.1109/TASC.2021.3059593.

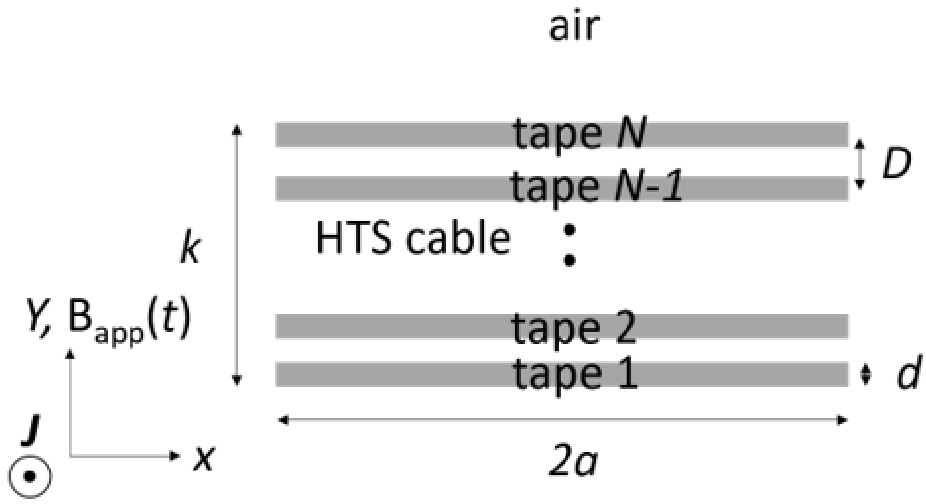

Figure 6.1: FE model geometry detailing the orientation of coordinate axes, and direction of transport current, $\boldsymbol{J}$, (out of the page) and applied magnetic field, B_{app}, relative to both the single wire and parallel-connected stacks.

6.1 Finite Element Geometry

Figure 6.1 shows the finite element geometry and relevant quantities used throughout this chapter. N represents the number of tapes within the cable, D, the centre to centre spacing between tapes, d, the individual tape thickness, k, the total cable height and a, the half width of a single tape. The problem dimensions are the same as those presented in chapter 5, consisting of a 2D cross-section of the HTS tape or cable in the xy-plane, with infinite length along the z-axis. The governing $\boldsymbol{H}$-formulation equations are given in 3.1.1. In this chapter, an interpolated $J_{\mathrm{c},\mu\mathrm{V}}(B,\theta)$ model is used, which employs experimentally measured values for $J_{\mathrm{c},\mu\mathrm{V}}$ and n as outlined in section 3.2.1. Two tapes are considered here, the SuperPower and SuNAM data from Figure 3.3 are used in Section 6.2 and Section 6.3 respectively. As in chapter 5, the current and field distributions within the cable are calculated in two stages. The first is a linear ramp to the desired transport current I_{t} (with a fixed $\mathrm{d}I_{\mathrm{t}}/\mathrm{d}t$ of 100 As^{-1} in section 6.2, and 10 As^{-1} in section 6.3) and secondly, the application of an oscillating magnetic field of the form $B_{\mathrm{app}}(t)$=$B_{\mathrm{a0}}\sin(\omega t)$. This field is applied for 2.5 complete cycles and the dynamic resistance computed from the final cycle. This is done so that initialisation effects in the first cycle can be ignored. It is important to note here that throughout this chapter, I_c refers to the critical current determined using a 1 μV/cm criterion, although minor references are made to the saturation current $I_{c,S}$. In this chapter, the thickness of the superconducting layer has been expanded by a factor 100. This is done to reduce the computational time required while not significantly impacting the FE results as demonstrated in [94, 98, 136].

To compute the time averaged values for the dynamic resistance, first the instantaneous spatially averaged electric field, $E_{\mathrm{T_N}}$,

$$E_{\mathrm{T_N}}(t) = \frac{1}{A_{\mathrm{T_N}}} \iint_{A_{\mathrm{T_N}}} E_{\mathrm{z}}(x, y, t) dx dy \tag{6.1}$$

and the net instantaneous DC current within the tape, $I_{\mathrm{T_N}}$,

$$I_{\mathrm{T_N}} = \iint_{A_{\mathrm{T_N}}} J_z(x, y, t) dx dy \tag{6.2}$$

are computed, where $\mathrm{T_N}$ denotes the N^{th} tape and $A_{\mathrm{T_N}}$ the associated cross-section within the FE model. As all of the tapes are simulated to be parallel connected, $E_{\mathrm{T_N}}$ has the same value for all tapes (note that this is only true in the fully penetrated regime where the $\partial A/\partial t$ contribution to the scalar potential is negligible). However, the instantaneous current within each tape is variable. Thus the time averaged dynamic resistance for each tape is given by

$$\frac{R_{dyn,T_N}}{fL} = \int_{\frac{1}{f}}^{\frac{2}{f}} \frac{E_{\mathrm{T_N}}(t)}{I_{\mathrm{T_N}}(t)} dt \tag{6.3}$$

The time-averaged value for the cable is determined using the equation for resistive components connected in parallel

$$\frac{fL}{R_{\mathrm{dyn,cable}}} = \sum_{n=1}^{N} \frac{fL}{R_{\mathrm{dyn,Tn}}} \tag{6.4}$$

6.2 Four Tape Stack

In the following section the simple case of a four tape stack is considered. The relevant analytic equations for the threshold field in an infinitesimally thin superconducting strip is given in Section 2.5. In this section, the SuperPower wire has a half-width $a = 2$mm, thickness $d = 100\mu$m (after artificial expansion), and centre to centre spacing $D = 300\mu$m.

6.2.1 *I-V* Curves and Current Filling in Zero Applied Field

Figure 6.2 shows the numerically calculated I-V curves obtained when ramping the DC current in both a single tape and the stacked cable in zero applied field (i.e. self-field). Experimental data obtained from a self-field transport measurement on a short sample of the SuperPower SCS4050-AP YBCO tape [21] is also shown. The measured critical current of a single tape is denoted by I_{c0} and for the SuperPower tape studied in this work, was 102.6 A. The flux-creep exponent, n, determined from a power-law fit to the measured E-J curve is 27. J_{c0} is determined by dividing I_{c0} by the area of the HTS film cross-section. Experimentally, a small non-zero voltage is measured for the single tape at currents below I_{c0}, which is attributed to incomplete current transfer between the current and voltage taps due to the short sample length [137].

As discussed previously, it is not generally possible to make experimental measurements on a short sample (e.g, less than several meters) of a parallel stack of tapes, as small variations in the soldered contact resistance become increasingly important [138, 139]. Instead one must rely on numerical modelling to determine the behaviour in this arrangement. The experimentally measured I_{c0} and FE model results for the single tape I_{c} are in close agreement at 100.5 A and 102.6 A, respectively. The stacked cable FE model gives a cable critical current, $I_{\mathrm{c,cable}}$, value of 334.6 A, which is ~80% of the critical current of four isolated coated conductor tapes. This reduction in $I_{\mathrm{c,cable}}$ is due to the increased self-field from neighbouring tapes in close proximity within the stack. This has also been observed

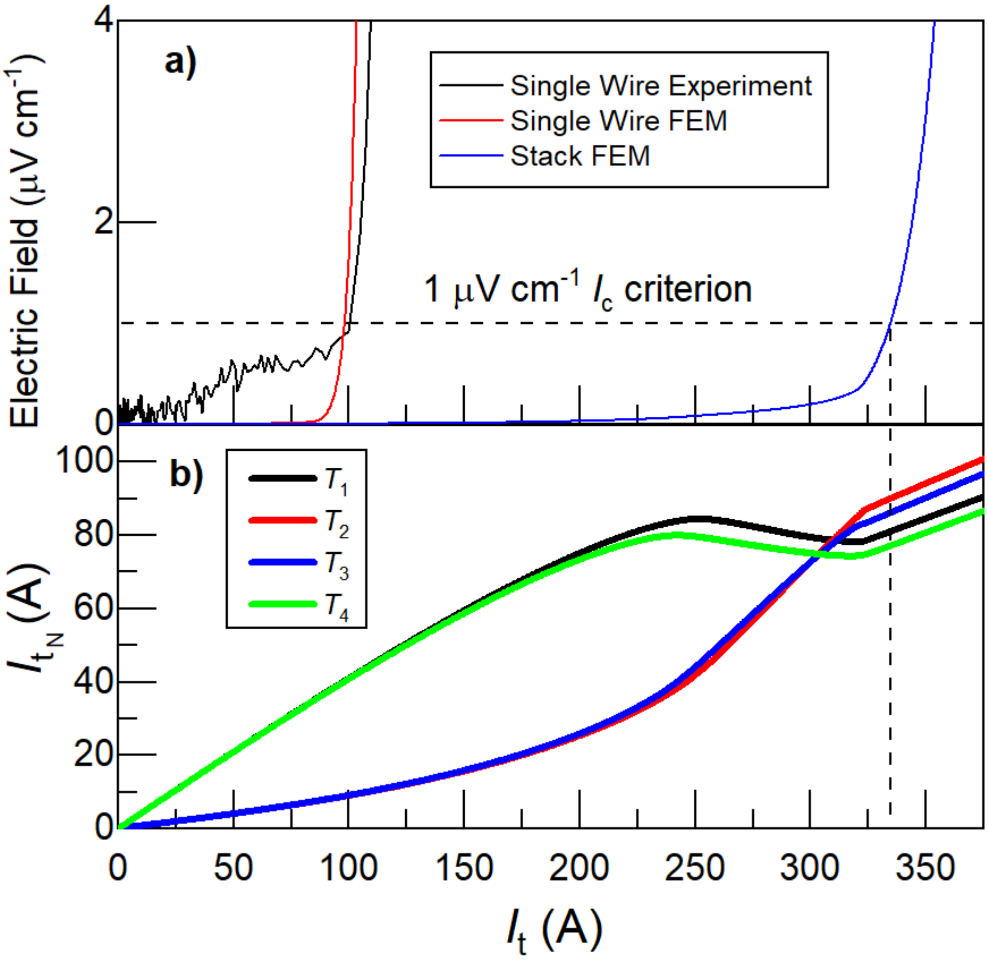

Figure 6.2: (a) Self-field *I*-*V* curves for a single tape, as measured experimentally in self-field and simulated using the FE model. This is shown alongside the simulated *I*-*V* curve for the cable in self-field. The horizontal dashed line shows I_c as defined by the 1 μV/cm criterion. (b) DC current within each tape of the cable during the DC ramp. The vertical dashed line indicates the DC current within each tape at the 1 μV/cm criterion.

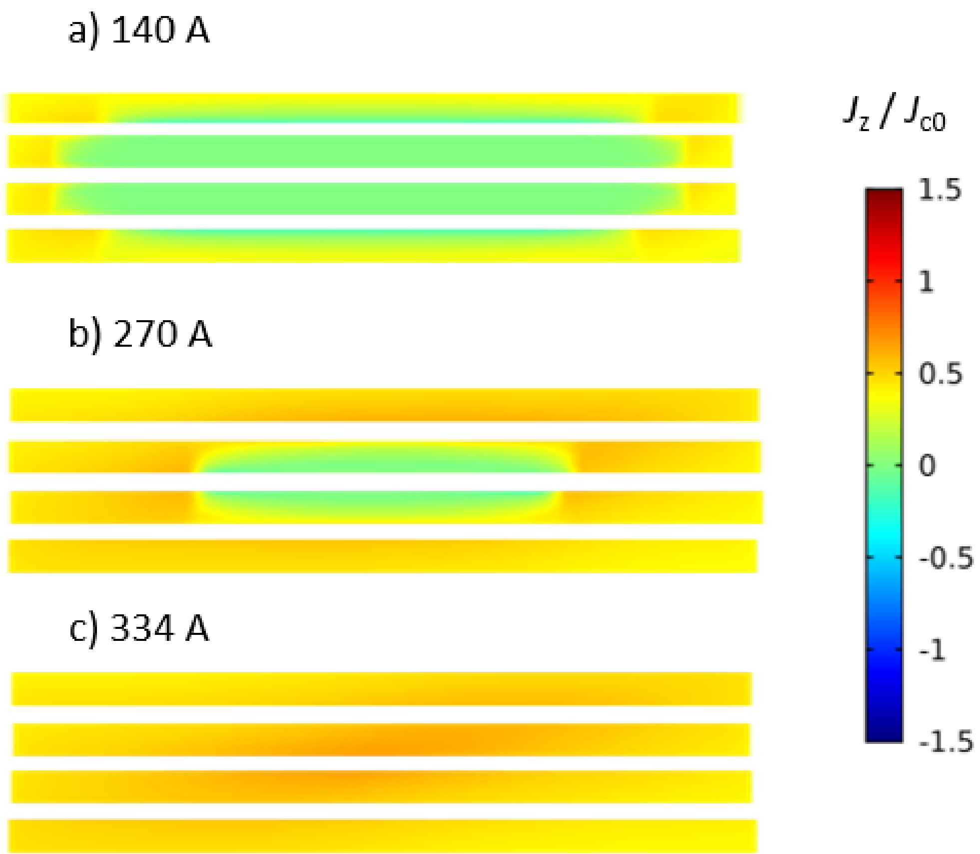

Figure 6.3: Model cross-sections displaying the current density as a function of position at different times during the DC ramp. Plots (a), (b) and (c) show J_z / J_{c0} at 140 A, 270 A and 334 A. The tape aspect ratio has been adjusted to assist the viewer.

in a series-connected stack of tapes reported in [71]. As DC current is injected into the cable, it must distribute itself amongst the four tapes. This is shown in Figure 6.2 (b). First, current is injected primarily into the outer tapes in the stack (T_1 and T_4). As the total current in the cable increases, the share of the total current carried by the inner tapes (T_2 and T_3) increases. Once I_t reaches approximately 90% of $I_{c,cable}$, a crossover occurs with the transport current primarily occupying the centre tapes. The saturation current for this particular ramp rate occurs just before I_c (determined using the 1 μV cm^{-1} criterion) as can be seen by the equal linear gradients for each tape beyond this point[140]. Further understanding of the evolving current distribution in the stack during the initial current injection can be obtained by examining the current density across the full cross section of the stacked cable. Figure 6.3 (a), (b), and (c) show the current density as a fraction of J_{c0} at three moments during the current ramp; when $I_{\rm t}$ is 140 A, 270 A, and 334.6 A. The parallel connected stack can be considered to behave similar to a superconducting bulk, in the sense that when $I_{\rm t}$ is well below $I_{\rm c,cable}$, the current density is largest near the surface. This manifests as current flowing across the entire width of the outermost tapes, T_1 and T_4, as well as at both edges of the interior tapes, T_2 and T_3. As the total transport current is increased, the outer tapes become saturated with DC transport current across their entire cross-section, leaving a small shielded region which exists only in the central regions of tapes T_2 and T_3. At $I_{\rm c,cable}$ this shielded region disappears, and the critical current of each tape is determined by its $J_c(B,\theta)$ properties and the local magnetic environment. The inner tapes experience a smaller field contribution from their neighbouring tapes than the outer tapes, which is why the inner tapes carry a slightly larger proportion of the total current. The reason for this is that the inner tapes have neighbouring tapes both above and below. This symmetry leads to the perpendicular magnetic field contribution from each neighbouring tape being partially cancelled out. The outer tapes experience the full contribution from their neighbouring tapes, and hence experience a larger perpendicular field and consequently, a lower $J_{\rm c,\mu V}(B,\theta)$

6.2.2 Resistance per AC Field Cycle

Figure 6.4 (a)–(d) show the values calculated from the FE model using equations 6.3 and 6.4 for the dynamic resistance per cycle, for each tape and the total cable. Analytical values for the cable obtained from equations 2.13, 2.15, and 2.16 are also shown. The dynamic resistance is calculated for four different values of the reduced current i = 0.3, 0.5, 0.7, 0.9, and for a single frequency f = 65 Hz. The $R_{\rm dyn}$ values are plotted as a function of the applied field amplitude B_{a0}. For all reduced currents, there is a single threshold field value below which the DC values for the dynamic resistance in each tape is negligible. Only once the applied field amplitude exceeds this threshold value does the time-averaged resistance for each tape begin

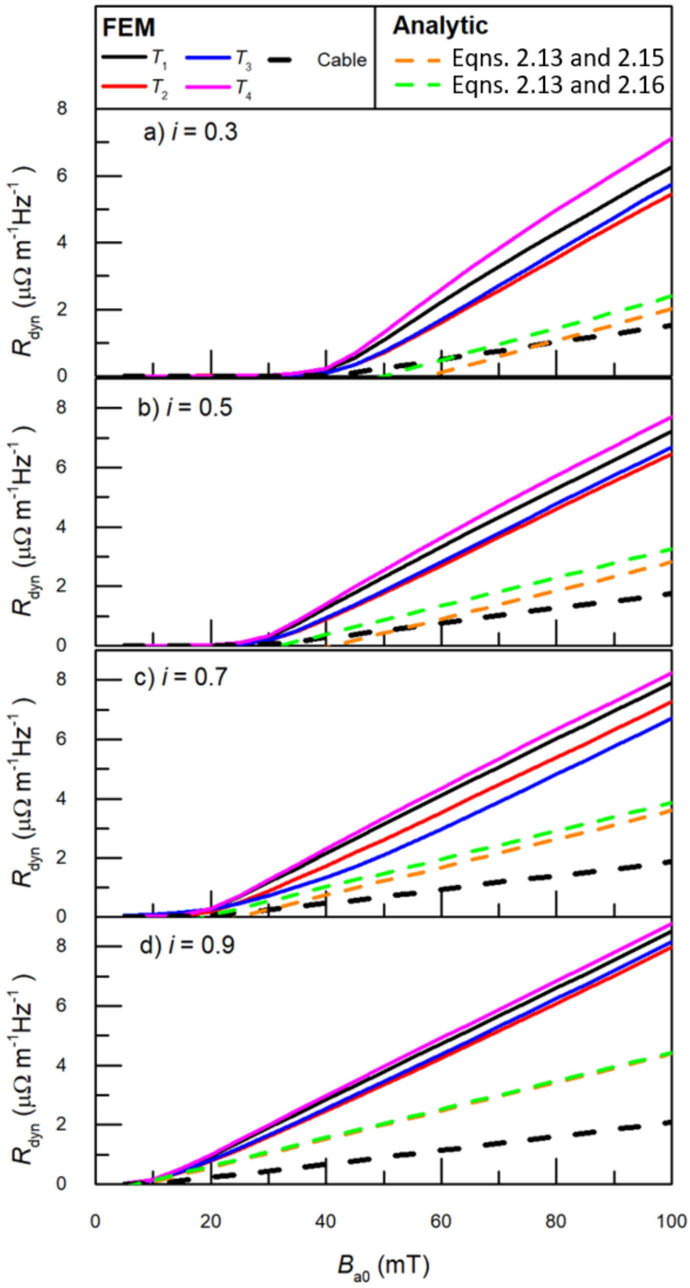

Figure 6.4: Time averaged values for the dynamic resistance and the threshold fields. Plots (a), (b), (c), and (d) show the time averaged resistance for four different values of i = 0.3, 0.5, 0.7, and 0.9 in AC field amplitudes up to 100 mT.

to linearly increase. This is because the parallel connection of tapes in the stack ensures that transport current is dynamically redistributed, such that the potential drop along each tape is identical. This situation differs from a series-connected stack of tapes [71], where the transport current in each tape is constrained to be equal and hence shielding effects mean that dynamic resistance emerges in the outer tapes well before it is observed in the inner tapes. For all values of i, the outermost tapes in the stack have a larger DC dynamic resistance compared to the interior tapes. This is because they carry a greater proportion of shielding currents, and consequently a smaller proportion of the total transport current than the inner tapes. When $i = 0.9$, the difference between the dynamic resistance of each tape decreases significantly. This reflects the fact that the cable can support less screening currents at highly elevated values of i.

6.2.3 Transient Electric Field and Current Sharing in a Sinusoidal Perpendicular Field

The DC values for R_{dyn} presented in Section 6.2.2 are calculated from the transport current and the time-averaged electric field in each tape in the cable. These transient quantities vary over the alternating field cycle. In particular, screening currents redistribute during the cycle which causes the net DC transport current component to also move between the exterior and interior tapes. Figure 6.5 shows the current distribution at eight moments over a single cycle of the applied field with $B_{\mathrm{a0}} = 20$ mT $< B_{\mathrm{th}}$ and $i = 0.5$. As expected, a significant fraction of the cable interior has current densities well below J_{c}. In this regime, there is no flux transfer across the cable and no net DC electric field. Figure 6.6 shows the current density at the same eight different times during a single cycle of the applied magnetic field when $i = 0.5$ and $B_{\mathrm{a0}} = 100$ mT. Plot (a) shows the moment $B_{\mathrm{app}} = 0$ mT and is increasing. Screening currents of opposite polarity to the DC current flow on the left-hand side of the cable and penetrate slightly further into the exterior tapes. The right-hand side of the cable accommodates the sum of screening currents and the DC transport current. At this instant in the cycle, dissipation is occurring across the entire conductor and E_{cable} is increasing. Figure 6.6(b) shows the current distribution by B_{app} = 100 mT after 1.25 cycles. At this moment E_{cable} has fallen from its peak value and almost decayed to zero. The total induced screening currents flowing in the stack have decreased since Figure 6.6(a). This is evident from the reduced area of the return path on the left-hand side of the cable, along with the global reduction in the magnitude of the current density. Figure 6.6(c) shows the moment shortly after the applied field has reached its maximum, where B_{app} = 86 mT and is now decreasing (This occurs after 1.333 complete cycles in Figure 6.7). Now, E_{cable} is at its minimum value (see figure 6.7 (c)). Interestingly, this is occurring sometime after $\mathrm{d}B_{\mathrm{app}}/\mathrm{d}t = 0$. Figure 6.6(c) shows new return paths for negative polarity screening currents appearing now on the opposite edge of the tape. At the same time, negative currents which were previously flowing on the left side are now being gradually erased by positive

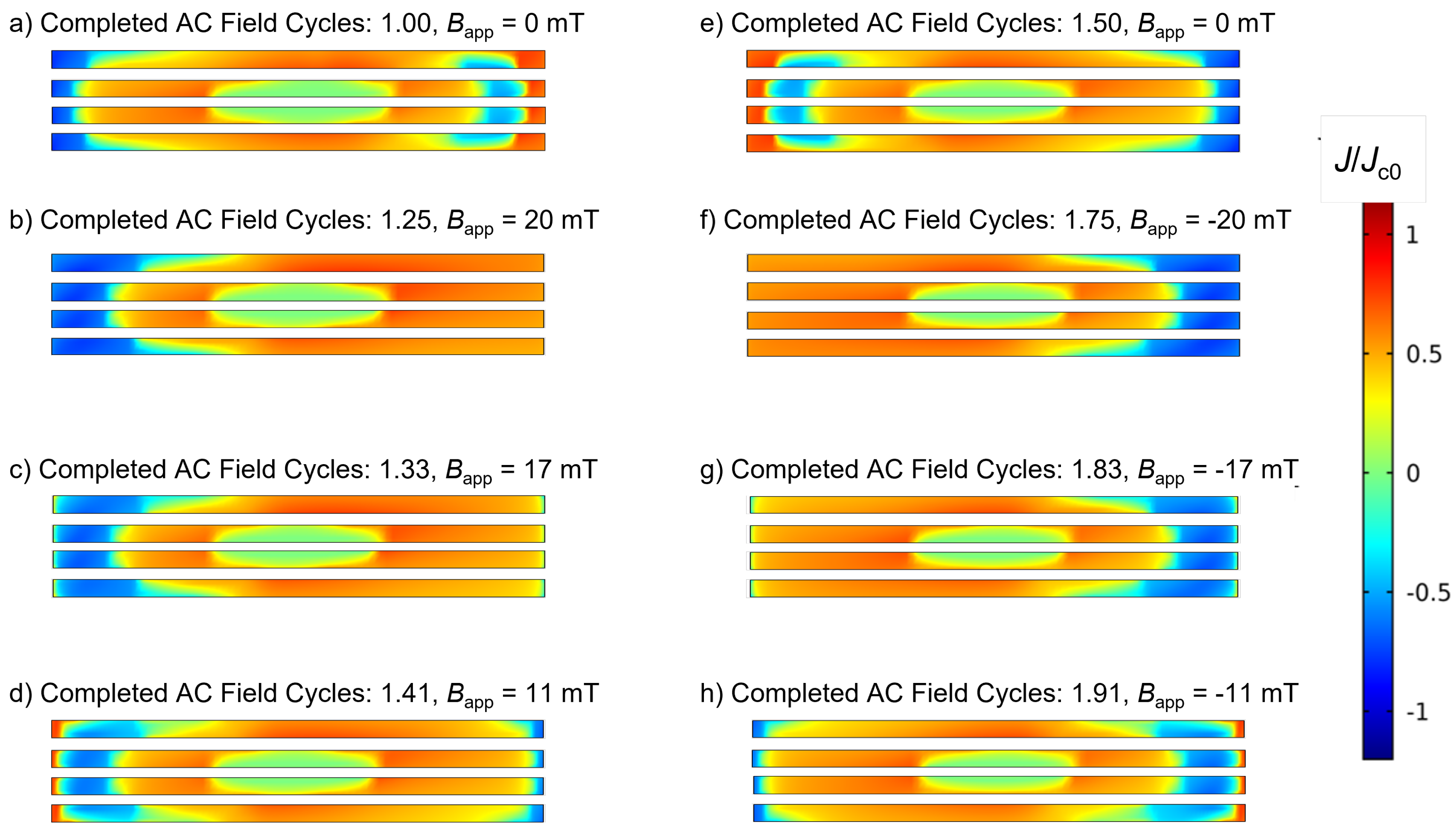

Figure 6.5: Model cross-sections showing J_z/J_{c0} within the cable as a function of position at eight separate instances during a single cycle as indicated by the solid black circles (a–h) in Figure 6.7(a). The magnitude of the current density is indicated by the colour scale on the right-hand side. $B_{a0} = 20$ mT, $i = 0.5$.

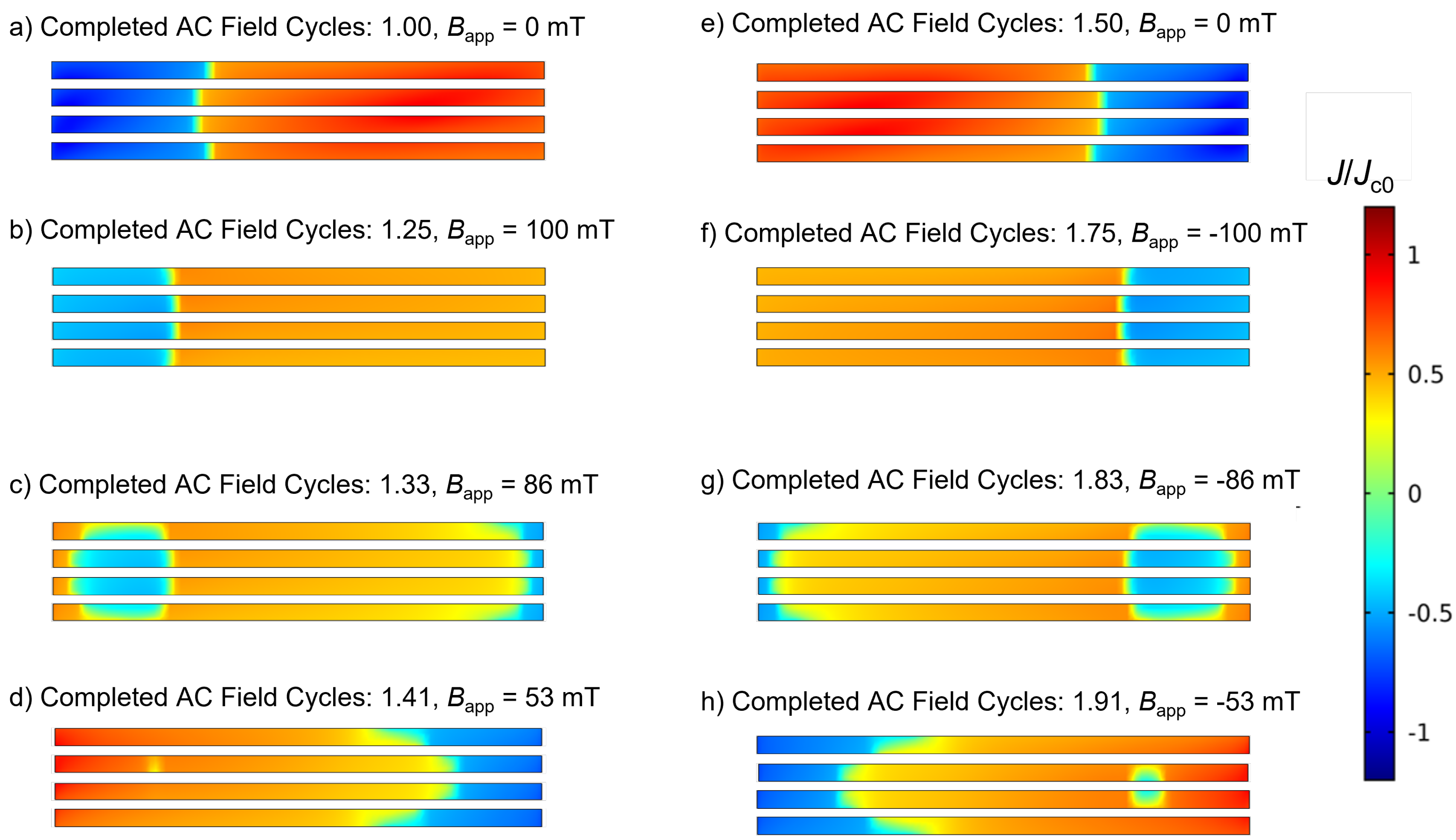

Figure 6.6: Model cross-sections showing J_z/J_{c0} within the cable as a function of position at eight separate instances during a single cycle as indicated by the solid black circles (a–h) in Figure 6.7(a). The magnitude of the current density is indicated by the colour scale on the right-hand side. $B_{a0} = 100$ mT, $i = 0.5$.

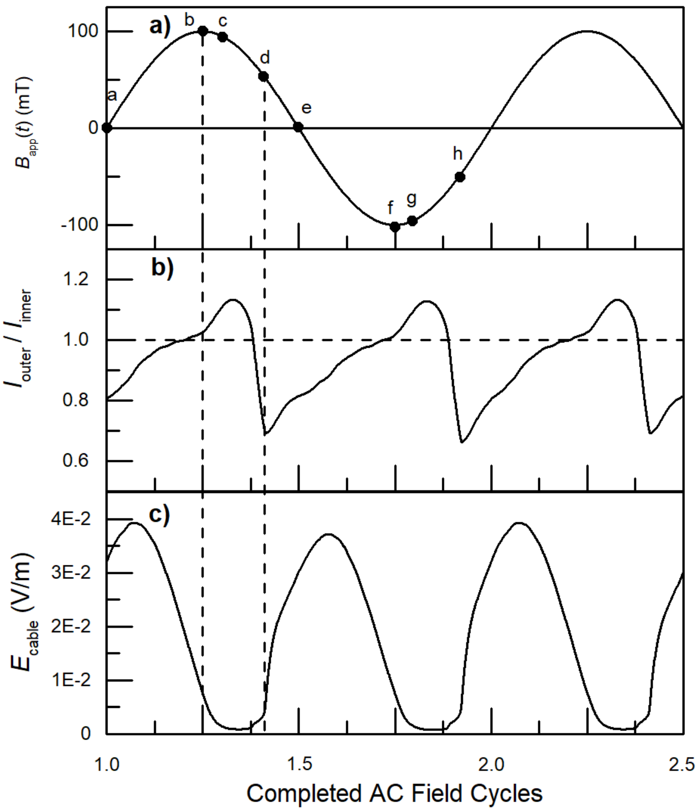

Figure 6.7: (a) Phase of the applied magnetic field with $B_{\mathrm{a0}} = 100$ mT. (b) and (c) Show the time dependence of I_{outer}/I_{inner} and E_{cable} for $i = 0.5$. These plots span 1.5 cycles of the applied field. The solid black circles in (a) indicate the eight instances in time referenced in Figure 6.6. The dashed lines indicate when the applied magnetic field $B_{\mathrm{app}} = B_{a0}$ and $B_{a0} - 2B_{\mathrm{th}}$ (B_{th} calculated using eqn. 2.15).

currents encroaching from the left edge. These residual screening currents vanish first in the exterior tapes leading to a short-lived peak in the DC current contained in the exterior tapes (see Figure 6.7(a)). Shortly afterwards, the residual 'island' of screening currents is also erased from the interior tapes, which are then able to accommodate a greater proportion of the transport current.

By Figure 6.6(d), the applied field has dropped to $B_{\mathrm{app}} = 53$ mT, and 1.41 AC field cycles have passed. At this moment, the negative screening currents on the left-hand side have vanished entirely. This coincides with the rapid increase from zero of E_{cable}. It should be noted that the applied field at this moment is approximately equal to B_{a0} - $2B_{\mathrm{th}}$. After this moment current distributions - which

are the mirror image of those in Figure 6.6(a–d) - are observed in Figure 6.6(e–h) as the AC field goes through the negative half of the AC field cycle.
This narrative is presented again in figure 6.7. Here, the same eight separate moments during the applied field cycle are shown, which correspond to the labelled points in figure 6.6. Figure 6.7(b) shows the time-dependence of the ratio of transport current carried by the outer and inner tapes respectively when $i = 0.5$ and $B_{\text{a0}} = 100$ mT. This is expressed as $I_{outer}/I_{inner} = (I_{T_1} + I_{T_4})/(I_{T_2} + I_{T_3})$. Figure 6.7(c) shows how the transient variations in this ratio also correspond to the transient electric field across the stack, E_{cable}. (Again note that the idealised parallel connection between every tape in the stack means that $E_{\text{cable}} = E_{T_N}$ for all tapes).

In Figures 6.7(b) and (c), we see the evolution of $I_{\text{outer}}/I_{\text{inner}}$ and E_{cable} over 1.5 cycles of the applied AC field. The dashed lines show the window in which the applied magnetic field decreases from its peak value of B_{a0} to approximately B_{a0} - $2B_{\text{th}}$ (calculated using equation 2.15). This is the point in the cycle at which the Bean model predicts that screening current reversal is no longer capable of shielding the interior from the changing external field [71], and hence holding the interior electric field at its minimum value. Immediately following this window, there is a sharp rise in E_{cable} and simultaneously a greater proportion of the DC current moves into the interior tapes. This occurs as the screening currents are driven in the outer tapes to oppose the rapidly changing applied field and hence the DC current component is driven into the inner tapes. The ratio of DC current, I_{outer}/I_{inner}, then steadily increases until the applied field reaches the opposite polarity peak and the process then repeats in the next half-cycle.

The time-varying distribution of transport current between tapes is observed at all applied field amplitudes. Figure 6.8 shows the time dependence of I_{outer}/I_{inner} and E_{cable} for a range of B_{a0} values (with $B_{a0} > B_{\text{th}}$). At increasing values of B_{a0}, the maximum value of I_{outer}/I_{inner} increases, indicating that a greater proportion

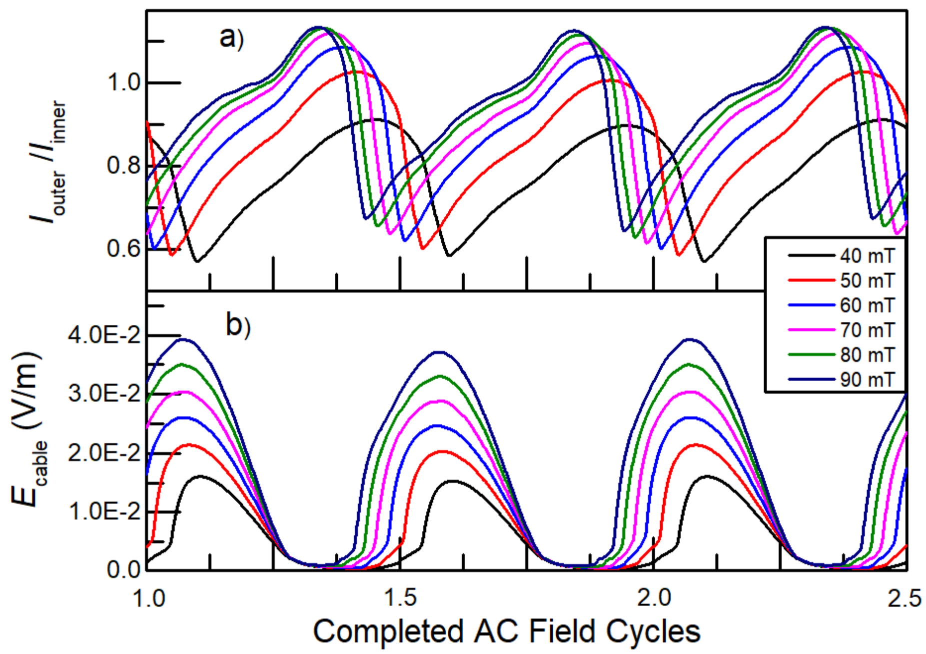

Figure 6.8: Time dependence of (a) I_{outer}/I_{inner} and (b) E_{cable} for a range of B_{a0} values over 1.5 cycles of the applied magnetic field for $i = 0.5$.

of the interior tapes are taken up by reversing currents during the period between B_{a0} and B_{a0} - $2B_{\mathrm{th}}$ (equivalent to Figure 6.6(c)). We also observe that the peaks in the E_{cable} waveform broaden and increase in amplitude with increasing B_{ao}. This directly causes the DC value of R_{dyn} to increase as shown in Figure 6.4.

6.3 Vertically Stacked Cables with a variable Number of Tapes

In the following section, the evolution of B_{th} in cables comprised of N tapes connected in parallel is investigated. As mentioned earlier, this section uses the measured SuNAM $J_{\mathrm{c},\mu\mathrm{V}}(B,\theta)$ and n data. The values for B_{th} calculated from the FE model are compared to values obtained from the corresponding slab, strip, and stack equations presented in Section 2.5. In this section, the tape thickness d = 130 μm, the centre-to-centre spacing D = 200 μm, and the tape half width a = 2 mm. The overall cable thickness is $k = (N\text{-}1)D{+}d$. Unlike the previous section, the

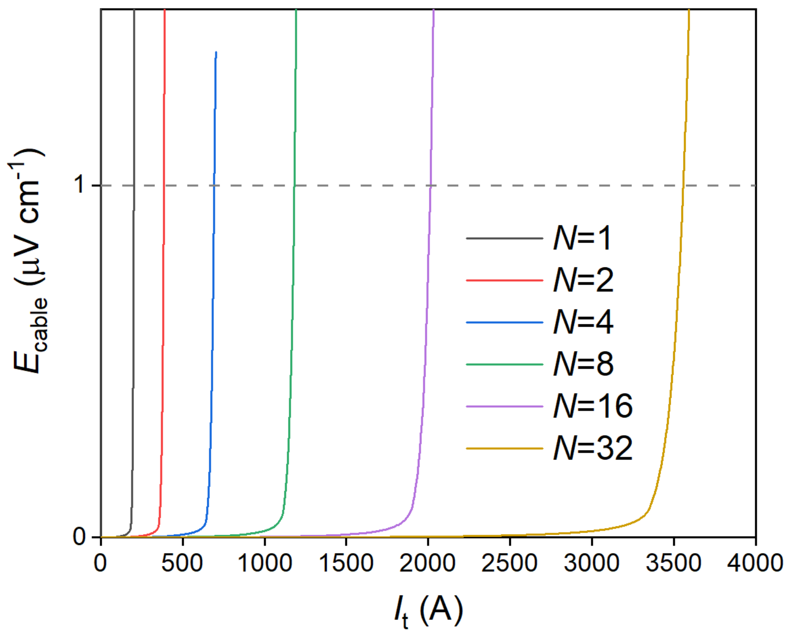

Figure 6.9: Simulated *E*-*I* curves for vertically stacked cables comprised of 1-32 tapes.

frequency of the applied magnetic field is 100Hz, noting here that the dynamic loss is independent of frequency for frequencies on the order of hundreds of Hz [61, 70].

6.3.1 Calculated I_c Values

First, simulated I_c tests are performed for each cable configuration so that a value of J_c can be determined for use with equations 2.15, 2.14, and 2.17. The same electric field criterion of 1μVcm^{-1} is applied when determining I_c for each N. The calculated *E*-*I* curves are shown in Figure 6.9. In Figure 6.10, these values are shown compared with the I_c of a single tape multiplied by the number of tapes within the cable. The calculated $I_{c,cable}$ values begin to diverge significantly when $N > 8$. This reflects the suppression of J_c due to the increasing magnetic field generated by neighbouring tapes. The value of J_c used in the analytic equations is determined by dividing the calculated $I_{c,cable}$ by the total cable cross-section, i.e. $J_c = I_c \;/\; 2ak$. This is consistent with previous reports showing that HTS cables can be modelled as a single bulk with a reduced J_c [141].

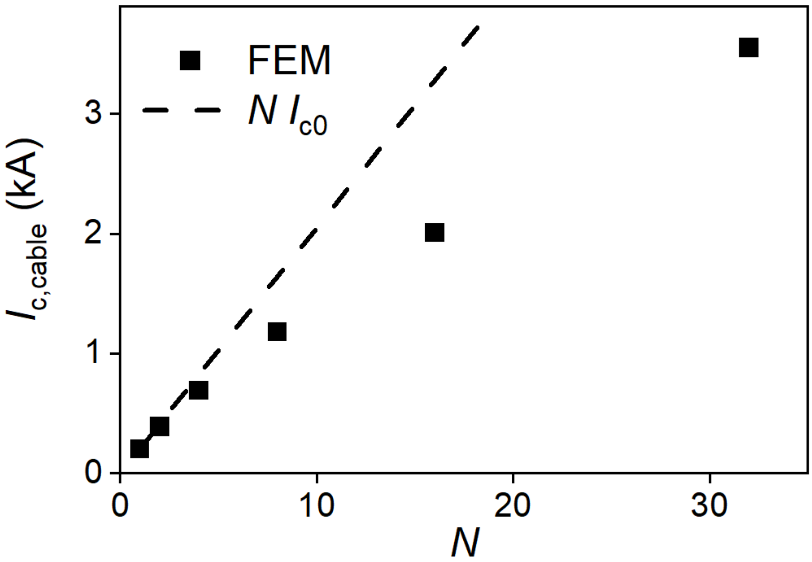

Figure 6.10: Calculated I_c values using the 1 μV cm^{-1} criterion from Figure 6.9 as a function of tape number N. The dashed line shows the value obtained by multiplying the I_c of a single tape in isolation by N.

6.3.2 Threshold Fields

The threshold fields for each cable is calculated in the same manner described in section 6.2.3, taking the B_{a0} intercept from linear fits to the non-zero regime in plots of $R_{dyn,cable}$ as a function of B_{a0}. These are presented alongside values calculated using equations 2.14, 2.15, and 2.17 for various values of i in Figure 6.11.

For N = 1, 2, and 4, the FE data shows clearly non-linear behaviour at low transport currents, $i < 0.3$. There is exceptional agreement between the FE data and the strip and stack equations for $N = 1$ and $i > 0.3$ but only the strip expression retains this agreement for transport currents below $0.3I_c$. As the aspect ratio of the cable decreases with increasing N, the non-linear behaviour occurs at progressively lower currents, vanishing by $N = 8$. At higher values of N, the strip and slab expressions swap in terms of agreement with the FE data while the stack expression remains in close agreement throughout.

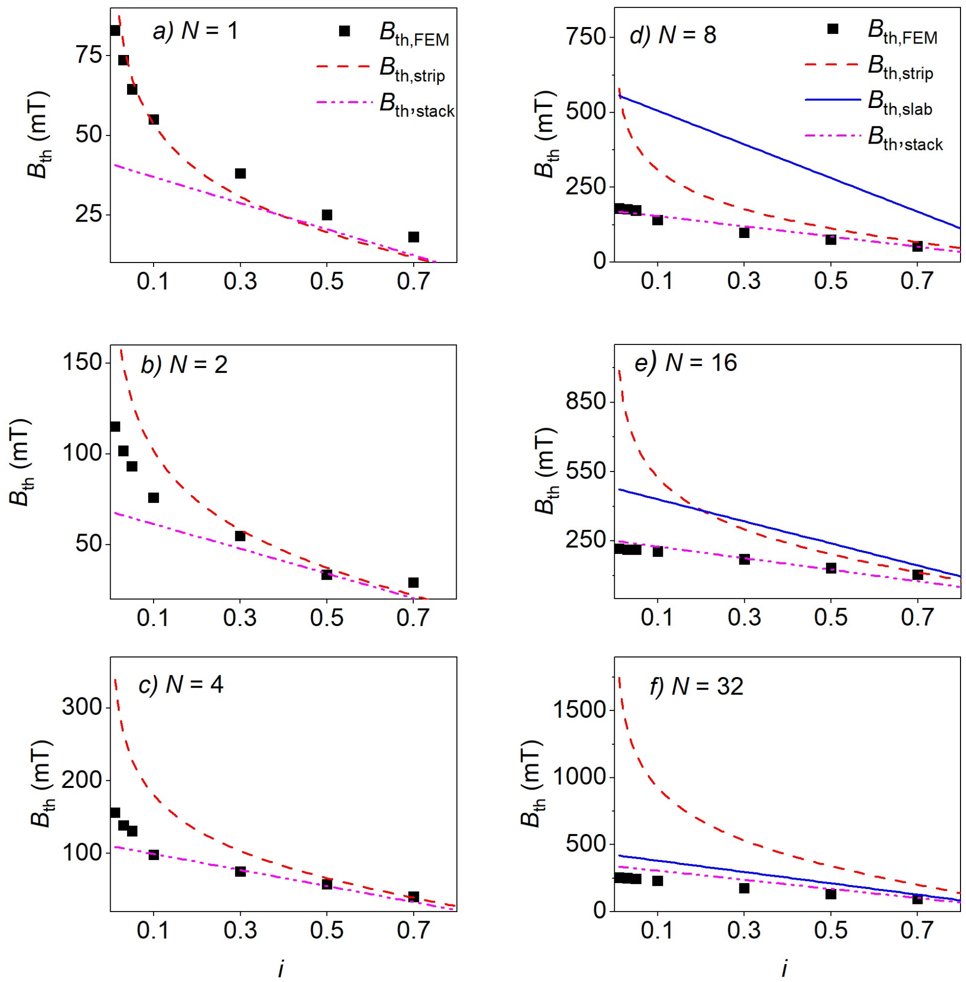

Figure 6.11: Calculated values for B_{th} as a function of i obtained from the FE model and using equations 2.15, 2.14, and 2.17. Shown are results from N=1, 2, 4, 8, 16, and 32 in plots a-f.

Figure 6.12 shows the threshold field behaviour at 1% I_{c} for each cable. Again this highlights the transition in agreement between the strip and slab expressions as N increases. The stack expression is consistent over the entire range but begins to overshoot slightly for $N > 16$. It is interesting that the FE model yields similar results to the analytical expressions as the latter assumes a constant J_{c} while the FE model includes field dependent J_{c} values.

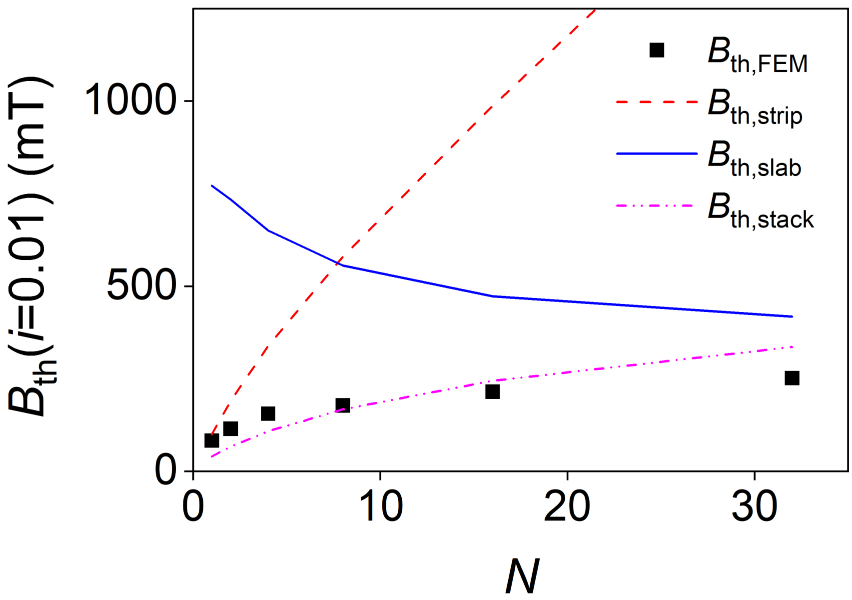

Figure 6.12: Calculated values for B_{th} and i=0.01 using the FE model and equations 2.14, 2.15, and 2.17 for all values of N.

6.4 Summary Discussion

In this chapter, the dynamic resistance has been modelled in parallel connected, vertical stacks of HTS tapes with varying aspect ratios. The numerical models are based on the ***H***-formulation and make realistic assumptions about the electrical properties of the superconductor, including field dependent critical current densities and physical values for the flux creep exponent n. When the transport current flowing through the cable is held constant and an alternating field applied, we observe a single threshold field above which the time-averaged values for the dynamic resistance increases linearly from zero for all tapes. The FEM values for the time-averaged dynamic resistance and threshold fields have varying levels of agreement with those from the different analytical models. The overall FE agreement with the analytical expression for stacks is exceptional in the linear regime for each cable. However dynamic resistance switching in the low i regime is only successfully described analytically in high aspect ratio tapes. FE analysis of this regime in cables indicates that none of the analytic models presented here can describe the cable over the entire range of transport currents. While cables consisting of a small number of tapes retain a high aspect ratio, the threshold fields cannot be described by a strip model with a constant critical current density.

When we examine the transient behaviour of the cable, it is evident that the transport current moves between flowing primarily in the exterior or interior tapes, in response to the varying applied magnetic field. The motion of current and flux in the y-direction cannot be described using the 1D geometry assumed for a strip. When the rate of change of the applied field changes polarity, screening currents appear on the edges of the tape which act to erase the screening currents from the previous half cycle. During this period, the electric field passes through its minimum values and most of the transport current flows in the exterior tapes. After the screening currents are completely erased, the electric field rapidly increases due to a combination of the suppression of the critical current and the increasing presence of screening currents. In these moments, the DC transport flows mostly in the interior tapes.

7
Effective Resistance of a Current-Carrying Hollow Strip in an AC Magnetic Field

As discussed in the previous chapters, a type-II superconductor carrying a DC transport current and subject to an alternating magnetic field can experience a dissipative DC electric field. This is dependent on whether or not the applied field is capable of fully penetrating the superconductor such that the screening and transport currents interact. This 'dynamic resistance' is generated by the flow of vortices across the conductor[53, 58]. As discussed in [88], a general expression for the dynamic resistance can be obtained by considering a superconducting hollow slab carrying a DC transport current while simultaneously exposed to an alternating magnetic field (see figure 7.1). In this chapter, FE analysis of a superconducting loop made from a hollow superconducting thin film is presented. Similar to the dynamic resistance in hollow slabs, it is expected that the underlying physics will be the same [58], however the form of the threshold fields in the hollow strip will differ due to the highly non-linear current and field profiles through the superconductor. In principle, the threshold fields for the hollow strip may be computed using the conformal mapping technique described in [38–40]. However, it is significantly easier to investigate the form of the threshold field in a hollow strip using finite element analysis as will be shown in this chapter. The computed values for the threshold field for the dynamic resistance are then compared with values predicted using the analytical models of section 2.5.1.1 for a single monolithic strip. These equations are repeated here.

$$B_{\text{th,strip}} = \frac{\mu_0 I_c}{2\pi a}\left[\frac{1}{i} ln\left(\frac{1+i}{1-i}\right) + ln\left(\frac{1-i^2}{4i^2}\right)\right] \tag{2.15}$$

and

$$B_{\mathrm{th,Jiang}} = \frac{4.9284\mu_0 I_{\mathrm{c}}}{\pi a}(1 - i) \tag{2.16}$$

where a is the half width of the strip. These expressions come from [58] and [61] respectively. These expressions show close agreement for transport currents $> 10\%$ of I_{c}. At present there is no analytical expression for the threshold field of a hollow strip with an arbitrary transport current. Thus the threshold fields for a monolithic strip are substituted to estimate the net DC electric field generated in the hollow strip. The field and current profiles during the AC field cycle calculated using the FE model are analysed using contour plots.

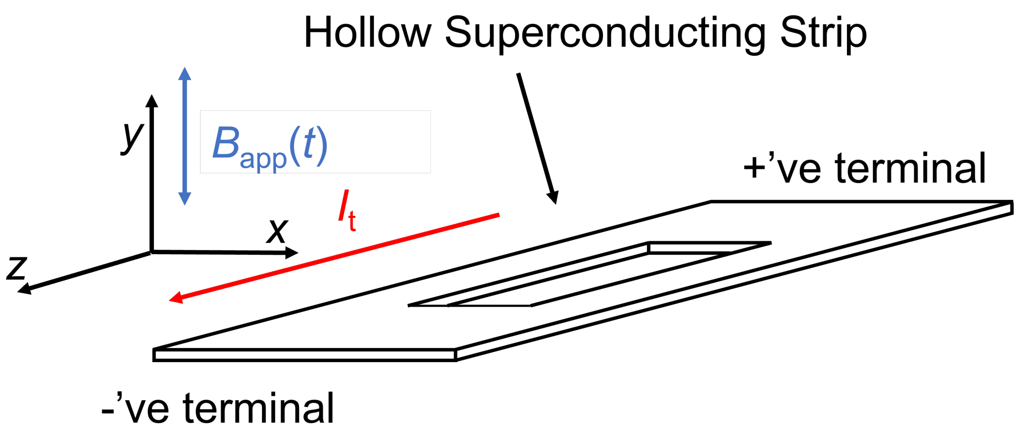

Figure 7.1: Superconducting loop made from a hollow superconducting thin film. The loop carries a DC transport current and is exposed to an alternating, transverse magnetic field.

7.1 Finite Model

The finite element model used in this chapter is a 2D model in the xy-plane with translational symmetry along z. As shown in figures 7.1 and 7.2, the hollow strip consists of two rectangular HTS cross sections connected in parallel with an air-gap between the two. A transport current flows along the positive z-direction with the alternating magnetic field applied in the y-direction. The finite element model uses the $\boldsymbol{H}$-formulation outlined in Section 3.1.1. with constant $J_{\mathrm{c},\mu\mathrm{V}}$ and n values.

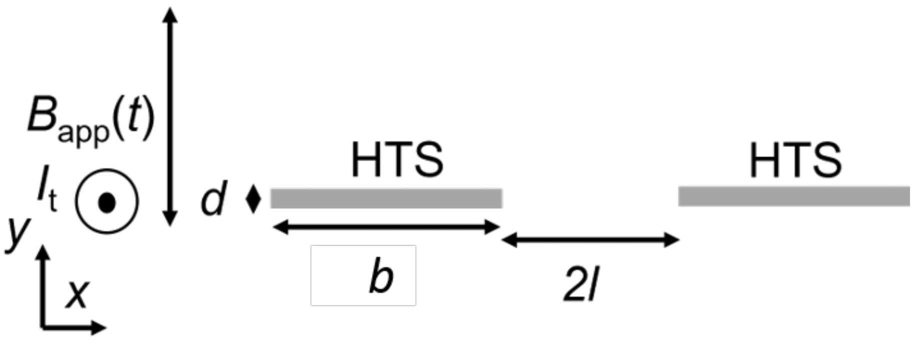

Figure 7.2: Finite element geometry of the superconducting switch. Shown are the relevant lengths as well as the applied transport current and AC field directions

Each superconducting branch has width b = 4 mm and a thickness of 100 μm. The half width of the air-gap, l, is 2 mm. The flux creep exponent was set at n = 30, the $I_{\mathrm{c,branch}}$ of a single branch is 105 A, and thus the critical current of the entire loop, I_{c}, is 210 A. The AC frequency f = 100 Hz. All of these are consistent with typical parameters for a commercially manufactured HTS tape and an experiment in a laboratory setting [71, 72, 76].

In a similar manner to the previous dynamic resistance chapters, currents and fields are computed in a two stage process. The details are essentially identical to that employed in the previous Chapters 4,5, and 6 where first a DC transport current, I_{t}, is applied to the conductor using an integral constraint

$$I_{\mathrm{t}} = \int_{\Omega} \mathbf{J} \cdot d\mathbf{\Omega} = I_{\mathrm{app}}(t) \tag{7.1}$$

where Ω is the union of the two HTS cross sections. In stage one, $I_{\mathrm{app}}(t)$ is a linear ramp with a gradient of 10 As^{-1}. This ramp is run until the desired transport is reached and then the transport current is held constant. Note that the critical current density of the superconductor is set to 26 kAm^{-1}. In stage two, a sinusoidal field, $B_{\mathrm{app}}(t)$=B_{a0}sin(ωt) is applied for multiple cycles. The FE values for the net DC electric field are then given by

$$E_{\mathrm{DC}} = \frac{f}{2bd} \int_{1/f}^{2/f} \int_{\Omega} \mathbf{E} \cdot d\mathbf{\Omega} dt \tag{7.2}$$

The spatial component of equation 7.2 is the instantaneous value of the spatially averaged electric field, denoted E_{ave}. The DC values of the electric field are computed from the second cycle where the transient values of E_{ave} are periodic with the applied field.

7.2 Results

7.2.1 Threshold Fields

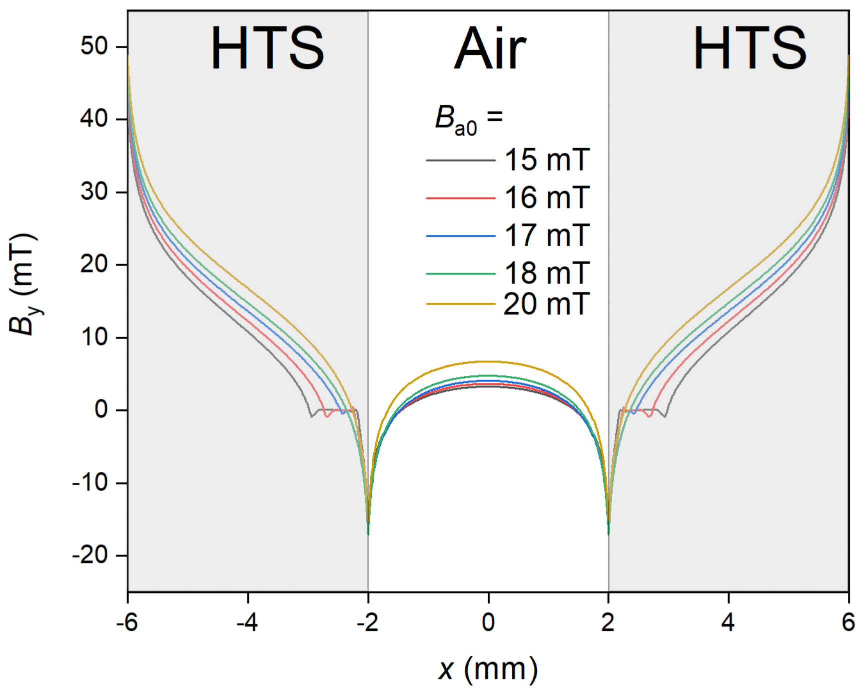

Figure 7.3: The magnetic field profile at peak applied field for various different values of B_{a0} as calculated using the FE model, with $I_{\mathrm{t}} = 0$ in all cases.

For the given geometry, the penetration field at zero transport current, B_{pen}, denotes the approximate limit of the threshold field. B_{pen} is the applied field at which flux penetrates the full width of both branches of the superconducting loop in the absence of any external current. Figure 7.3 shows the perpendicular magnetic field in the plane of the conductor at peak field for various different values of B_{a0} as calculated from the FE model. For lower field amplitudes, there is a region

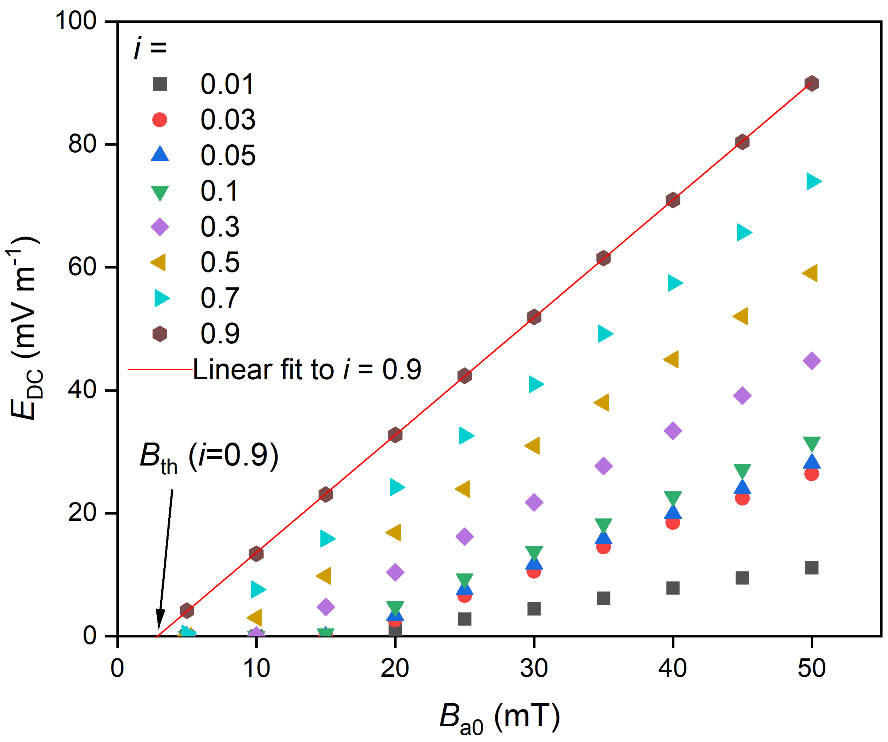

Figure 7.4: Calculated E_{DC} values as a function of B_{a0} obtained from the FE model. An example of a linear fit is shown for $i = 0.9$ as well as the corresponding B_{th} value

nearer to the interior edge of each HTS branch where the field is zero. As B_{a0} is increased, this shielded region decreases in size until by $B_{a0} = 18$ mT, the local magnetic flux density is non-zero everywhere except for two singular locations near to the interior edge of each tape. Thus, 18 mT approximates the upper bound for B_{th}.

For non-zero transport currents, B_{th} values are determined from the FE model in the same manner as the previous resistance chapters. They are obtained from linear extrapolations of the DC electric field as a function of field and transport current[61, 70, 76, 86, 129]. This is presented in figure 7.4. The FE threshold fields are then compared with values calculated using the analytical model for a single strip (equations 2.15 and 2.16) in figure 7.5.

When calculating the threshold fields using the analytical equations 2.15 and

	$B_{\text{th,StripA}}$	$B_{\text{th,StripB}}$	$B_{\text{th,JiangA}}$	$B_{\text{th,JiangB}}$
b (mm)	4	6	4	6

Table 7.1: B_{th} labels and input values for the parameter a used in equations 2.15 and 2.16

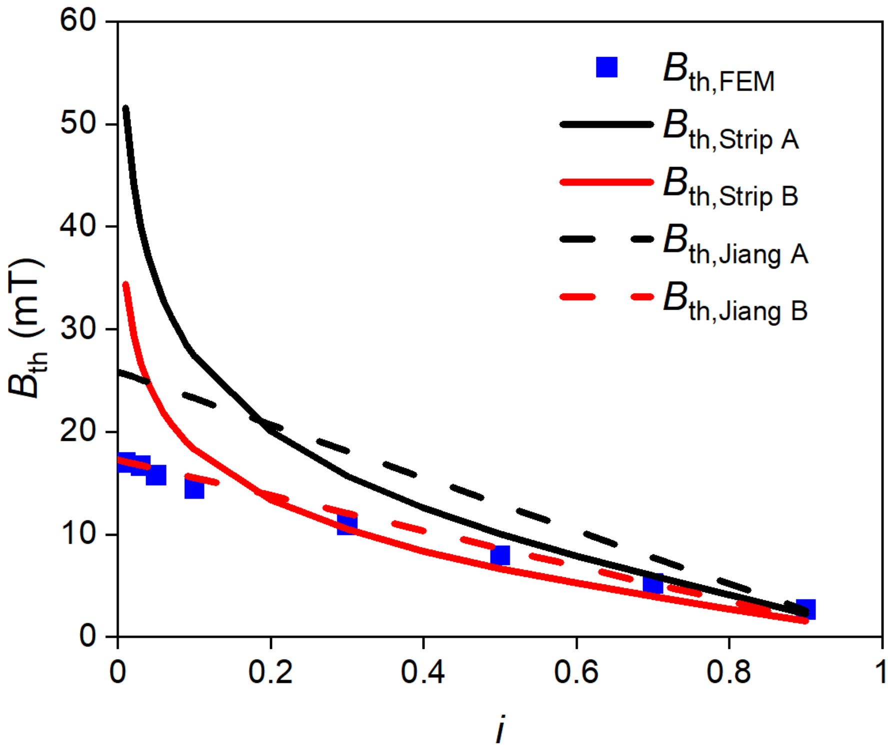

Figure 7.5: Threshold field values calculated using the FE model and the analytical equation for a single strip. Two strip models are presented. A strip with the same J_c and i values as the hollow strip. As well as a larger strip with a reduced J_c but the same i values.

2.16, a choice must be made for the values to use for the strip half-width, a. Two different possible choices for a correspond to (A) a strip with width equal to the sum of the two branches (ie $a = b = 4$ mm, $B_{\text{th,StripA}}$ and $B_{\text{th,JiangA}}$): or (B) a strip with total width equal to the total width of the hollow strip (ie $a = b+l = 6$ mm, $B_{\text{th,StripB}}$ and $B_{\text{th,JiangB}}$).

This results in four different calculations of B_{th} (two from equation 2.15 and two from equation 2.16), as summarised in table 7.1.

Figure 7.5 shows that analytical values calculated using $a = b$ ($B_{\mathrm{th,StripA}}$ and $B_{\mathrm{th,JiangA}}$) overestimate $B_{\mathrm{th,FEM}}$ for transport currents less than 90% of I_{c}. However, $B_{\mathrm{th,StripB}}$ and $B_{\mathrm{th,JiangB}}$ produce very good agreement with the FE values for B_{th}, particularly $B_{\mathrm{th,JiangB}}$ which is comparable for transport currents $0.01 \leq i \leq 0.9$. This is a rather surprising result as the derivation of neither equation 2.15 or 2.16 properly considers the current induced due to flux in the air gap. The non-linearity at low transport currents in the strip expression, equation 2.15, is not observed in the FE data which is linear over the full current range. Equation 2.16 exhibits this behaviour, with a threshold field value of 17 mT at the lowest transport current considered here. This agrees with the estimate of B_{pen} from figure 7.3.

7.2.2 DC Time-Averaged Electric Field

The derivation of equation 2.23 does consider the effect of the air gap on the time averaged electric field in a hollow slab. In the following section, values for E_{DC} calculated using the FE model and equation 2.23 are compared. This is shown in figure 7.6. $B_{\mathrm{th,JiangB}}$ is used as the threshold field input in equation 2.23, based on the close agreement observed in figure 7.5. Figure 7.6 reveals that three distinct regimes can be identified in the net DC electric fields.

1. Regime A - a zero net DC electric field regime exists wherever $B_{\mathrm{a0}} < B_{\mathrm{th}}$. This shielded regime is essentially identical to that observed in a monolithic strip, and includes all data points that lie along the i axis in figure 7.6. This regime is indicated by the cyan box.

2. Regime B - a non-zero net DC electric field regime exists where E_{DC} increases non-linearly with transport current. In this regime, $I_{\mathrm{t}} \ll I_{\mathrm{c}}$ and $B_{\mathrm{a0}} > B_{\mathrm{th}}$. This regime is defined by the deviation of the FE electric fields away from the linear behaviour predicted by equations 2.16 and 2.23.

3. Regime C - a non-zero net DC electric field regime exists where E_{DC} increases less rapidly than in Regime B and is broadly consistent with equation 2.23.

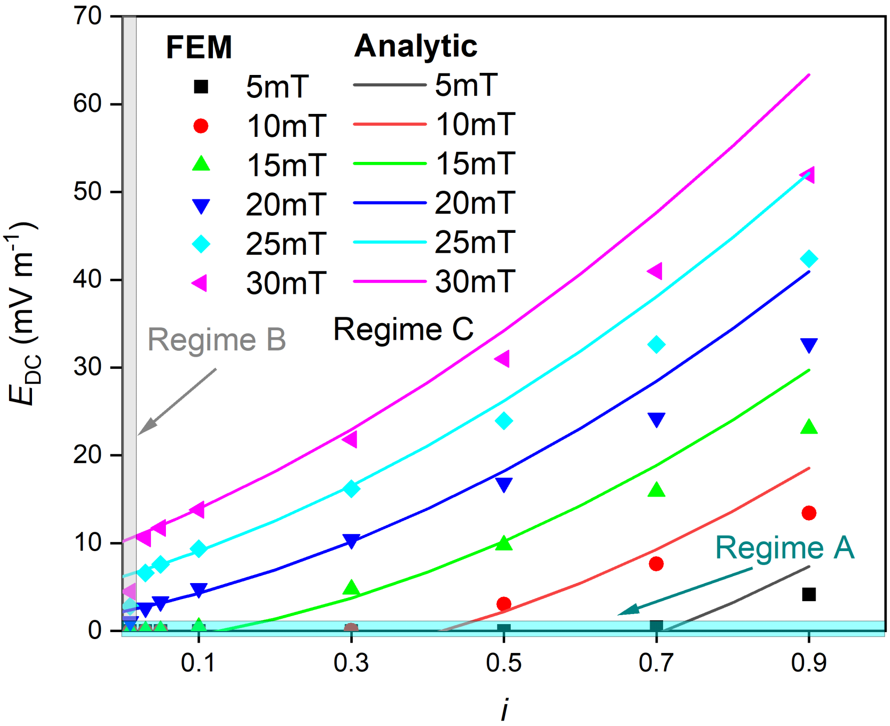

Figure 7.6: Calculated values for the net DC electric field from the FE model and using equation 2.23 and $B_{\mathrm{th,JiangB}}$ used as the threshold field

> In this regime, $I_t \geq 1\% I_c$ and $B_{a0} > B_{th}$. This regime represents all data points that lie outside of the grey and cyan boxes in figure 7.6.

Regime A is equivalent to that observed in the dynamic resistance of monolithic conductors. In this regime, the superconductor is not fully penetrated by the external field and the transport current is typically viewed as occupying the central region of the conductor. As the entire conductor is never saturated with critical currents, there is no net DC electric field. Regime C is also observed in monolithic strips. The combination of equations 2.16 and 2.23 for E_{DC} leads to an i^2 dependence, such that the dynamic resistance ($E_{DC}/\ i$) is expected to increase linearly. In this regime, during the AC field cycle the current density is driven above J_c everywhere such that flux traverses the strip and results in a net DC electric field. Regime B however, is not observed in monolithic conductors and represents a transition region that is only observed in hollow conductors.

7.2.3 Cyclic Evolution of Sheet Currents and Electromagnetic Fields

In order to analyse the three different regimes, the 2D data for J_z, B_y, and E_z from the FE model is transformed into the equivalent sheet values for using the relevant equations given in section 3.1.3. These are presented visually using contour plots (see figure 7.7). These contour plots are shown alongside time-evolution plots of the instantaneous values of E_{ave}, the net current in the left and right branches, I_L and, I_R, and B_{app}.

Regime A

Figure 7.7 shows the typical transient behaviour of sheet current values across the tape in regime A. Here $i = 0.5$, $B_{a0} = 5$ mT $< B_{th}$, and the time axis spans four cycles of the applied field. The current distributions are shown in plot (a). Return paths for induced screening currents (blue) are observed at the four tape edges, being largest at the outer two. Peak current penetration occurs concurrently with peaks in the applied magnetic field. Currents which run parallel to the transport current (red) penetrate further than those which run anti-parallel. Unlike the slab model, currents also penetrate each branch from the interior edges, although these are significantly smaller than those at the outer edges. In the centre of each HTS branch is a region where the currents run parallel with the transport current and are sub critical. This indicates that there is sufficient 'space' within each branch for the transport current to flow before 'overflowing' into regions occupied by screening currents. Plot (f) shows the local perpendicular magnetic flux density over the width of the loop and it is clear that the interior regions of each HTS branch have flux frozen in. The polarity is flipped between the two branches, and internal variations due to the external field occur primarily at the tape edges. Plot (k) shows that the largest magnitude electric fields are also generated

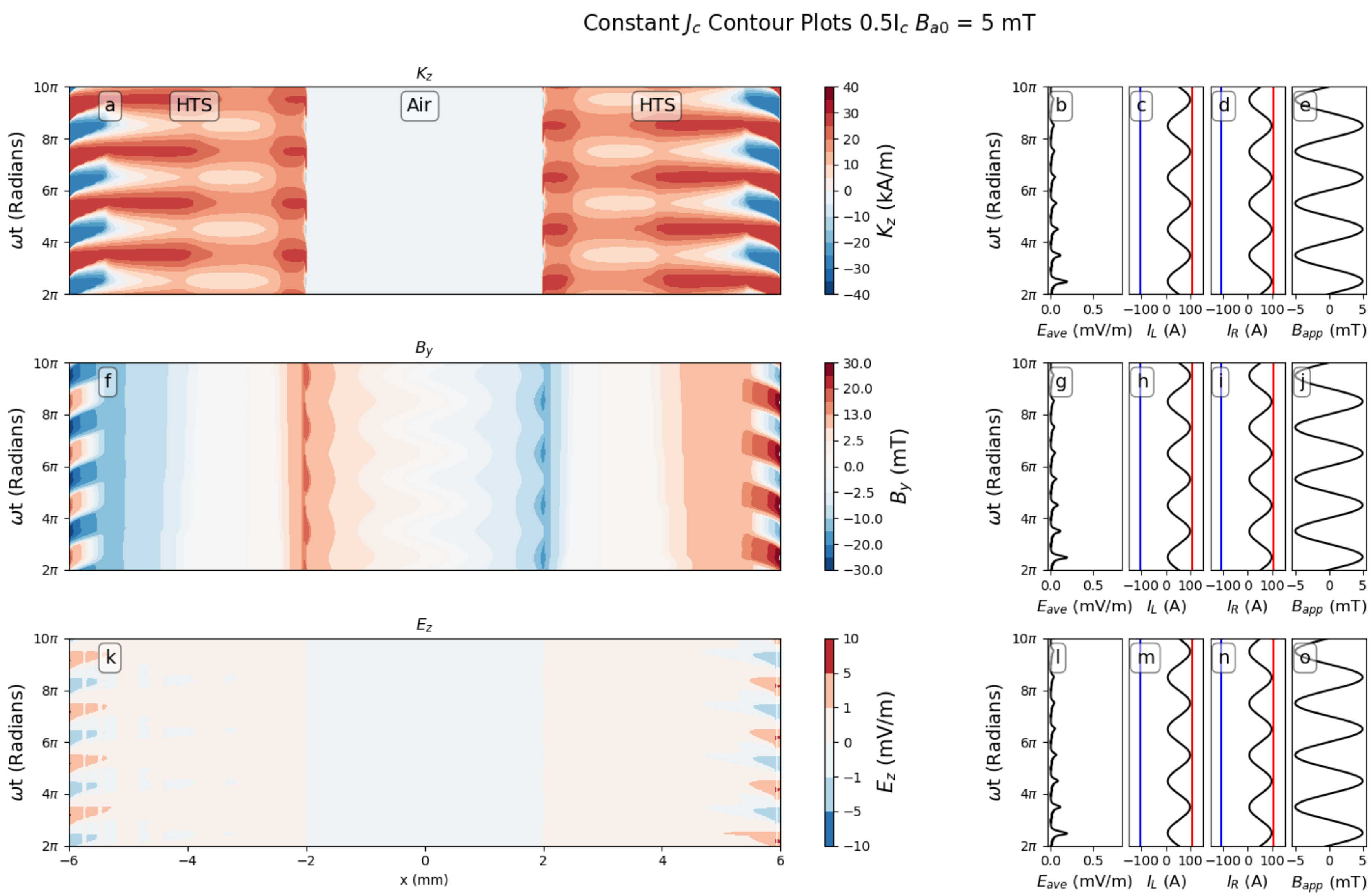

Figure 7.7: Regime A: Plots a,f, and k are contour plots showing the local evolution of K_z, B_y, and E_z over five cycles of the applied field. Plots b,c,d, and e show the E_{ave}, I_L, I_R and B_{app} waveforms. The remaining plots duplicate plots b-e alongside each contour plot so features can be correlated. The red and blue vertical lines indicate $\pm\ I_c$ in each branch. Here, $i = 0.5$, $B_{a0} = 5$ mT

at the outer edges of each branch and have opposite polarity. Because $B_{\mathrm{a0}} < B_{\mathrm{th}}$, the net electric field waveform is very small and the model does not produce a periodic waveform, even after four full cycles. However, as seen in figure 7.6, the DC time-averaged electric field is effectively zero for all cycles.

The behaviour in regime A can be understood in terms of the net transport current flowing through each branch as shown in plots (c) and (d). The transport current within each branch oscillates between zero and 95% of the branch I_{c}. Because neither branch exceeds $I_{\mathrm{c,branch}}$ at anytime, no flux traverses either branch and there is no net DC electric field.

Regime B

A set of typical contour plots for regime B are shown in figure 7.8 where $B_{\mathrm{a0}} > B_{\mathrm{th}}$ and $I_{\mathrm{t}} \ll I_{\mathrm{c}}$. In this particular instance, $i = 0.01$, $B_{a0} = 30$mT, and the time axis spans two cycles of the applied field.

Plot (a) again shows the current distributions within each branch and they have a particularly simple form. When B_{app} is at its peak, each branch contains only one polarity of current. As B_{app} varies by $2B_{\mathrm{th}}$ from its peak, the currents reverse polarity in both branches. Following this, the E_{ave} waveform increases from zero as the screening and transport currents interact.

This process is then mirrored in the following half cycle. In plot (f) we see the emergence of contour spikes at the internal edges of each branch, reminiscent of those for the single strip in chapter 5. These contour spikes represent the locations where the last bastion of frozen flux is eliminated once the applied field has varied by $2B_{\mathrm{th}}$ from the peak value.

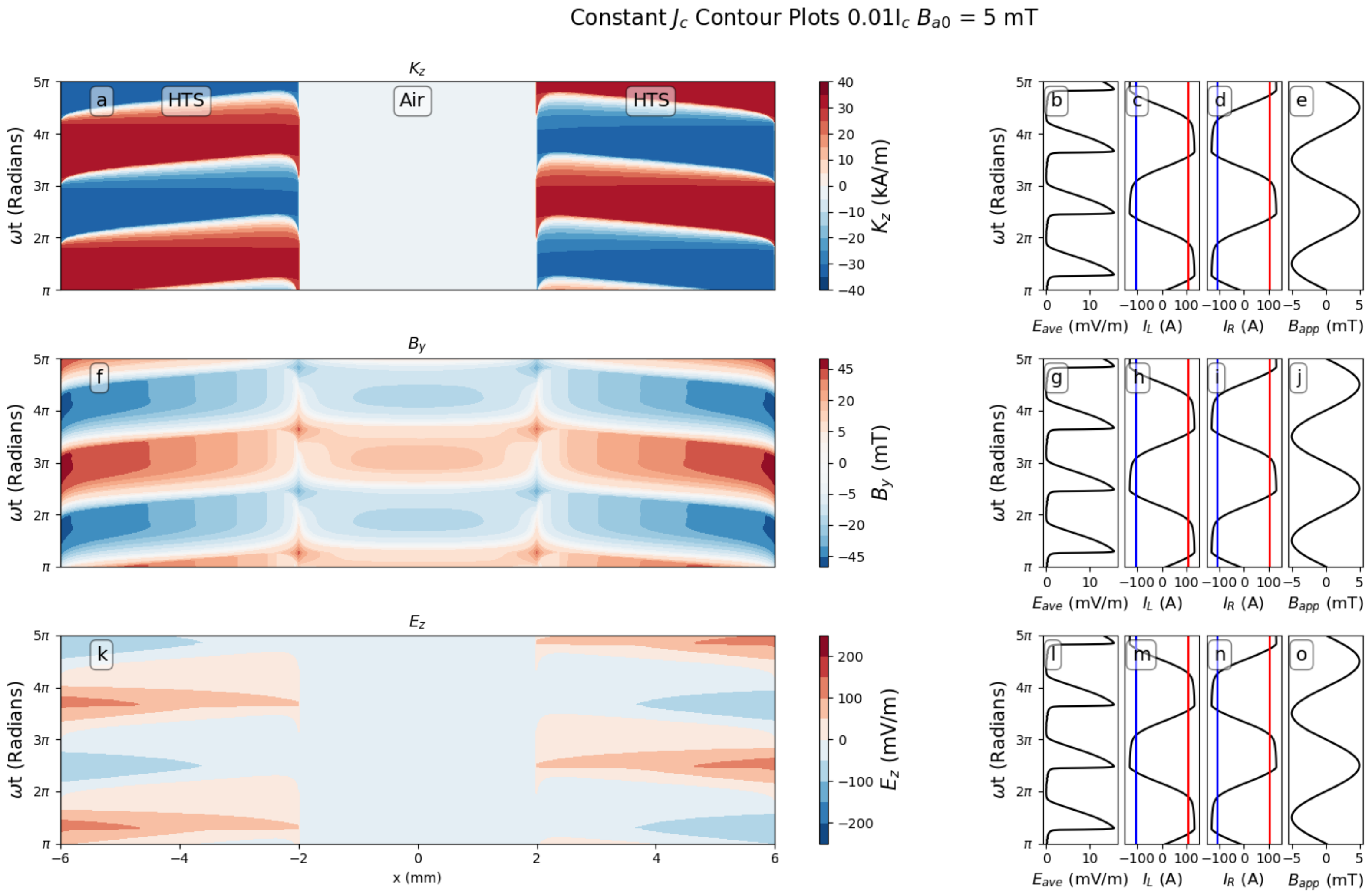

Figure 7.8: Regime B: Plots a,f, and k are contour plots showing the local periodic evolution of K_z, B_y, and E_z over two cycles of the applied field. Plots b,c,d, and e show the E_{ave}, I_L, I_R and B_{app} waveforms. The remaining plots duplicate plots b-e alongside each contour plot so features can be correlated. The red and blue vertical lines indicate $\pm\, I_c$ in each branch. Here, $i = 0.01$, $B_{a0} = 30$ mT

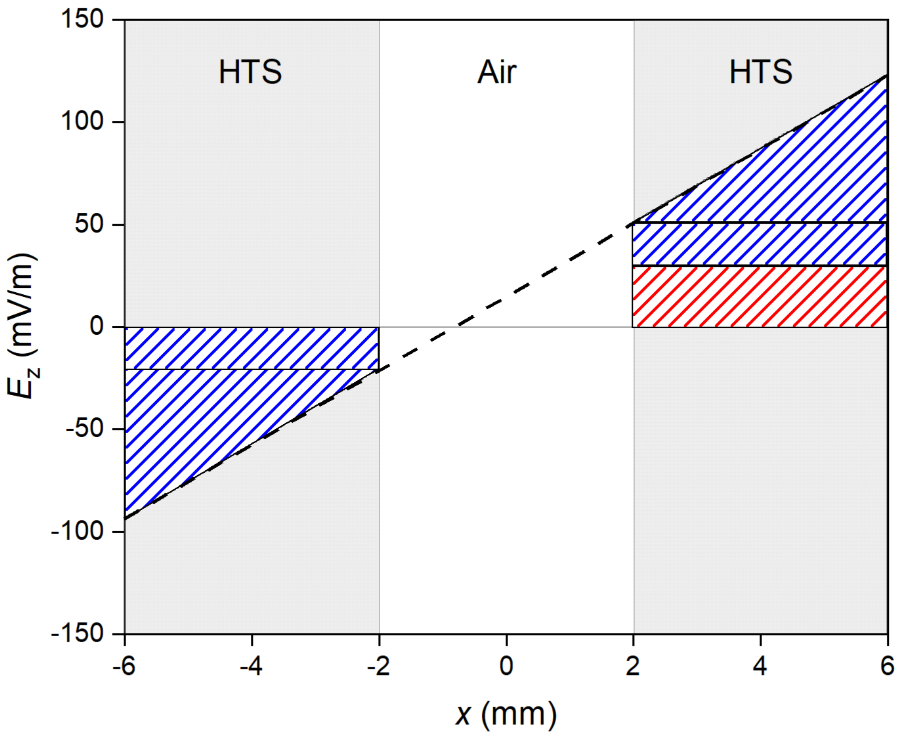

Figure 7.9: E_z profile across the conductor width at peak dissipation when $i = 0.01$, $B_{a0} = 30$ mT. The blue-shaded regions represent equal and opposite contributions to the spatially averaged electric field which sum to zero. The red-shaded area represents the net averaged electric field at this moment in the cycle.

From the contour plots, the field distributions appear to be symmetric about $x = 0$, as one would expect for a loop carrying no transport current. However, plot (k) demonstrates that the electric fields in the branch carrying current parallel to the transport current are significantly larger (as the current density is $> J_c$ throughout that branch). This asymmetry is what generates a net DC electric field. Plots (c) and (d) show the net current within each branch and we see that both are driven over $I_{c,\mathrm{branch}}$ at the same moments during the AC field cycle. The branch with screening currents running parallel to the transport current is driven further up the E-J curve, resulting in a larger electric field.

Figure 7.9 shows the electric field profile across the width of the conductor at peak dissipation as the applied field changes from negative to positive. The electric field varies linearly over the width when fully penetrated, similar to the strip models presented in chapter 5. This is because once both branches are saturated to J_c, the local magnetic field changes linearly with further applied field, ie independent of x-location. As a result, Faraday's law simplifies to $\partial_x E_z$ = constant. The presence of the net transport current in just one branch drives the electric field zero crossing away from the geometric centre of the loop. This is equivalent to stating that the electric field in the branch where the screening and transport currents are parallel has a larger electric field. The blue-shaded regions show contributions to the average E_z which are of equal and opposite polarity, and hence sum to zero. Cancelling the contributions from these regions leaves the residual DC electric field shown by the red-shaded region, which is distributed uniformly across the width of only one branch during each half cycle. Notably, the zero crossing of the electric field lies in the air gap between the two superconducting branches. This is the reason why equation 2.19 is not valid for regime B. The derivation of equation 2.19 requires a closed loop current path around the full loop for which $E = 0$ at all points. Finite element modelling shows that such a contour does not exist when operating in regime B.

Regime C

Contour plots for the typical transient evolution of sheet values in regime C are shown in figure 7.10 ($B_{a0} > B_{th}$ and $i > 0.01$). In this particular case, $i = 0.5$ and $B_{a0} = 30$ mT and the time axis spans two cycles of the applied field. The current distributions in plot (a) retain a relatively simple form. At the outer edge of each HTS branch, return paths for screening currents are clearly visible and these oscillate between the two branches with the applied field.

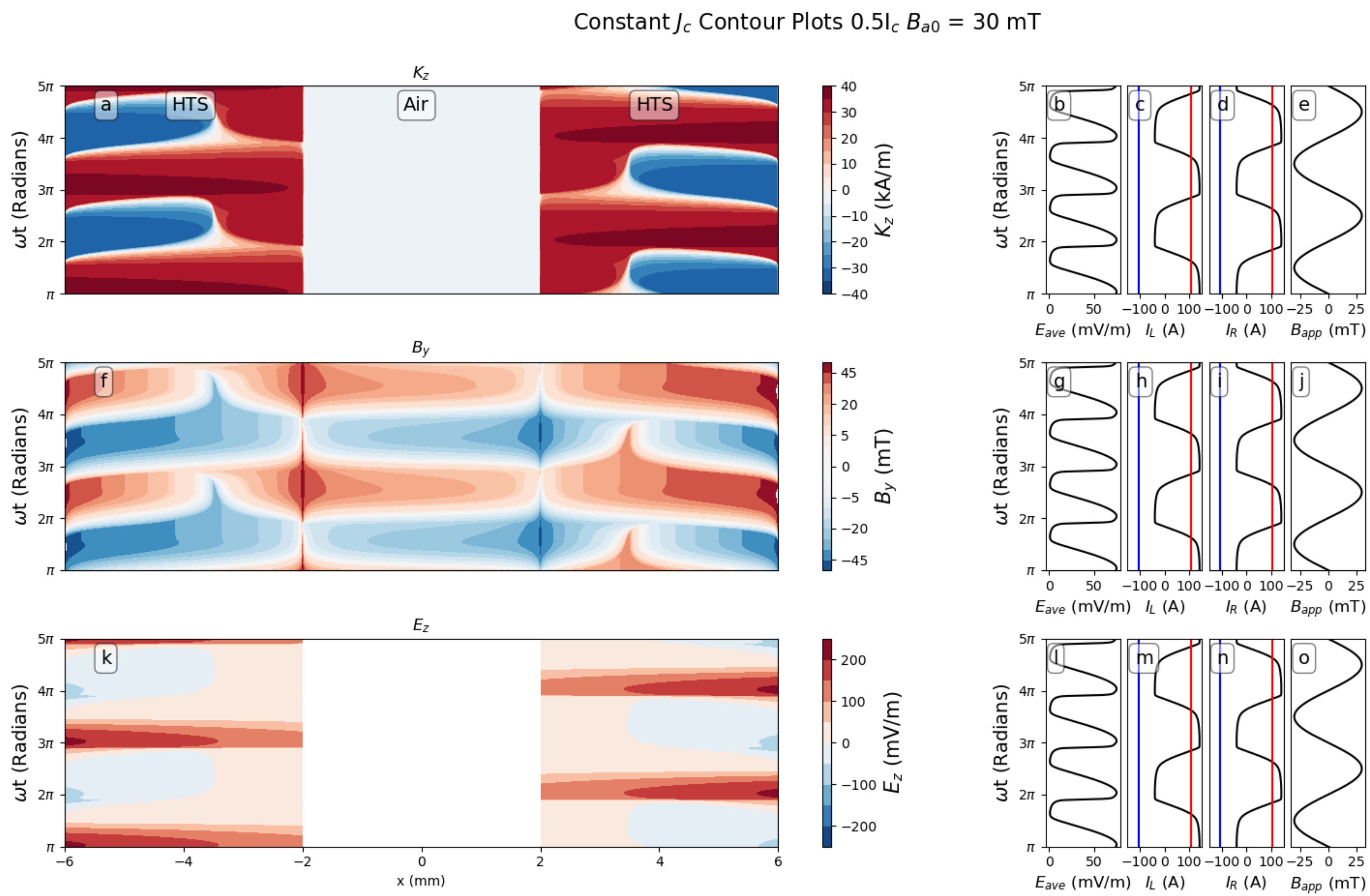

Figure 7.10: Regime C: Plots a,f, and k are contour plots showing the local periodic evolution of K_z, B_y, and E_z over two cycles of the applied field. Plots b,c,d, and e show the E_{ave}, I_L, I_R and B_{app} waveforms. The remaining plots duplicate plots b-e alongside each contour plot so features can be correlated. The red and blue vertical lines indicate $\pm\, I_c$ in each branch. Here, $i = 0.5$, $B_{a0} = 30$ mT

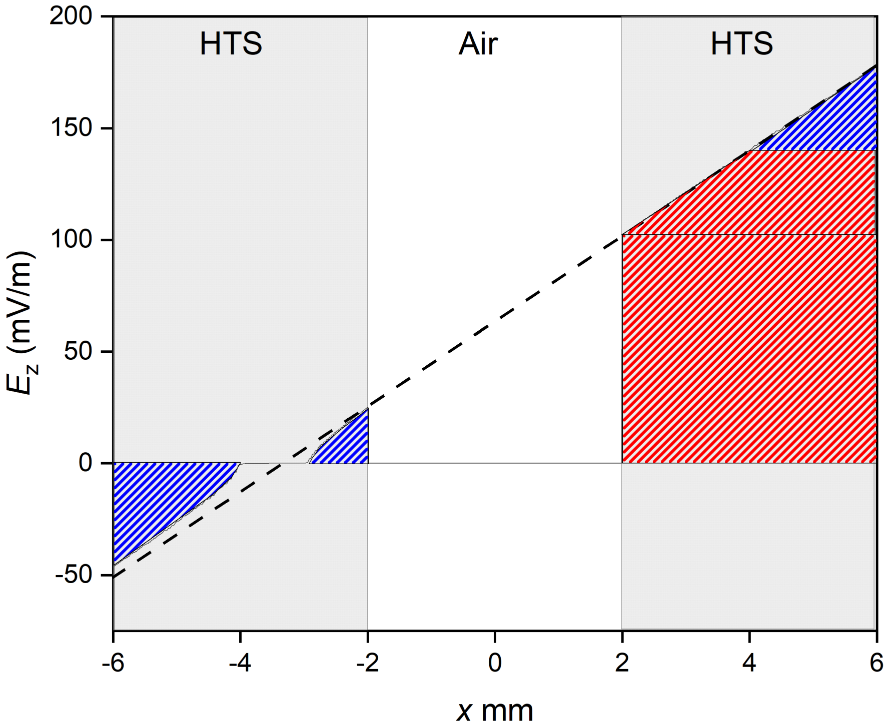

Figure 7.11: E_z profile across the conductor width at peak dissipation when $i = 0.5$, $B_{a0} = 30$ mT. The blue-shaded regions represent equal and opposite contributions to the spatially averaged electric field, which sum to zero. The red-shaded area represents the net averaged electric field at this moment in the cycle.

Once B_{app} varies by $2B_{th}$ from its peak value, the previous return paths for screening currents are completely erased and screening currents now occupy the alternate branch. After this point, E_{ave} increases rapidly from zero and remains positive until the following peak in B_{app}. Unlike regime B, only a single contour spike in B_y is apparent at any given moment. Plot (k) shows the local E_z. At peak resistance, a large electric field is generated in the branch with currents parallel to the transport current. It is largest at the outer edge and decreases linearly towards the inner edge. The other branch experiences significant electric fields of both polarities which partially cancel, resulting in an almost net zero electric field. Plots (c) and (d) show the net current within each branch. Unlike regime B, only one branch at a time carries a net transport current that exceeds $I_{c,branch}$ and this alternates with the applied field. The alternate branch essentially contains a large eddy current that acts to displace transport current from that particular branch.

Figure 7.11 shows the electric field profile across across the width of the hollow strip at peak resistance as the applied field changes from negative to positive. In the branch that is fully penetrated, again the electric field varies linearly with position. However, in the 'shielded branch' a non-linear trend in E_z is observed. Extrapolation of the linear electric field shows that the electric field zero crossing now lies within the shielded branch. This is different to regime B. Again, the blue-shaded regions represent equal and opposite contributions the net DC electric field represented by the red-shaded region. The largest electric fields are generated at the exterior edges of the loop. An exactly opposite distribution is observed at peak resistance in the next half-cycle. This means that the transport current moves between both branches over the course of a full cycle.

7.3 Summary Discussion

In this chapter, a finite element model has been used to predict the DC electric fields generated in a superconducting hollow strip that carries a transport current while exposed to an alternating, perpendicular magnetic field. From the model, time averaged electric and threshold magnetic fields have been calculated.

The time averaged electric fields exhibit three separate output regimes dependent on the applied transport current and AC field amplitude. Below the threshold field, both branches of the superconducting loop have regions of frozen flux. In this regime (A), the FE model does not produce an equilibrium solution after four cycles of the applied field, however the magnitude of the time-averaged electric fields are insignificant when compared with the other two regimes. The two non-zero regimes are differentiated by the amount of transport current flowing through the superconductor. Consider a superconducting hollow strip exposed to an alternating magnetic field with no transport current. If the field is sufficient to fully penetrate each of the superconducting branches, equal and opposite electric fields are driven in each branch. The electric field can be imagined to cross zero at the geometric centre of the loop. As the transport current is increased from zero, the electric centre line is now slightly displaced, oscillating about the geometric centre of the loop. Provided the transport current is sufficiently small, the electric centre line remains in the air gap and the device is in the second regime (B). This second regime is not observed in the dynamic resistance of geometries consisting of a single piece of superconductor and is exclusive to the 'hollow loop' geometry. At peak dissipation in this regime, each branch contains currents of the same polarity. The branch carrying transport current is driven further up the E-J curve, generating a larger electric field. As the transport current increases, the electric centre line is further displaced and now oscillates between the two branches. Peak dissipation in this regime (C) occurs in one branch at a time, and evolves similarly to the dynamic resistance of a single bulk conductor with increasing transport current.

8
Conclusions

In this thesis, a combination of finite element simulations and experiments have been used to investigate two resistive phenomena in high temperature superconductor wire; geometric current saturation, and dynamic resistance. Both phenomena have been modelled using the $\boldsymbol{H}$-formulation, employing a magnetic field dependent power-law function to capture the electrical properties of the superconductor and validated against experimental data. The models allow one to interrogate the electromagnetic fields and current distributions within the conductor. This allows for interpretation of these phenomena in the language of conventional 'flux physics'. This analysis has provided a number of novel results and insights which are summarised in the following.

Geometric Current Saturation

- Current saturation across the conductor width in high aspect-ratio HTS tapes (crystalline and multi-filamentary) during transport measurements can be observed using near surface magnetic field imaging. Prior to saturation, current initially occupies the edge regions, filling towards the centre with increasing transport current. After saturation, additional transport current is distributed uniformly over the entire conductor cross-section.

- This non-uniform filling behaviour causes a change in the near-surface magnetic field signature from non-linear to linear. This signature change can be used to reliably identify the saturation current of a HTS thin film, independent of sensor location and at a singular value for the transport current.

- The experimentally observed voltage response in HTS conductors and near surface magnetic field behaviour during transport measurements can be fully reproduced using finite element models using solely Maxwell's laws with a power-law resistivity. This means that it is not necessary to invoke more complex quantum physics to describe this behaviour, as has been proposed in [106–108]

- Finite element modelling results indicate that current saturation coincides with the penetrating flux front reaching the tape centre and the onset of steady flux flow across the entire conductor width.

- The saturation current is shown to vary as a function of the current ramp rate. This results in variations in the apparent J_c.

- The critical current of a HTS tape is typically considered to be a fixed quantity for a given magnetic field, determined using an arbitrary electric field criterion of 1 μV cm^{-1}. This definition is inherently unsatisfying as the 1 μV cm^{-1} criterion can occur in both the flux-creep and flux-flow regimes, depending on the experimental conditions.

- The saturation current is proposed as an alternative definition for the critical current. Unlike the voltage criterion, the saturation current is a phenomenological definition that is equivalent to the theoretical definition of the critical current given in the Bean model in terms or current and flux penetration.

Dynamic Resistance in Tapes and Stacks

- Finite element models employing a power-law resistivity with field dependent J_c, reproduce the experimental transient voltage response in HTS tapes exhibiting dynamic resistance. Constant J_c models *do not* capture all of the physics exhibited in experimental results.

- Available analytical models describe dynamic resistance in terms of a net transfer of a single polarity flux across the conductor width when an AC field is applied on top of a DC background field. Finite element models confirm that in the absence of a DC background field, flux of both polarities enters at both tape edges. This results in vortex anti-vortex annihilation occurring across the entire conductor width. This has an equivalent effect of generating a DC electric field, each cycle of the applied field.

- There are experimentally observed features which *cannot be described* using the Bean critical state model with a constant J_c but which are fully reproduced using a finite element model with a field dependent J_c. In the absence of a field dependent critical current, the maximum voltage response is expected to occur at the zero-crossing of the applied magnetic field (where its time rate of change is largest). Inclusion of field dependent J_c results in a short lived increase in the current carrying capacity of the wire which results in peak-splitting of the measured voltage waveform.

- The contour plots presented in this thesis are a powerful tool for investigating the transient evolution of sheet variables in HTS coated conductors. This visualisation technique can be applied to any superconductor where transient behaviour is of note and the conductor cross-section can be treated as 1-dimensional.

- The electric field distributions calculated using a finite element model indicate that the transport currents flows across the entire width of the conductor over a cycle of the applied field. This is in contrast with analytical models which assume the transport currents flow in the tape centre.

- The threshold fields for vertical stacks of HTS tapes with varying aspect ratios have been calculated using a finite element model. In the high(low) aspect ratio limits, the strip(slab) equations agree with the calculated values. At intermediate aspect ratios, the calculated threshold fields transition between these two limiting cases.

Dynamic Resistance in a Hollow Strip

- The effective resistance generated in a hollow superconducting strip has been calculated and is significantly larger when compared with monolithic conductors carrying similar transport currents and in similar external fields. This makes hollow-conductor geometries promising for superconducting switching elements.

- The effective resistance in a current carrying, hollow superconducting strip in an alternating perpendicular magnetic field has been computed using the a finite element model with a power-law resistivity. Three different output regimes have been identified. Two regimes are analogous to the dynamic resistance behaviour observed in monolithic conductors, but the other regime is unique to hollow-conductor geometries.

- As with the case for dynamic resistance in monolithic conductors, the effective resistance is generated by flux motion across the conductor. The exact flux dynamics vary depending on which regime the hollow conductor is in.

Future Work

This analyses presented in this thesis leads to a number of interesting results which can provoke consideration of potential future research. These are outlined in the following.

Geometric current saturation

- The work concerning the saturation current has been presented only for single tapes. This work can be extended to examine current saturation in all manner of superconductor cables and coils with saturation correlated with features in the measured I-V characteristics. This will be possible provided the configuration exhibits an aspect ratio $\gg 1$.

- The finite element models considered in this thesis all employ a power-law resistivity. This means that provided $\mathrm{d}I_\mathrm{t}/\mathrm{d}t$ is sufficiently slow, then $I_\mathrm{c,S}$ can be driven arbitrarily close to zero. Reality might differ markedly from this where materials have non-zero pinning forces and thus current saturation over the width at low currents should be impossible. Further experimental tests may assist in determining whether this is the case for commercial HTS tapes.

Dynamic resistance

- Finite element analysis of dynamic resistance in HTS tapes and cables in a combination of DC and AC magnetic fields can be performed. This could then be compared with experimental data such as that published in [67, 68].

- Additional modelling of dynamic resistance in parallel connected, vertical stacks could be performed with $J_\mathrm{c}(B,\theta)$ data obtained in higher fields should be performed. The $J_\mathrm{c}(B,\theta)$ data would allow for a complete mapping of the transition between strip and slab behaviour.

- The finite element analysis of dynamic resistance in hollow-strip geometries must be validated against experimental data obtained on hollow-strip conductors. Commercial HTS tapes can be etched and tested in a dynamic resistance setup such as that described in this thesis. An analytical expression for the threshold field in hollow-conductor geometries can be derived making the usual Bean critical state assumptions and using the conformal mapping technique outlined in [38–40]

References

[1] J. G. Bednorz and K. A. Müller. "Possible high T_c superconductivity in the Ba-La- Cu- O system". In: *Zeitschrift für Physik B Condensed Matter* 64.2 (1986), pp. 189–193.

[2] L. Bromberg, M. Tekula, L. El-Guebaly, R Miller, A. Team, et al. "Options for the use of high temperature superconductor in tokamak fusion reactor designs". In: *Fusion Engineering and Design* 54.2 (2001), pp. 167–180.

[3] P. Bruzzone, W. H. Fietz, J. V. Minervini, M. Novikov, N. Yanagi, Y. Zhai, and J. Zheng. "High temperature superconductors for fusion magnets". In: *Nuclear Fusion* 58.10 (2018), p. 103001.

[4] C. Barth. *High temperature superconductor cable concepts for fusion magnets.* Vol. 7. KIT Scientific Publishing, 2013.

[5] D. Whyte, J Minervini, B LaBombard, E Marmar, L Bromberg, and M Greenwald. "Smaller & sooner: Exploiting high magnetic fields from new superconductors for a more attractive fusion energy development path". In: *Journal of Fusion Energy* 35.1 (2016), pp. 41–53.

[6] R Heller, W. Fietz, A Kienzler, and R Lietzow. "High temperature superconductor current leads for fusion machines". In: *Fusion engineering and design* 86.6-8 (2011), pp. 1422–1426.

[7] Y. Iwasa. "HTS and NMR/MRI magnets: Unique features, opportunities, and challenges". In: *Physica C: Superconductivity and its applications* 445 (2006), pp. 1088–1094.

[8] C. A. Luongo, P. J. Masson, T. Nam, D. Mavris, H. D. Kim, G. V. Brown, M. Waters, and D. Hall. "Next generation more-electric aircraft: A potential application for HTS superconductors". In: *IEEE Transactions on Applied Superconductivity* 19.3 (2009).

[9] P. J. Masson and C. A. Luongo. "High power density superconducting motor for all-electric aircraft propulsion". In: *IEEE Transactions on Applied Superconductivity* 15.2 (2005).

[10] A. Patel, V. Climente-Alarcon, A. Baskys, B. A. Glowacki, and T. Reis. "Design considerations for fully superconducting synchronous motors aimed at future electric aircraft". In: *2018 IEEE International Conference on Electrical Systems for Aircraft, Railway, Ship Propulsion and Road Vehicles & International Transportation Electrification Conference (ESARS-ITEC)*. IEEE. 2018.

[11] J. H. Durrell, M. D. Ainslie, D. Zhou, P. Vanderbemden, T. Bradshaw, S. Speller, M. Filipenko, and D. A. Cardwell. "Bulk superconductors: a roadmap to applications". In: *Superconductor Science and Technology* 31.10 (2018), p. 103501.

[12] K. S. Haran, S. Kalsi, T. Arndt, H. Karmaker, R. Badcock, B. Buckley, T. Haugan, M. Izumi, D. Loder, J. W. Bray, et al. "High power density superconducting rotating machines—development status and technology roadmap". In: *Superconductor Science and Technology* 30.12 (2017), p. 123002.

[13] L. Van de Klundert and H. H. ten Kate. "Fully superconducting rectifiers and fluxpumps Part 1: Realized methods for pumping flux". In: *Cryogenics* 21.4 (1981), pp. 195–206.

[14] M. Ainslie, F. Grilli, L. Quéval, E. Pardo, F. Perez-Mendez, R. Mataira, A. Morandi, A. Ghabeli, C. Bumby, and R. Brambilla. "A new benchmark problem for electromagnetic modelling of superconductors: the high-T_c superconducting dynamo". In: *Superconductor Science and Technology* 33.10 (2020), p. 105009.

[15] R. Mataira, M. Ainslie, A. Pantoja, R. Badcock, and C. Bumby. "Mechanism of the high-T c superconducting dynamo: Models and experiment". In: *Physical Review Applied* 14.2 (2020), p. 024012.

[16] R. Mataira, M. Ainslie, R. Badcock, and C. Bumby. "Origin of the DC output voltage from a high-Tc superconducting dynamo". In: *Applied Physics Letters* 114.16 (2019), p. 162601.

[17] K. Hamilton, A. E. Pantoja, J. G. Storey, Z. Jiang, R. A. Badcock, and C. W. Bumby. "Design and performance of a "squirrel-cage" dynamo-type HTS flux pump". In: *IEEE Transactions on Applied Superconductivity* 28.4 (2018).

[18] C. Bumby, Z. Jiang, J. Storey, A. Pantoja, and R. Badcock. "Anomalous open-circuit voltage from a high-T c superconducting dynamo". In: *Applied Physics Letters* 108.12 (2016), p. 122601.

[19] T. A. Coombs, J. Geng, L Fu, and K Matsuda. "An overview of flux pumps for HTS coils". In: *IEEE Transactions on Applied Superconductivity* 27.4 (2016).

[20] J. Geng and T. Coombs. "Mechanism of a high-T_c superconducting flux pump: Using alternating magnetic field to trigger flux flow". In: *Applied Physics Letters* 107.14 (2015), p. 142601.

[21] A Sundaram, Y Zhang, A. Knoll, D Abraimov, P Brownsey, M Kasahara, G. Carota, R Nakasaki, J. Cameron, G Schwab, et al. "2G HTS wires made on 30 μm thick Hastelloy substrate". In: *Superconductor Science and Technology* 29.10 (2016), p. 104007.

[22] J.-H. Lee, H. Lee, J.-W. Lee, S.-M. Choi, S.-I. Yoo, and S.-H. Moon. "RCE-DR, a novel process for coated conductor fabrication with high performance". In: *Superconductor Science and Technology* 27.4 (2014), p. 044018.

[23] H. Yi, Z Han, J. Zhang, T Liu, L Liu, M. Li, J Fang, Q Liu, and Y. Zheng. "Research status of the manufacturing technology and application properties of Bi-2223/Ag tapes at Innost". In: *Physica C: Superconductivity* 412 (2004), pp. 1073–1078.

[24] *2G HTS Wire Specification SuperPower.* `https://www.superpower-inc.com/specification.aspx`. (undefined 29/9/2021 15:6).

[25] H. Kamerlingh Onnes. "The superconductivity of mercury". In: *Comm. Phys. Lab. Univ. Leiden* 122 (1911), pp. 122–124.

[26] W. Meissner and R. Ochsenfeld. "Ein neuer effekt bei eintritt der supraleitfähigkeit". In: *Naturwissenschaften* 21.44 (1933), pp. 787–788.

[27] A. A. Abrikosov. "The magnetic properties of superconducting alloys". In: *Journal of Physics and Chemistry of Solids* 2.3 (1957), pp. 199–208.

[28] V. A. Shklovskij and O. V. Dobrovolskiy. “AC-driven vortices and the Hall effect in a superconductor with a tilted washboard pinning potential”. In: *Physical Review B* 78.10 (2008), p. 104526.

[29] J. Bardeen and M. Stephen. “Theory of the motion of vortices in superconductors”. In: *Physical Review* 140.4A (1965), A1197.

[30] N. Strickland, N. Long, E. Talantsev, P Hoefakker, J Xia, M. Rupich, T Kodenkandath, W Zhang, X Li, and Y Huang. “Enhanced flux pinning by BaZrO3 nanoparticles in metal-organic deposited YBCO second-generation HTS wire”. In: *Physica C: Superconductivity* 468.3 (2008), pp. 183–189.

[31] N. Strickland, N. Long, E. Talantsev, P Hoefakker, J. Xia, M. Rupich, W Zhang, X Li, T Kodenkandath, and Y Huang. “Nanoparticle additions for enhanced flux pinning in YBCO HTS films”. In: *Current Applied Physics* 8.3-4 (2008), pp. 372–375.

[32] N. Strickland, S. Wimbush, J. Kennedy, M. Ridgway, E. Talantsev, and N. Long. “Effective low-temperature flux pinning by Au ion irradiation in HTS coated conductors”. In: *IEEE Transactions on Applied Superconductivity* 25.3 (2014).

[33] F Lera, R Navarro, C Rillo, L. Angurel, A Badia, and J Bartolomé. “Critical state models for inter and intragranular flux pinning in HTS ceramics: universal scaling laws”. In: *Journal of Magnetism and Magnetic Materials* 104 (1992), pp. 615–616.

[34] C. P. Bean. “Magnetization of hard superconductors”. In: *Physical review letters* 8.6 (1962), p. 250.

[35] C. P. Bean. “Magnetization of high-field superconductors”. In: *Reviews of modern physics* 36.1 (1964), p. 31.

[36] P. W. Anderson. “Theory of flux creep in hard superconductors”. In: *Physical Review Letters* 9.7 (1962), p. 309.

[37] Y. Kim, C. Hempstead, and A. Strnad. “Critical persistent currents in hard superconductors”. In: *Physical Review Letters* 9.7 (1962), p. 306.

[38] W. Norris. “Calculation of hysteresis losses in hard superconductors carrying AC: isolated conductors and edges of thin sheets”. In: *Journal of Physics D: Applied Physics* 3.4 (1970), p. 489.

[39] E. Brandt, M. Indenbom, and A Forkl. “Type-II superconducting strip in perpendicular magnetic field”. In: *EPL (Europhysics Letters)* 22.9 (1993), p. 735.

[40] E Zeldov, J. R. Clem, M McElfresh, and M Darwin. “Magnetization and transport currents in thin superconducting films”. In: *Physical Review B* 49.14 (1994), p. 9802.

[41] E. H. Brandt. “Superconductors of finite thickness in a perpendicular magnetic field: Strips and slabs”. In: *Physical review B* 54.6 (1996), p. 4246.

[42] J. Rhyner. “Magnetic properties and AC-losses of superconductors with power law current—voltage characteristics”. In: *Physica C: Superconductivity* 212.3-4 (1993), pp. 292–300.

[43] S. C. Wimbush and N. M. Strickland. “A public database of high-temperature-superconductor critical current data”. In: *IEEE Transactions on Applied Superconductivity* 27.4 (2016).

[44] Y. Kim, C. Hempstead, and A. Strnad. "Magnetization and critical supercurrents". In: *Physical Review* 129.2 (1963), p. 528.

[45] T. Johansen and H Bratsberg. "Critical-state magnetization of type-II superconductors in rectangular slab and cylinder geometries". In: *Journal of Applied Physics* 77.8 (1995), pp. 3945–3952.

[46] M. R. Koblischka, A. Van Dalen, T Higuchi, S. Yoo, and M. Murakami. "Analysis of pinning in $NdBa_2Cu_3O_{7-\delta}$ superconductors". In: *Physical Review B* 58.5 (1998), p. 2863.

[47] S Furtner, R Nemetschek, R Semerad, G Sigl, and W Prusseit. "Reel-to-reel critical current measurement of coated conductors". In: *Superconductor Science and Technology* 17.5 (2004), S281.

[48] K. Higashikawa, K. Katahira, M. Inoue, T. Kiss, Y. Shingai, M. Konishi, K. Ohmatsu, T. Machi, M. Yoshizumi, T. Izumi, et al. "Nondestructive diagnostics of narrow coated conductors for electric power applications". In: *IEEE Transactions on Applied Superconductivity* 24.3 (2013).

[49] T. Machi, N. Chikumoto, K. Nakao, Y. Aoki, Y. Kitoh, H. Fuji, T. Izumi, A. Ibi, and Y. Yamada. "Development of a magneto-optical imaging equipment for long length 2G-HTS tapes". In: *Physica C: Superconductivity and its applications* 445 (2006), pp. 673–676.

[50] H. Song, M. W. Davidson, and J. Schwartz. "Dynamic magneto-optical imaging of transport current redistribution and normal zone propagation in $\mathrm{YBa}_2Cu_3O_{7-}\delta$ coated conductor". In: *Superconductor Science and Technology* 22.6 (2009), p. 062001.

[51] T. Johansen, M Baziljevich, H Bratsberg, Y Galperin, P. Lindelof, Y Shen, and P Vase. "Direct observation of the current distribution in thin superconducting strips using magneto-optic imaging". In: *Physical Review B* 54.22 (1996), p. 16264.

[52] V. Andrianov, V. Zenkevich, V. Kurguzov, V. Sytchev, and F. Ternovskii. "Effective resistance of an imperfect type-II superconductor in an oscillating magnetic field". In: *Zh. Eksp. Teor. Fiz.;(USSR)* 58 (1970).

[53] T Ogasawara, K Yasuköchi, S Nose, and H Sekizawa. "Effective resistance of current-carrying superconducting wire in oscillating magnetic fields 1: Single core composite conductor". In: *Cryogenics* 16.1 (1976), pp. 33–38.

[54] T Ogasawara, Y Takahashi, K Kanbara, Y Kubota, K Yasohama, and K Yasukochi. "Alternating field losses in superconducting wires carrying dc transport currents: Part 1 single core conductors". In: *Cryogenics* 19.12 (1979), pp. 736–740.

[55] M. Aikele, R. Huebener, D Weischer, and C. Tsuei. "Effect of high-frequency magnetic fields on the dissipative vortex motion in the superconducting mixed state". In: *Physica C: Superconductivity* 290.1-2 (1997), pp. 109–112.

[56] M. Oomen, J Rieger, M Leghissa, B. ten Haken, and H. H. ten Kate. "Dynamic resistance in a slab-like superconductor with J_c(B) dependence". In: *Superconductor Science and Technology* 12.6 (1999), p. 382.

[57] T Ogasawara, K Yasukōchi, and S Sayama. “Effective resistance of current-carrying superconducting wire in oscillating magnetic fields 2. Twisted multifilamentary composite conductor”. In: *Cryogenics* 16.2 (1976), pp. 89–96.

[58] G. P. Mikitik and E. H. Brandt. “Generation of a DC voltage by an AC magnetic field in type-II superconductors”. In: *Physical Review B* 64.9 (2001), p. 092502.

[59] E. H. Brandt and G. P. Mikitik. “Why an ac magnetic field shifts the irreversibility line in type-II superconductors”. In: *Physical review letters* 89.2 (2002), p. 027002.

[60] M. Risse, M. Aikele, S. Doettinger, R. Huebener, C. Tsuei, and M Naito. “Dissipation in the superconducting mixed state in the presence of a small oscillatory magnetic-field component”. In: *Physical Review B* 55.22 (1997), p. 15191.

[61] Z. Jiang, R. Toyomoto, N. Amemiya, X. Zhang, and C. W. Bumby. “Dynamic resistance of a high-T_c coated conductor wire in a perpendicular magnetic field at 77 K”. In: *Superconductor Science and Technology* 30.3 (2017), 03LT01.

[62] H. Zhang, M. Yao, Z. Jiang, Y. Xin, and Q. Li. “Dependence of dynamic loss on critical current and n-value of HTS coated conductors”. In: *IEEE Transactions on Applied Superconductivity* 29.8 (2019).

[63] H. Zhang, H. Chen, Z. Jiang, T. Yang, Y. Xin, M. Mueller, and Q. Li. “A full-range formulation for dynamic loss of high-temperature superconductor coated conductors”. In: *Superconductor Science and Technology* 33.5 (2020), 05LT01.

[64] F. Grilli. “Calculating the full-range dynamic loss of HTS wires in an instant”. In: *Superconductor Science and Technology* 34.2 (2021), p. 020501.

[65] M Ciszek, H. Knoopers, J. Rabbers, B. ten Haken, and H. H. ten Kate. “Angular dependence of the dynamic resistance and its relation to the AC transport current loss in Bi-2223/Ag tape superconductors”. In: *Superconductor Science and Technology* 15.8 (2002), p. 1275.

[66] M. Ciszek, O Tsukamoto, J Ogawa, and D Miyagi. “Energy losses in YBCO-123 coated conductors carrying transport current in perpendicular external magnetic field”. In: *AIP Conference Proceedings*. Vol. 614. 1. American Institute of Physics. 2002, pp. 606–613.

[67] R. C. Duckworth, Y. F. Zhang, T. Ha, and M. J. Gouge. “Dynamic resistance of YBCO-coated conductors in applied AC fields with DC transport currents and DC background fields”. In: *IEEE Transactions on Applied Superconductivity* 21.3 (2010).

[68] A Uksusman, Y Wolfus, A Friedman, A Shaulov, and Y Yeshurun. “Voltage response of current carrying YBaCuO tapes to alternating magnetic fields”. In: *Journal of Applied Physics* 105.9 (2009), p. 093921.

[69] Z. Jiang, K Hamilton, N. Amemiya, R. Badcock, and C. Bumby. “Dynamic resistance of a high-T_c superconducting flux pump”. In: *Applied Physics Letters* 105.11 (2014), p. 112601.

[70] Z. Jiang, R. Toyomoto, N. Amemiya, C. W. Bumby, R. A. Badcock, and N. J. Long. “Dynamic resistance measurements in a GdBCO-coated conductor”. In: *IEEE Transactions on Applied Superconductivity* 27.4 (2016).

[71] Z. Jiang, W Zhou, C. Bumby, M Staines, Q Li, R. Badcock, N. Long, and J Fang. "Dynamic resistance measurement of a four-tape YBCO stack in a perpendicular magnetic field". In: *IEEE Transactions on Applied Superconductivity* 28.4 (2017).

[72] Y. Liu, Z. Jiang, Q. Li, C. W. Bumby, R. A. Badcock, and J. Fang. "Dynamic resistance measurement in a four-tape YBCO stack with various applied field orientation". In: *IEEE Transactions on Applied Superconductivity* 29.5 (2019).

[73] C. Li, J. Geng, J. Yang, J. Gawith, B. Shen, J. Ma, and T. Coombs. "Second harmonic in the voltage of dc-carrying YBCO tape under a perpendicular alternating magnetic field". In: *Physica C: Superconductivity and its Applications* 564 (2019), pp. 11–16.

[74] V. Lahtinen, E. Pardo, J. Šouc, M. Solovyov, and A. Stenvall. "Ripple field losses in direct current biased superconductors: Simulations and comparison with measurements". In: *Journal of Applied Physics* 115.11 (2014), p. 113907.

[75] J. Ma, J. Geng, W. K. Chan, J. Schwartz, and T. Coombs. "A temperature-dependent multilayer model for direct current carrying HTS coated-conductors under perpendicular AC magnetic fields". In: *Superconductor Science and Technology* 33.4 (2020), p. 045007.

[76] J. Brooks, M. Ainslie, Z. Jiang, A. Pantoja, R. Badcock, and C. Bumby. "The transient voltage response of ReBCO coated conductors exhibiting dynamic resistance". In: *Superconductor Science and Technology* 33.3 (2020), p. 035007.

[77] Z. Zhong, W. Wu, and Z. Jin. "Sharp demagnetization of closed-loop HTS coil in first cycle of external AC fields induced by unexpected dynamic resistance". In: *Superconductor Science and Technology* 34.8 (2021), 08LT01.

[78] Y. Sun, J. Fang, G. Sidorov, Q. Li, R. A. Badcock, N. J. Long, and Z. Jiang. "Total loss measurement and simulation in a REBCO coated conductor carrying DC current in perpendicular AC magnetic field at various temperatures". In: *Superconductor Science and Technology* 34.6 (2021), p. 065009.

[79] J. M. Brooks, M. D. Ainslie, Z. Jiang, S. C. Wimbush, R. A. Badcock, and C. W. Bumby. "Numerical modelling of dynamic resistance in a parallel-connected stack of HTS coated-conductor tapes". In: *IEEE Transactions on Applied Superconductivity* 30.4 (2020).

[80] J. M. Brooks, M. D. Ainslie, R. A. Badcock, and C. W. Bumby. "Effect of Stack Geometry on the Dynamic Resistance Threshold Fields for Vertical Stacks of Coated Conductor Tapes". In: *IEEE Transactions on Applied Superconductivity* 31.5 (2021).

[81] M. D. Ainslie, C. W. Bumby, Z. Jiang, R. Toyomoto, and N. Amemiya. "Numerical modelling of dynamic resistance in high-temperature superconducting coated-conductor wires". In: *Superconductor Science and Technology* 31.7 (2018), p. 074003.

[82] Q. Li, M. Yao, Z. Jiang, C. W. Bumby, and N. Amemiya. "Numerical modeling of dynamic loss in HTS-coated conductors under perpendicular magnetic fields". In: *IEEE Transactions on Applied Superconductivity* 28.2 (2017).

[83] J. Geng and T. A. Coombs. "Modeling methodology for a HTS flux pump using a 2D H-formulation". In: *Superconductor Science and Technology* 31.12 (2018), p. 125015.

[84] H. Zhang, P. Machura, K. Kails, H. Chen, and M. Mueller. "Dynamic loss and magnetization loss of HTS coated conductors, stacks, and coils for high-speed synchronous machines". In: *Superconductor Science and Technology* 33.8 (2020), p. 084008.

[85] S. Otten and F. Grilli. "Simple and fast method for computing induced currents in superconductors using freely available solvers for ordinary differential equations". In: *IEEE Transactions on Applied Superconductivity* 29.8 (2019).

[86] R. Liu, W. Yang, D. Song, J. Zhu, and X. Li. "Effect of Dynamic resistance on AC loss in stacked superconducting tapes". In: *IEEE Transactions on Applied Superconductivity* 30.4 (2020).

[87] P Fabbricatore, S Farinon, S Innocenti, and F Gömöry. "Magnetic flux shielding in superconducting strip arrays". In: *Physical Review B* 61.9 (2000), p. 6413.

[88] J. Geng, J. M. Brooks, C. W. Bumby, and R. A. Badcock. "Time-varying magnetic field induced electric field across a current-transporting type-II superconducting loop: beyond dynamic resistance effect". In: *Superconductor Science and Technology, Under Review* (2021).

[89] S. Stavrev, F. Grilli, B. Dutoit, N. Nibbio, E. Vinot, I. Klutsch, G. Meunier, P. Tixador, Y. Yang, and E. Martinez. "Comparison of numerical methods for modeling of superconductors". In: *IEEE transactions on magnetics* 38.2 (2002).

[90] G Barnes, M McCulloch, and D Dew-Hughes. "Computer modelling of type II superconductors in applications". In: *Superconductor Science and Technology* 12.8 (1999), p. 518.

[91] A. Campbell. "A direct method for obtaining the critical state in two and three dimensions". In: *Superconductor Science and Technology* 22.3 (2009), p. 034005.

[92] T. Benkel, M. Lao, Y. Liu, E. Pardo, S. Wolfstädter, T. Reis, and F. Grilli. "T–A-formulation to model electrical machines with HTS coated conductor coils". In: *IEEE Transactions on Applied Superconductivity* 30.6 (2020).

[93] H. Zhang, M. Zhang, and W. Yuan. "An efficient 3D finite element method model based on the T–A formulation for superconducting coated conductors". In: *Superconductor Science and Technology* 30.2 (2016), p. 024005.

[94] B. Shen, F. Grilli, and T. Coombs. "Review of the AC loss computation for HTS using H-formulation". In: *Superconductor Science and Technology* 33.3 (2020), p. 033002.

[95] B. Shen, F. Grilli, and T. Coombs. "Overview of H-formulation: A versatile tool for modeling electromagnetics in high-temperature superconductor applications". In: *IEEE access* 8 (2020).

[96] E. Pardo, J. Šouc, and L. Frolek. "Electromagnetic modelling of superconductors with a smooth current–voltage relation: variational principle and coils from a few turns to large magnets". In: *Superconductor Science and Technology* 28.4 (2015), p. 044003.

[97] E. Pardo and M. Kapolka. "3D computation of non-linear eddy currents: Variational method and superconducting cubic bulk". In: *Journal of Computational Physics* 344 (2017), pp. 339–363.

[98] M. D. Ainslie. "Transport AC loss in high temperature superconducting coils". PhD thesis. University of Cambridge, 2012.

[99] C. Rey. *Superconductors in the power grid: Materials and applications*. Elsevier, 2015.

[100] N. M. Strickland, S. C. Wimbush, A. Pantoja, D. M. Pooke, M. Fee, V. Chamritskii, Z Hartwig, J. Cheng, S. Garberg, and B. Sorbom. "Extended-Performance "SuperCurrent" Cryogen-Free Transport Critical-Current Measurement System". In: *IEEE Transactions on Applied Superconductivity* 31.5 (2021).

[101] N Haned and M Missous. "Nano-tesla magnetic field magnetometry using an InGaAs–AlGaAs–GaAs 2DEG Hall sensor". In: *Sensors and Actuators A: Physical* 102.3 (2003), pp. 216–222.

[102] D. Dew-Hughes. "The critical current of superconductors: an historical review". In: *Low temperature physics* 27.9 (2001), pp. 713–722.

[103] A. Campbell and J. Evetts. "Flux vortices and transport currents in type II superconductors". In: *Advances in Physics* 21.90 (1972), pp. 199–428.

[104] D. A. Huse, M. P. Fisher, and D. S. Fisher. "Are superconductors really superconducting?" In: *Nature* 358.6387 (1992), pp. 553–559.

[105] M. Leroux, F. F. Balakirev, M. Miura, K. Agatsuma, L. Civale, and B. Maiorov. "Dynamics and critical currents in fast superconducting vortices at high pulsed magnetic fields". In: *Physical Review Applied* 11.5 (2019), p. 054005.

[106] E. Talantsev, N. Strickland, S. Wimbush, and W. Crump. "The onset of dissipation in high-temperature superconductors: Self-field experiments". In: *AIP Advances* 7.12 (2017), p. 125230.

[107] E. F. Talantsev, A. Pantoja, W. P. Crump, and J. L. Tallon. "Current distribution across type II superconducting films: a new vortex-free critical state". In: *Scientific reports* 8.1 (2018), pp. 1–9.

[108] E. Talantsev and J Brooks. "The onset of dissipation in high-temperature superconductors: flux trap, hysteresis and in-field performance of multifilamentary $\mathrm{Bi}_2 Sr_2 Ca_2 Cu_3 O_{10+x} wires$". In: *Materials Research Express* 6.2 (2018), p. 026002.

[109] J. Zuber, F. S. Wells, S. A. Fedoseev, T. H. Johansen, A. B. Rosenfeld, and A. V. Pan. "A new approach to the inverse problem for current mapping in thin-film superconductors". In: *Journal of Applied Physics* 123.12 (2018), p. 123906.

[110] J. Ade-Hall, R. Wilson, and P. Smith. "The petrology, Curie points and natural magnetizations of basic lavas". In: *Geophysical Journal International* 9.4 (1965), pp. 323–336.

[111] K. Fabian, V. P. Shcherbakov, and S. A. McEnroe. "Measuring the Curie temperature". In: *Geochemistry, Geophysics, Geosystems* 14.4 (2013), pp. 947–961.

[112] D.-X. Chen and C Gu. "Alternating current loss in a cylinder with power-law current-voltage characteristic". In: *Applied Physics Letters* 86.25 (2005), p. 252504.

[113] D.-X. Chen and C Gu. "A universal formulation for the transport V (I) curve of a superconducting cylinder with a power law E (J)". In: *Journal of Applied Physics* 101.12 (2007), p. 123921.

[114] H. Liu, G. Li, H. Zhang, and Y. Wang. "Numerical modeling and experimental analysis of AC critical current in YBCO-coated conductors". In: *IEEE Transactions on Applied Superconductivity* 25.3 (2014).

[115] S. Li and D.-X. Chen. "Scaling law for voltage–current curve of a superconductor tape with a power-law dependence of electric field on a magnetic-field-dependent sheet current density". In: *Physica C: Superconductivity and its Applications* 538 (2017), pp. 32–39.

[116] J. Geng, K Matsuda, L Fu, J.-F. Fagnard, H. Zhang, X Zhang, B. Shen, Q Dong, M Baghdadi, and T. Coombs. "Origin of DC voltage in type II superconducting flux pumps: field, field rate of change, and current density dependence of resistivity". In: *Journal of Physics D: Applied Physics* 49.11 (2016), 11LT01.

[117] Z. Jiang, C. W. Bumby, R. A. Badcock, H.-J. Sung, N. J. Long, and N. Amemiya. "Impact of flux gap upon dynamic resistance of a rotating HTS flux pump". In: *Superconductor Science and Technology* 28.11 (2015), p. 115008.

[118] C. Li, J. Geng, B. Shen, J. Ma, J. Gawith, and T. A. Coombs. "Investigation on the transformer-rectifier flux pump for high field magnets". In: *IEEE Transactions on Applied Superconductivity* 29.5 (2019).

[119] J Geng, K Matsuda, B Shen, H Zhang, X Zhang, L Fu, Z Huang, and T. Coombs. "HTS persistent current switch controlled by AC magnetic field". In: *IEEE Transactions on Applied Superconductivity* 26.3 (2016).

[120] X. Li, C. Li, X. Zhao, X. Du, X. Nie, Y. Xiong, J. Zhao, J. Sheng, Y. Wang, M. Zhang, et al. "Study on two different charging methods for superconducting coils in persistent current mode". In: *Physica C: Superconductivity and its Applications* 554 (2018), pp. 44–50.

[121] C. Li, J. Geng, B. Shen, X. Li, J. Gawith, J. Ma, J. Yang, and T. Coombs. "Persistent current switch for HTS superconducting magnets: Design, control strategy, and test results". In: *IEEE Transactions on Applied Superconductivity* 29.2 (2018).

[122] V. M. Zermeño, K. Habelok, M. Stępień, and F. Grilli. "A parameter-free method to extract the superconductor's J_c (B, θ) field-dependence from in-field current–voltage characteristics of high temperature superconductor tapes". In: *Superconductor Science and Technology* 30.3 (2017), p. 034001.

[123] D Hu, M. Ainslie, J. Rush, J. Durrell, J Zou, M. Raine, and D. Hampshire. "DC characterization and 3D modelling of a triangular, epoxy-impregnated high temperature superconducting coil". In: *Superconductor Science and Technology* 28.6 (2015), p. 065011.

[124] D. Hu, M. D. Ainslie, M. J. Raine, D. P. Hampshire, and J. Zou. "Modeling and comparison of in-field critical current density anisotropy in high-temperature superconducting (HTS) coated conductors". In: *IEEE Transactions on Applied Superconductivity* 26.3 (2016).

[125] B. Shen, J. Li, J. Geng, L. Fu, X. Zhang, C. Li, H. Zhang, Q. Dong, J. Ma, and T. Coombs. "Investigation and comparison of AC losses on stabilizer-free and copper stabilizer HTS tapes". In: *Physica C: Superconductivity and its applications* 541 (2017), pp. 40–44.

[126] G. Liu, G. Zhang, H. Yu, L. Jing, L. Ai, and Q. Liu. "Experimental and numerical study of frequency-dependent transport loss in $YBa_2Cu_3O_{7-\delta}$ coated conductors with ferromagnetic substrate and copper stabilizer". In: *Journal of Applied Physics* 121.24 (2017), p. 243902.

[127] J. R. Clem. "Theory of flux-flow noise voltage in superconductors". In: *Physical Review B* 1.5 (1970), p. 2140.

[128] J. D. Jackson. *Classical electrodynamics.* 1999.

[129] Z. Jiang, W. Zhou, Q. Li, M. Yao, J. Fang, N. Amemiya, and C. W. Bumby. "The dynamic resistance of YBCO coated conductor wire: effect of DC current magnitude and applied field orientation". In: *Superconductor Science and Technology* 31.3 (2018), p. 035002.

[130] T Matsushita. "Flux pinning and electromagnetic phenomenon". In: *Tokyo* 345 (1994), p. 99.

[131] D. Van der Laan, J. Weiss, and D. McRae. "Status of CORC® cables and wires for use in high-field magnets and power systems a decade after their introduction". In: *Superconductor Science and Technology* 32.3 (2019), p. 033001.

[132] D. Van Der Laan, J. Weiss, U. Trociewitz, D Abraimov, A Francis, J Gillman, D. Davis, Y Kim, V Griffin, G Miller, et al. "A CORC® cable insert solenoid: the first high-temperature superconducting insert magnet tested at currents exceeding 4 kA in 14 T background magnetic field". In: *Superconductor Science and Technology* 33.5 (2020), 05LT03.

[133] Y. Wang, M. Zhang, F. Grilli, Z. Zhu, and W. Yuan. "Study of the magnetization loss of CORC® cables using a 3D TA formulation". In: *Superconductor Science and Technology* 32.2 (2019), p. 025003.

[134] L Muzzi, G De Marzi, A Di Zenobio, and A Della Corte. "Cable-in-conduit conductors: lessons from the recent past for future developments with low and high temperature superconductors". In: *Superconductor Science and Technology* 28.5 (2015), p. 053001.

[135] M. Staines, N. Glasson, M. Pannu, K. P. Thakur, R. Badcock, N. Allpress, P. D'Souza, and E. Talantsev. "The development of a Roebel cable based 1 MVA HTS transformer". In: *Superconductor Science and Technology* 25.1 (2011), p. 014002.

[136] Z Hong and T. Coombs. "Numerical modelling of AC loss in coated conductors by finite element software using H formulation". In: *Journal of Superconductivity and Novel Magnetism* 23.8 (2010), pp. 1551–1562.

[137] J. Ekin. *Experimental techniques for low-temperature measurements: cryostat design, material properties and superconductor critical-current testing.* Oxford university press, 2006.

[138] Z. Jiang, K. Thakur, M. Staines, R. Badcock, N. Long, R. Buckley, N. Amemiya, and A. Caplin. “Transport AC loss characteristics of a five strand YBCO Roebel cable with magnetic substrate”. In: *IEEE Transactions on Applied Superconductivity* 21.3 (2010).

[139] Z. Jiang, R. Badcock, N. Long, M. Staines, K. Thakur, L. Lakshmi, A Wright, K Hamilton, G. Sidorov, R. Buckley, et al. “Transport AC loss characteristics of a nine strand YBCO Roebel cable”. In: *Superconductor Science and Technology* 23.2 (2010), p. 025028.

[140] J. M. Brooks, M. D. Ainslie, R. Mataira, R. A. Badcock, and C. W. Bumby. “Below 1 μV cm-1: Determining the geometrically-saturated critical transport current of a superconducting tape”. In: *Superconductor Science and Technology* 34.8 (2021).

[141] L. Quéval, V. M. Zermeño, and F. Grilli. “Numerical models for ac loss calculation in large-scale applications of HTS coated conductors”. In: *Superconductor Science and Technology* 29.2 (2016), p. 024007.